Graphene, a two-dimensional material consisting of carbon atoms arranged in a honeycomb lattice, has become famous for the evidence that its electronic structure approximately corresponds to the one of massless Dirac fermions.
However, in order to correctly describe graphene, the spin, which plays an essential role in the physics of Dirac fermions, has to be replaced by the so-called pseudospin, an intrinsic property of the honeycomb lattice which is not related to the electrons' real spin. If the real spin is considered, too, the effective Hamiltonian has to be extended by terms which have no equivalents in the original Dirac Hamiltonian.
While charge transport properties can be predicted from Dirac physics very reliably, the extended Hamiltonian leads to new phenomena in the context of spin transport. In this thesis two distinct topics are investigated theoretically. The presented results are mainly based on numerical simulations using a recursive Green's function algorithm. The first part of this thesis covers spin relaxation in graphene. Different sources of spin relaxation are investigated with a particular focus on the role of locally varying spin-orbit coupling and adatoms. The second part covers edge magnetism in graphene zigzag nanoribbons. It is shown how magnetic clusters form even in the presence of a potential which is not homogeneous in space. Different signatures of zigzag edge magnetization in charge and spin transport are presented.

Universitätsverlag Regensburg

ISBN 978-3-86845-115-3
gefördert von:
Alumni der physikalischen Fakultät der Universität Regensburg e.V.

Universität Regensburg

Dissertationsreihe Physik - Band 42

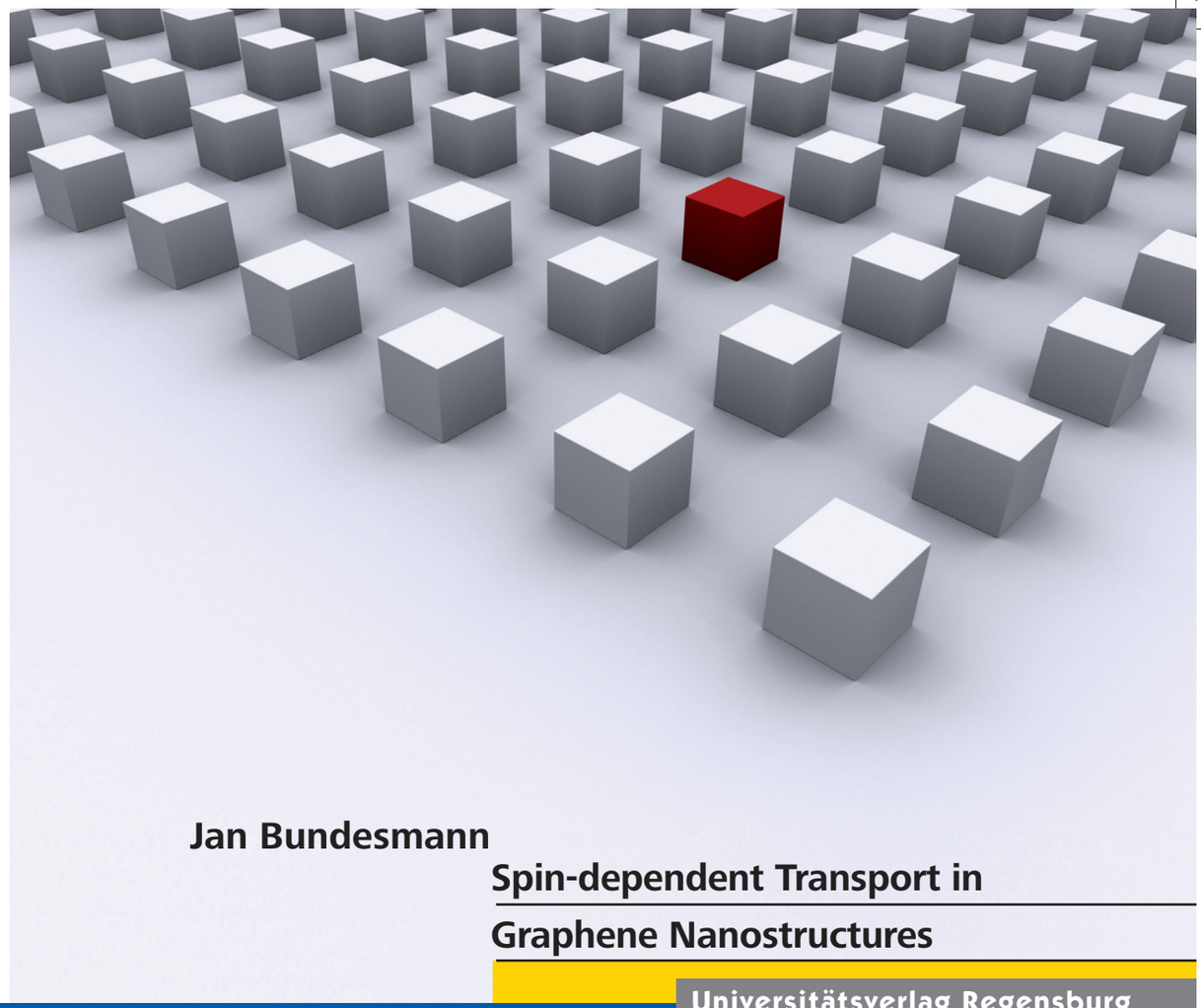

Jan Bundesmann

Spin-dependent Transport in Graphene Nanostructures

Universitätsverlag Regensburg

42

Dissertationsreihe Physik

Jan Bundesmann

Jan Bundesmann

Spin-dependent Transport in Graphene Nanostructures

Spin-dependent Transport in Graphene Nanostructures

Dissertation zur Erlangung des Doktorgrades der Naturwissenschaften (Dr. rer. nat.)
der naturwissenschaftlichen Fakultät II - Physik der Universität Regensburg
vorgelegt von

Jan Bundesmann

aus Gräfelfing
im Jahr 2014

Die Arbeit wurde von Prof. Dr. Klaus Richter angeleitet.
Das Promotionsgesuch wurde am 01.10.2009 eingereicht.

Prüfungsausschuss:	Vorsitzender:	Prof. Christoph Strunk
	1. Gutachter:	Prof. Klaus Richter
	2. Gutachter:	Prof. Milena Grifoni
	weiterer Prüfer:	Prof. Tilo Wettig

Dissertationsreihe der Fakultät für Physik der Universität Regensburg, Band 42

Herausgegeben vom Präsidium des Alumnivereins der Physikalischen Fakultät:
Klaus Richter, Andreas Schäfer, Werner Wegscheider, Dieter Weiss

Jan Bundesmann

Spin-dependent Transport in Graphene Nanostructures

Universitätsverlag Regensburg

Bibliografische Informationen der Deutschen Bibliothek.
Die Deutsche Bibliothek verzeichnet diese Publikation
in der Deutschen Nationalbibliografie. Detailierte bibliografische Daten
sind im Internet über http://dnb.ddb.de abrufbar.

1. Auflage 2014
© 2014 Universitätsverlag, Regensburg
Leibnizstraße 13, 93055 Regensburg

Konzeption: Thomas Geiger
Umschlagentwurf: Franz Stadler, Designcooperative Nittenau eG
Layout: Jan Bundesmann
Druck: Docupoint, Magdeburg
ISBN: 978-3-86845-115-3

Alle Rechte vorbehalten. Ohne ausdrückliche Genehmigung des Verlags ist es nicht gestattet, dieses Buch oder Teile daraus auf fototechnischem oder elektronischem Weg zu vervielfältigen.

Weitere Informationen zum Verlagsprogramm erhalten Sie unter:
www.univerlag-regensburg.de

Contents

1. Introduction **1**
- 1.1. Spintronics . . . 1
- 1.2. Graphene . . . 3
- 1.3. Outline . . . 4

2. Mesoscopic transport **7**
- 2.1. Defining mesoscopic physics . . . 7
- 2.2. Green's functions . . . 8
- 2.3. Transport through open systems . . . 9
  - 2.3.1. Selfenergies . . . 9
  - 2.3.2. The recursive Green's function method . . . 11
  - 2.3.3. Optimized recursive Green's function method for transmission at different system lengths . . . 12

3. Graphene **15**
- 3.1. Graphene basics . . . 15
- 3.2. Tight-binding description . . . 16
  - 3.2.1. Electrons without spin . . . 16
  - 3.2.2. Electrons with spin . . . 19
- 3.3. Klein tunneling in the presence of spin-orbit coupling . . . 22
- 3.4. Summary . . . 25

I. Spin Relaxation in Graphene **27**

4. Introduction **29**

5. DP and EY in graphene **31**
- 5.1. The Dyakonov-Perel mechanism in graphene . . . 31
- 5.2. Elliot-Yafet mechanism in graphene . . . 36
- 5.3. Summary . . . 40

6. Sherman mechanism in graphene **43**
- 6.1. Sherman spin relaxation mechanism . . . 44
- 6.2. Impurity-Induced Spin-Orbit Coupling in Graphene . . . 45
- 6.3. Numerical Results . . . 46
- 6.4. Discussion and Summary . . . 50

7. Atomistic description of adsorbed adatoms **53**
7.1. Tight-binding model for adsorbates 53
7.2. DOS of fluorinated and hydrogenated graphene 56
7.3. Adatoms and charge transport 58
7.4. Spin relaxation in random spin-orbit fields 60
7.4.1. Spin-dependent scattering from a single adatom 60
7.4.2. Spin-dependent scattering from a cluster of adatoms 60
7.4.3. Adatoms in diffusive graphene 62
7.5. Magnetic moment formation 63
7.5.1. Single adatom limit 63
7.5.2. Resonant magnetic scatterers in diffusive graphene 64
7.6. Summary 69

II. Edge Magnetism in Graphene **71**

8. Introduction **73**

9. Magnetic Alignment with Disorder **75**
9.1. Hubbard model and Hartree-Fock approximation 75
9.2. Searching for the magnetic edge state 76
9.3. On the route to a phenomenological model 78
9.4. Using the results for transport calculations 82

10. Transport calculations **87**
10.1. Formalism 87
10.2. Localized mesoscopic transport 88
10.2.1. Decomposition 90
10.2.2. Average values 91
10.3. Controllable finite spin conductance 92
10.4. Summary 93

11. Conclusions and perspectives **95**
11.1. Spin relaxation in graphene 95
11.2. Zigzag edge magnetism 97
11.3. Perspectives 97

III. Appendix **99**

A. Recursive Green's function formalism **101**

B. Interactions **103**
B.1. Interacting Hamiltonian in second quantization for uncorrelated electrons 103
B.2. Interacting Hamiltonian on a Discrete lattice 104
B.3. Hubbard model in Hartree-Fock approximation 105

B.4. Calculation scheme 108

C. Sherman spin relaxation **109**
C.1. Correlation function of Rashba disorder 109
C.2. Sherman spin relaxation rate 112

Bibliography **113**

Publication list **125**

Danksagung **127**

1. Introduction

1.1. Spintronics

In this thesis, we will treat topics which can be attributed to the field of spintronics: the study of charge and spin distributions and their corresponding currents in mesoscopic systems: an important tool to obtain an understanding of quantum phenomena and useful for information storage and processing.

The beginning of spintronics is dated to the discovery of the giant magnetoresistive effect (GMR) in 1988 [1, 2]. It consists of the dependence of the resistivity of a multilayer semiconductor systems on the electron's spin. Soon, it came widely used for data read-out in computer hard discs which brought spintronics to our living rooms [3].

From a technical perspective, there exist great expectations for spintronic devices. They are expected to show a large number of advantages: "nonvolatility, increased data processing speed, decreased electric power consumption, and increased integration densities compared with conventional semiconductor devices" [4]. So far, the GMR and the closely related tunneling magnetoresistive effect [5, 6, 7] are the only available spintronics applications in our daily lifes.

In particular, spin based information processing in logical circuits still seems a long way off. Three obstacles have to be overcome for this goal. First, spins have to be injected and detected at a high reliability. Second, the spin orientation shall be controllable. Third, optimal materials for those purposes have to be found. For technological usability the solution to these three points has to be found for room temperature and only partial success has been achieved until now.

The three obstacles are following a hierarchy as a successful spin injection and detection must be achieved first in order to tackle the other problems. Nowadays, optical methods of spin injection and detection are known and used in experiments [8, 9, 10, 11] but the demand of uniform and integrated spintronics devices requires all-electronic injection and detection of spins. This is already available for metals since the mid 1980's thanks to proposals from Johnson and Silsbee [12, 13]. Materials considered nowadays, e. g. semiconductors, often have a lower conductivity as the injection electrode. This *conductivity mismatch* is a serious problem since, instead of diffusing into the transport channels, injected electrons get directly reflected back into the ferromagnetic contact.

This issue was not solved before, in 2001, Fert and Jaffres suggested to separate the magnetic injection electrode from the semiconductor by a thin tunnel barrier [14]. Successful spin injection was demonstrated shortly afterwards in Groningen opening the route for systems that permit "the study of spin transport phenomena, such as controlled spin precession in solid state devices and the control of spin-polarized currents at room temperature by additional ferromagnetic contacts" [15].

Apparently, the first hurdle has been taken and this, consequently, allows for an all-electric study of methods to control spin injection. We list interesting proposals and realizations of this second issue.

In very clean semiconductor heterostructures the Rashba effect [16] can be used to rotate spins by an amount proportional to an externally applied electric field. This is the basis for *Datta-Das* spin field-effect transistor (FET) [17]. Using spin rotation from an externally applied electric field to switch conductance in "Control of Spin Precession in a Spin-Injected Field Effect Transistor" has been demonstrated in high-mobility InAs structures [18]. However, the demands for clean structures are very strict.

Similarly, spins can be rotated by an external magnetic field. This so-called spin Hanle effect was first proposed by Johnson and Silsbee [12, 13] and, for the first time, successfully utilized in Groningen after their successful injection and detection of spins in metallic spin valves [19].

A shortcoming of the Datta-Das spin FET is encountered in non-ballistic systems where the randomization of the electron's momentum leads to a randomization of the spin precession axis. To avoid this problem, Schliemann et al. suggested to choose a system with not only Rashba spin-orbit coupling (SOC) but also Dresselhaus SOC present [20]. When the corresponding interaction strengths, α and β differ, spins get randomized, the transistor is in the "off state". Switching to the "on state" is performed by applying an external electric field in a way that $\alpha = \beta$. Notably, the "on state" is characterized by a persistent spin helix, a particular spin rotation pattern where the orientation only depends on the position of the electron along the transport direction not on the exact path [21, 22].

Further selected examples are "Spin-Transistor Action via Tunable Landau-Zener Transitions" [23] and "Spin Transistor Action from Hidden Onsager Reciprocity" [24]. Betthausen at al. [23] showed that they could switch between "on" and "off" states by applying a magnetic field to a diluted magnetic semiconductor quantum well covered by an array of ferromagnetic stripes. In the presence of the magnetic field, spin evolution is no longer adiabatic and, hence, allows for spin flip scattering which translates into an increased resistance, the "off state".

Adagideli et al. [24] could show that a position dependent SOC can be described as an effective magnetic field in a spin-less description by applying an appropriate $SU(2)$ gauge transformation. Then, due to Onsager relations [25, 26], spin conductance vanishes, the transistor is in the "off state". Switching to the "on state" is done by either breaking time reversal symmetry by applying a true magnetic field or by adding a third lead. These three proposals have their robustness against disorder as a common advantage in comparison to the *original* spin FET proposal by Datta and Das [17]. They are, however, only a small selection of the available proposals.

The third issue, judging on a material's suitability as a spintronic base material, can be addressed with the presented methods. In particular, Hanle measurements can help deciding on that question as the detected spin signal is directly influenced by the spin relaxation time τ_S, which is a quantity to estimate how fast spin information gets lost. For technical applications a large τ_S is desired. Fundamental research addresses the question what is causing spin relaxation in a given material and how fast this happens. With respect to investigations on controlling spin orientations, also, long

spin relaxation times are desired to discriminate intrinsically and extrinsically induced spin-flip. This is where graphene enters stage as a possible candidate.

1.2. Graphene

Graphene is a carbon allotrope formed by atoms which are arranged in a honeycomb lattice. The first description of its electronic properties dates back to 1947 [27]. In 1984, Semenoff suggested that graphene mimics the physics of two-dimensional massless Dirac fermions with a reduced speed of light [28]. This resemblance discriminates graphene from other two-dimensional electron system. It could, however, not be verified before graphene became available for experiments in 2004 [29]. Most prominent features of the Dirac nature of electrons in graphene, which have been observed experimentally, are the half-integer quantum hall effect [29, 30] and Klein tunneling [31]. The latter one is the result of the strong coupling between spin and orbital degree of freedom. In the effective Dirac Hamiltonian for graphene the real spin is replaced by the so-called pseudospin, a property of electrons in graphene defined by its lattice structure. The formal equivalence between electrons in graphene and massless Dirac fermions is, however, destroyed when we also consider the real spin of the electrons in graphene. An effective description of electrons in graphene contains orbital, pseudospin and real spin degrees of freedom. Their interplay will be the main purpose of this work.

Intrinsically, the electrons' spins are only weakly coupled to other degrees of freedom in graphene due to the absence of a nuclear spin in the majority of the carbon cores.[1] This makes graphene a very promising candidate for spintronics applications and, moreover, keeps the formerly mentioned resemblance to Dirac fermions intact. We will consider two examples in this thesis of the occurrence of strong spin-orbit coupling and other spin-dependent terms in the electronic Hamiltonian of graphene, namely the presence of adsorbed adatoms, and the so-called zigzag edge magnetism.

The presence of adatoms is hardly avoidable in the state-of-the-art manufacturing processes of graphene. Since graphene consists basically only of surface, there is no bulk, far away from the influence of surface effects, which could lead to undisturbed electron transport. This makes graphene much more sensitive to surface disturbances than extended materials. We will show that already a small concentration of hydrogen adatoms turns graphene into a material not suited for spintronics because spins get relaxed quickly by strong, randomized magnetic moments around resonant scatterers [33]. Similar effects can be expected for other adatoms or defects in the graphene lattice [34]. On the other hand, without adatoms and defects, there is no reason to disapprove graphene for spin transport.

Along the edges of graphene nanostructures, under certain circumstances, magnetic moments can form, too, which we summarize under the term zigzag edge magnetism [35]. They are the result of electron-electron interactions considered in mean-field approximation. No experimental evidence for that exists so far, also because the

[1] Carbon materials from natural sources consist of mainly two carbon isotopes. More than 99% is made up from ^{12}C, which does not have a nuclear spin. The remaining $< 1\%$ is ^{13}C with a finite nuclear spin [32].

effect is believed to be destroyed by disorder. We will investigate transport in the disordered graphene nanostructures and show that, indeed, edge magnetism exists in disordered graphene nanostructures and it induces spin conductance obeying universal predictions. Moreover, we propose a new method to use zigzag edge magnetism for creating a finite spin conductance.

1.3. Outline

This thesis is structured in three parts.

We begin with an introductory part consisting of chapters 2 and 3. In chapter 2 we present the general framework of mesoscopic two-dimensional physics and sketch the computational methods used within this thesis.

Chapter 3 is an overview over the physics of electrons in graphene. Therein, we present the widely used single-band single-electron tight-binding Hamiltonian. We do not restrict ourselves to the spin-less Hamiltonian but introduce the spin-dependent terms arising in the description of graphene. The chapter ends with a short illustrative example of both the transport formalism and the graphene physics, the spin-dependent Klein tunneling [36].

The second part treats spin relaxation in graphene. It aims at the revelation of the dominant spin relaxation mechanism. To this end we dedicate chapter 5 to the presentation of the Dyakonov-Perel and the Elliot-Yafet mechanism. These important mechanisms are usually held responsible for spin relaxation in mesoscopic quantum transport. After introducing their modes of action we present numerical calculations and compare them to analytic predictions.

The focus of chapter 6 is spin relaxation due to spin-orbit coupling strength fluctuating in space. The underlying mechanism is conventionally called Sherman mechanism [37] and it is considered a good candidate to explain the high spin relaxation rate in graphene [38, 39]. This model is combined with the short-range spin-orbit disorder originally proposed by Castro-Neto and Guinea [40] to derive an expected spin relaxation length. Again, we compare the analytical predictions to numerical calculations and, furthermore, use them to investigate parameter ranges not accessible analytically.

The model of fluctuating spin-orbit coupling used in chapter 6 is contrasted with an atomistic description of graphene in the presence of adatoms within an extended tight-binding model in chapter 7. In this chapter we extend the tight-binding model for electrons in graphene presented in chapter 3. Again, these adatoms lead to a spin-orbit coupling field [41, 42, 43, 33] which is investigated with respect to its influence on spin relaxation. Due to the extension of the tight-binding model resonant scattering is now included, too. Additionally and in contrast to the chapters 5 and 6, the extended tight-binding model contains local spin-splitting due to magnetization [33]. We show that this is by far more efficient in relaxing spins than spin-orbit coupling and much lower adatom concentrations are needed to obtain spin relaxation rates comparable to the experimental findings than in the pure spin-orbit coupling case.

The third part contains a closer look at magnetism in graphene. We investigate the intrinsic magnetization of the zigzag edge which is predicted from various calculations that take into account electron-electron interactions.

To this end we present the theoretical basis of the zigzag edge magnetism and perform calculation within a mean-field Hubbard Hamiltonian in chapter 9. In contrast to the existing literature we include changes of the local potential and perform a thorough investigation of the spin density in that case which allows to define an effective spin-dependent potential landscape. As the full self-consistent mean-field calculation is computationally demanding we use the insights of our investigations to justify a phenomenological model which assumes the formation of clusters of magnetic moments close to where charge neutrality lines coincide with zigzag edges.

The phenomenological model is used for transport calculations which are presented in chapter 10. We focus on transport in the localized regime close to the Fermi level since this is where we expect (see chapter 9) the magnetic edge to alter transport efficiently. To compensate for the shortcomings of the phenomenological model we study universal transport properties and the potential to create a spin-polarized currents with respect to relative orientations of the magnetic clusters. Those might be completely uncorrelated or collinear along the edges.

Finally we summarize and conclude in chapter 11.

2. Mesoscopic transport

The physical systems treated in this work are based on graphene which is a very good candidate for studies in the field of two-dimensional mesoscopic physics. While the field of mesoscopic and low-dimensional physics arose in the 1980s by the emerging possibility to fabricate small conductors, graphene did not become available until 2004 [29]. Its popularity quickly increased turning it to a widely used system for the understanding of mesoscopic phenomena.

To set the framework we are working in, it is necessary to give a brief review about mesoscopic physics and transport in mesoscopic systems before turning our attention to graphene. This chapter is intentionally kept short by mainly referring to textbooks and review articles that treat the topics more thoroughly.

2.1. Defining mesoscopic physics

Mesoscopic physics is characterized by the size of the considered system lying between the microscopic and the macroscopic regime. This very vague description should be quantified by introducing the system size L, the phase coherence length L_ϕ and the wavelength of the considered particles, e. g. the electron's de-Broglie wavelength $\lambda_F = 2\pi/k$. To call a system mesoscopic we require

$$\lambda_F \ll L \lessapprox L_\phi. \tag{2.1}$$

The first part of this inequality discriminates mesoscopic physics from microscopic physics, i. e. from the description of the dynamics on atomic lengthscales. The second inequality makes sure that the particles still behave as quantum mechanic entities by not loosing their phase information to the environment too fast. Furthermore it is important to distinguish mesoscopic physics from macroscopic and classical physics. In terms of transport physics the latter relation discriminates mesoscopic conductors from ohmic conductors.

It is important to find a way to describe mesoscopic systems efficiently, since a full quantum mechanical treatment is not feasible, while still sustaining their quantum nature visible in certain signatures. Examples of these signatures are weak localization [44, 45] or universal conductance fluctuations [46] in mesoscopic transport, which cannot be explained purely classically.

An effective and efficient description of the system is achieved by reducing the complexity of the system according to some physical assumptions. Often, as well as in this work, interactions between different particles are ignored or reduced to a simpler model, so that an effective Hamiltonian is set up describing only the particles of interest. For this thesis the tight-binding Hamiltonian of electrons in graphene, which is introduced in section 3.2, assumes this role.

Graphene is also a good example to roughly sketch the physical approximations. The Hamiltonian used is a single-band single-electron tight-binding Hamiltonian. We neglect the dynamics of the carbon cores within the Born-Oppenheimer approximation, and the electrons in atomic states different from the considered p_z orbitals. The latter ones are only included indirectly in terms of spin-orbit interaction as will be used in part I of this thesis. Their influence is included perturbatively by means of a Lövdin transformation [47]. With the neglect of the cores' dynamics also the coupling between electrons and phonons is ignored. Furthermore we discard electron-electron interactions or rather include them only on a mean field level in part II.

The tight-binding model acts on states localized around the carbon atoms and, hence, naturally leads to a discretized Hamiltonian with a fixed spacing between neighboring sites. This encourages a numerical treatment in which the Hamiltonian is represented by a complex matrix. Apparently, graphene is described as a real two-dimensional material in contrast to two-dimensional electron or hole systems in semiconductor heterostructures.

2.2. Green's functions

While the Hamiltonian is a full description of a physical problem and allows for determining eigenvalues and eigenstates of a given system it is often convenient to choose an equivalent description when only observables or effective properties are desired.

Aiming for the calculation of transport properties we are interested in the amplitude or the probability for an electron's propagation from point A to point B. This amplitude is given by the system's propagator $\tilde{K}(t)$ in the time domain or by its Green's function $G(E)$ in energy space. The problems and the corresponding Hamiltonians within this work carry no explicit time dependence, so the Green's function is a suitable choice. $G(\alpha', \alpha; E) = \langle \alpha' | G(E) | \alpha \rangle$ is the amplitude for a particle to propagate from state α to state α' at a given energy E. The Green's function is related to the Hamiltonian $\mathcal{H}$ by

$$G^{R/A}(E) = (E - \mathcal{H} \pm \mathrm{i}\eta)^{-1}, \tag{2.2}$$

where the infinitesimally small imaginary quantity $\mathrm{i}\eta$ has been added to secure invertibility even if E is an eigenvalue of $\mathcal{H}$. Specifically we have to distinguish between the retarded and the advanced Green's function $G^{R/A}(E)$, labeled by the superscripts R and A.

Roughly spoken they can be identified with solutions of the Hamiltonian $\mathcal{H}$ approaching a given state α in time or moving away from it depending on the given boundary conditions. By introducing the small imaginary number $\mathrm{i}\eta$ the boundary conditions are fixed by shifting the poles of the $G(E)$ in the complex energy plane which is important for a numerical calculation of the Green's function.

The Green's function carries equivalent information as the Hamiltonian. Equation (2.2) is one possible definition of a physical Green's function which immediately can be identified with the mathematical definition of a Green's function of a differential

operator. There exist other equivalent definitions which depending on the situation might be more appropriate. We want to introduce also the spectral representation

$$G^{R/A}(x,x';E) = \sum_n \frac{\varphi_n(\boldsymbol{x})\varphi_n^*(\boldsymbol{x'})}{E - E_n \pm \mathrm{i}\eta}, \tag{2.3}$$

making use of the wavefunctions $\varphi_n(\boldsymbol{x})$ of the Hamiltonian's eigenstates $|n\rangle$. We already projected the Green's function into position space. In this representation it is easily seen that the retarded Green's function allows for a direct access to the local density of states.

$$\frac{1}{\pi}\operatorname{Im} G^R(x,x;E) = \frac{1}{2\pi\mathrm{i}}(G^R - G^{R*}) = \sum_n \varphi_n^*(\boldsymbol{x})\varphi_n(\boldsymbol{x})\frac{1}{\pi}\frac{\eta}{(E-E_n)^2 - \eta^2}. \tag{2.4}$$

In the limit $\eta \to 0$, the last term is the Lorentz representation of the Dirac delta $\delta(E - E_n)$. So we end up with

$$\frac{1}{\pi}\operatorname{Im} G^R(x,y;E) = \sum_n \varphi_n^*(\boldsymbol{x})\varphi_n(\boldsymbol{x})\delta(E-E_n) = d(\boldsymbol{x},E). \tag{2.5}$$

In the next section we want to show how mesoscopic transport can be modeled using the Green's function.

2.3. Transport through open systems

2.3.1. Selfenergies

In a typical transport problem one is dealing with a scattering region and particle reservoirs far away from the scattering region connected to the scattering region via ideal, i. e. reflectionsless, leads as indicated in Fig. 2.1.

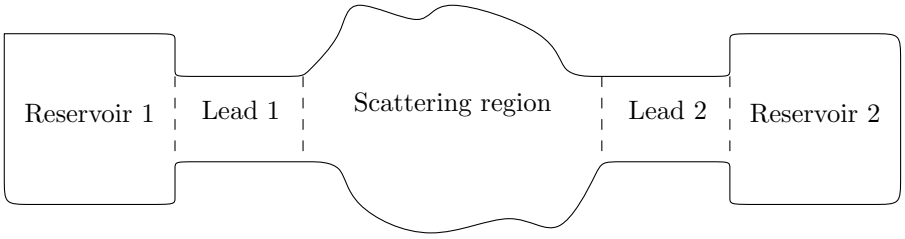

Figure 2.1.: Sketch of a typical scattering problem. By introducing the concept of self-energies we can cut the system at the broken lines where leads and scattering region touch; see text.

We only shortly revisit the basics of the scattering formalism used for this thesis. For a detailed description we refer the reader to existing literature and textbooks, e. g. Refs. [48, 49, 50]. In a first step the reservoirs are removed from the system which is possible as we are considering ideal ballistic leads. The reservoirs' influence is reflected by semi-infinite leads in which the available states are fully occupied up to

the reservoirs chemical potential or, in the case of equilibrium calculations, up to the Fermi level.

Still, while this decreases the systems complexity, an obstacle for a numerically supported calculation of the transport properties exists: besides the finite scattering region, our system consists of the infinite leads. The discretized Hamiltonian is infinitely large and, hence, not integrable numerically.

The problem can be further minimized at this point by reducing the full Hamiltonian to the one only describing the scattering region, $\mathcal{H}_S$, and adding self-energies Σ representing the leads' action. Let us formally write the Green's function as an infinitely large matrix in position space,

$$G = \begin{pmatrix} G_S & g_{SL} \\ g_{LS} & G_L \end{pmatrix} = \begin{pmatrix} E - \mathcal{H}_S & h \\ h^\dagger & E - \mathcal{H}_L \end{pmatrix}^{-1}. \tag{2.6}$$

We use indices L and S whenever leads or the scattering region are concerned, respectively. g_{SL} and g_{LS} are blocks of the Green's function and h and $h^\dagger$ are the blocks in the Hamiltonian connecting leads and scattering region. From equation (2.6) we obtain

$$(E - \mathcal{H}_S)G_S + hg_{LS} = I, \tag{2.7}$$

$$h^\dagger G_S + (E - \mathcal{H}_L)g_{LS} = 0. \tag{2.8}$$

This can be solved for scattering region's Green's function

$$G_S = \left[E - \mathcal{H}_S - h(E - \mathcal{H}_L)^{-1}h^\dagger\right]^{-1}. \tag{2.9}$$

$(E-\mathcal{H}_L)^{-1}$ is the Green's function of the isolated lead, the hopping matrices h and $h^\dagger$ have non-zero entries only in the contact region. The calculation of the isolated lead's Green's function is, hence, limited to the calculation of its surface Green's function.

At this point the lead's selfenergy,

$$\Sigma = h(E - \mathcal{H}_L)^{-1}h^\dagger, \tag{2.10}$$

shall be introduced. The concept of self-energies is very common in mesoscopic physics and can be used for instance as an approximative description of electron-electron or electron-phonon interactions. Due to the formal analogy Σ is also referred to as self-energy although it is an exact description of the leads. It allows to calculate the Green's function of a finite scattering region by a simple inversion of a finite matrix:

$$G^{R/A} = \left[E - (\mathcal{H}_S + \Sigma) \pm \mathrm{i}\eta\right]^{-1}. \tag{2.11}$$

To illuminate the effect of the selfenergy Σ, note that it is in general complex valued. The new Hamiltonian $\mathcal{H}_S + \Sigma$ is not hermitian anymore and the eigenvalues of the original Hamiltonian $\mathcal{H}_S$ get shifted and assume a certain broadening due to their imaginary part. The level broadening induced by the leads can also be understood as a reduction of the time a particle stays in the scattering region.

For the calculation of the selfenergy several methods exist. There is the widely used iterative method [51]. In molecular physics the so called wide-band limit is often

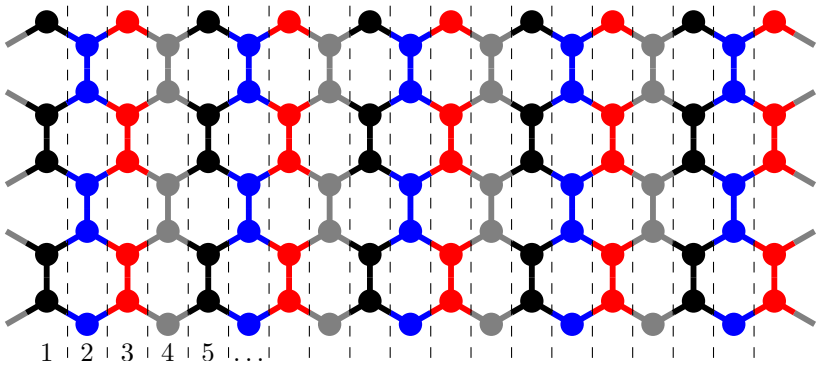

Figure 2.2.: Partitioning of a very simple graphene grid. Leads are attached at the left and right edges. Slices are indicated by a variation of line colors.

used, replacing Σ by a constant imaginary number. Wimmer developed an eigendecomposition based method, which is able to calculate the selfenergy of an arbitrary lead, independent of the underlying Hamiltonian [52]. We use the eigendecomposition based method for this work.

2.3.2. The recursive Green's function method

We could already calculate the Green's function from equation (2.11). The direct inversion of a matrix representing a grid of up to several millions of gridpoints would be, however, rather time demanding. Therefore, we want to shortly present the recursive Green's function (RGF) method which has been developed in the 1980s by Thouless and Kirkpatrick [53], Fisher and Lee [54], and MacKinnon [55] and been implemented for arbitrary grids using methods from graph theory by Wimmer [52, 56]. The numerical calculations performed in this thesis were performed with this last implementation, thus we refer to Ref. [52] for further details.

For the RGF method a system is partitioned into slices. These slices are fractions of the scattering systems of roughly equal size as shown in Fig. 2.2. Neighboring slices i and j are connected to each other via a hopping matrix $\mathcal{H}_{i,j}$. The RGF makes iterative use of the Dyson equation

$$G = G_0 + G_0 V G, \tag{2.12}$$

treating the hopping matrices as perturbations and the isolated slices as the unperturbed systems. The iteration starts from the contact region at one lead (with slice index N) subsequently adding slices until the other lead is reached at slice index 0. The connection between the retarded Green's function elements in two subsequent steps is

$$G^{r,i-1}_{i-1,i-1} = \left(E - \mathcal{H}_{i-1,i-1} - \mathcal{H}_{i-1,i} G^{r,i}_{i,i} \mathcal{H}_{i,i-1}\right)^{-1}, \tag{2.13}$$

$$G^{r,i-1}_{N,i-1} = G^{r,i}_{N,i} \mathcal{H}_{i,i-1} G^{r,i-1}_{i-1,i-1}. \tag{2.14}$$

Here superscript indices label the iteration number, subscripts indicate the slices matrix blocks are calculated for. $\mathcal{H}_{i,i}$ is the Hamiltonian of the isolated slice i. The

iteration starts with the surface Green's function of the lead as $G^{r,N}_{N,N}$. The RGF algorithm then fills the blocks in the matrix representation of the Green's function that are needed for the calculation of transmission and reflection, i. e. the diagonal blocks and the last row of blocks. After the complete iteration we end up with $G^r_{0,0}$ and $G^r_{N,0}$. Possibly, also other diagonal blocks $G^r_{i,i}$ can be stored to calculate the local density of states with equation (2.5). Notably not the full Green's function is calculated by this method but only the parts that are needed for transport.

Let us assume a system which can be sliced N times to slices of size M. The total number of grid points can be estimated as $M \cdot N$. The inversion of a matrix scales cubic with its number of rows or columns, so the direct inversion would scale cubic in both M and N. Using the RGF, each step in the iteration involves the inversion of a $M \times M$ matrix, scaling as M^3. This step has to be repeated N times, so the RGF scales with M^3N. Depending on the system geometry and size, the calculation can be significantly sped up. In particular, the calculation of transport in long and narrow systems benefits from this algorithm.

Finally the transmission amplitudes can be calculated from the Green's function using the Fisher-Lee relations [57],

$$t_{mn} = -\delta_{mn} + \mathrm{i}\hbar\sqrt{v_m v_n}\int_0^{L_1} \mathrm{d}y \int_0^{L_2} \mathrm{d}y' \phi^*_{m,1}(y) G^r_{N,0} \phi_{n,2}(y'). \tag{2.15}$$

In this relation, in addition to the Green's function itself, the leads surface wavefunctions ϕ of transverse mode m and n appear as well as their respective velocities $v_{m(n)}$, which are needed to assure current conservation. The leads' transverse wavefunctions as well as their velocities are obtained during the calculation of their surface Green's functions.

2.3.3. Optimized recursive Green's function method for transmission at different system lengths

The presented RGF method is especially suitable for the calculation of the transmission as a function of the system length. Let us shortly assume two different systems with N and N' slices, respectively. We further assume that the slices $(N - i_0)$, ..., N of the first system are identical with the last i_0 slices, $(N' - i_0)$, ..., N', of the second system. Then it follows directly that the calculated block of the Green's function up to the i_0th step are equal,[1]

$$G^{r,N-i} = G'^{r,N'-i} \forall i \leq i_0. \tag{2.16}$$

Only later in the iteration the Green's functions of the two systems differ. We now want to show how this can be used to calculate the transmission through a system at different lengths. As before we start with the first iteration step $G^{r,N}$. The transmission shall be calculated for lengths L_α, corresponding to different numbers of slices i_α. When encountering one of the slices i_α in the iteration, i. e. having calculated $G^{r,N-i_\alpha}$, instead of continuing with the algorithm, a virtual slice $N - i_\alpha - 1$ is added containing the

[1] From here on we omit the block indices of G^r for better readability.

selfenergy of a second lead. From the thereof calculated Green's function $G^{r,N-i_\alpha-1}_{\text{intermediate}}$ the transmission $T(L_\alpha)$ is calculated via the Fisher-Lee relations as explained before.

After this step the original iteration is continued from $G^{r,N-i_\alpha}$ until either the next selected slice $i_{\alpha'} > i_\alpha$ or the original system's end is reached.

Of course, this scheme is not a possible choice for an arbitrarily shaped scattering region. It is best applicable for nanoribbons or systems with a periodic repetition along the transport direction. However, the choice of the slice i_α has to be done carefully. In the hexagonal of graphene for example, they have to be chosen to fit to the final virtual slice containing the second lead's selfenergy.

This method comes in handy for the treatment of spin relaxation and diffusive transport where we are particularly interested in the transmission as a function of system length. Compared to a direct calculation of several nanoribbons of different lengths this optimizations is faster by at least one order of magnitude. The exact ratio of calculation times depends on the number of supporting points L_α and the total system length.

3. Graphene

Having laid out the grounds for the general description of transport through open mesoscopic systems, we now want to introduce graphene as the specific system to be considered in this thesis.

Graphene is a carbon allotrope consisting of carbon atoms arranged in a honeycomb lattice. It is a building block for other carbon allotropes such as graphite and carbon nanotubes. The stacking of graphene layers eventually leads to the formation of graphite. Carbon nanotubes can be thought of as rolled up graphene nanoribbons. The electronic structure of graphene, hence, is of large importance for the understanding of its derived materials.

Different models are used nowadays to describe the electronic properties of graphene. Among them one finds the description in terms of density functional theory (DFT), the tight-binding model of graphene and the effective Dirac Hamiltonian. Fur reviews and further references see Refs. [58, 59, 34, 60]. We choose the tight-binding model as it enables us to calculate numerically the transport in large systems while retaining the ability to include potentials with fluctuations on the size of an interatomic distance. While for the Dirac Hamiltonian there is basically no limitation to the system size it strictly is only valid for extended graphene in the absence of short-range scatterers. Edges for example constitute such a short range scatterer, but also atomic defects. DFT on the other hand needs large computing capacitance even for small systems of only a few nanometers.

In this chapter we present the tight-binding model for graphene. We also show the effective Dirac Hamiltonian which can be derived from the graphene Hamiltonian. We will use it in certain cases where its application is still justified, since it allows for a clearer description than the tight-binding model. DFT, however, will not be presented here; we just refer to the published literature wherever we make use of results necessary for our calculations.

3.1. Graphene basics

We want to explain several basics about graphene to make the notation used in this thesis clear and to avoid confusion. Graphene consists of carbon atoms arranged in a honeycomb lattice; see Fig. 3.1. As the honeycomb is no Bravais lattice, graphene has to be described as a triangular lattice with a two-atomic basis. We choose as the lattice vectors

$$\boldsymbol{a}_1 = a\begin{pmatrix}1\\0\end{pmatrix} \qquad \text{and} \qquad \boldsymbol{a}_2 = a\begin{pmatrix}\frac{1}{2}\\ \frac{\sqrt{3}}{2}\end{pmatrix}, \tag{3.1}$$

with $a \approx 2.46\,\text{Å}$ being the lattice constant. Atoms in sublattice A are located at the origin of the unit cell, sublattice B is shifted by $\boldsymbol{d} = \frac{a}{\sqrt{3}}(1/2, \sqrt{3}/2)$.

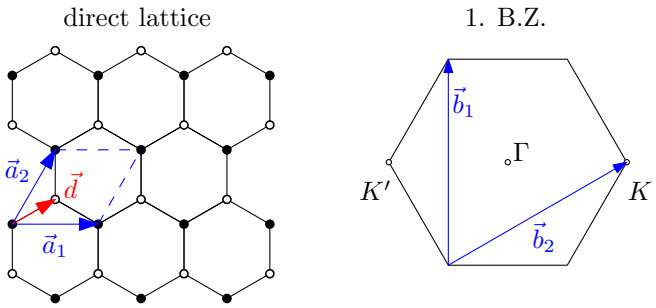

Figure 3.1.: Direct and reciprocal lattice of graphene with their respective unit vectors.

The reciprocal lattice is spanned by the vectors

$$\boldsymbol{b}_1 = \frac{4\pi}{\sqrt{3}a}\begin{pmatrix}0\\1\end{pmatrix} \qquad \text{and} \qquad \boldsymbol{b}_2 = \frac{4\pi}{a}\begin{pmatrix}\frac{\sqrt{3}}{2}\\ \frac{1}{2}\end{pmatrix}. \tag{3.2}$$

The first Brillouin zone (1.B.Z.) has the shape of a hexagon.[1] The corners can be divided into two inequivalent classes not connected by reciprocal lattice vectors. As will be seen later, they play an important role for the bandstructure. They are conventionally labeled $\boldsymbol{K}$ and $\boldsymbol{K}'$. From the equivalent corners we choose

$$\boldsymbol{K} = \frac{4\pi}{3a}\begin{pmatrix}0\\1\end{pmatrix} \qquad \text{and} \qquad \boldsymbol{K}' = \frac{4\pi}{3a}\begin{pmatrix}0\\-1\end{pmatrix}, \tag{3.3}$$

to represent the K-points. Equivalently these points can be called valleys or Dirac points. The meaning of this nomenclature will come clear from the bandstructure presented in the next chapter.

3.2. Tight-binding description

3.2.1. Electrons without spin

The tight-binding model for graphene was first used in 1947 when Wallace calculated the bandstructure of graphite layers [27]. It took several decades until the carbon allotropes finally reached experimental science and Wallace's work came of interest again. Graphene is a building block for fullerenes [61], graphene distorted to form a spherical structure, and carbon nanotubes [62, 63, 64], graphene rolled up. These materials became experimentally available in 1985 (fullerenes) and 1991 (carbon nanotubes), respectively. Accordingly, the tight-binding description of graphene became widely used in these fields. Finally, with the seminal work of Geim and Novoselov [29] on their experiments on exfoliated graphene the rise of graphene began.

The idea behind the easiest tight-binding description of graphene is very simple. It consists of a set of atomic sites i with a single-level state,

$$\mathcal{H}_{\text{isolated}} = \sum_i \varepsilon_i c_i^\dagger c_i, \tag{3.4}$$

[1] The hexagonal shape of the first Brillouin zone is not related to the hexagonal lattice of graphene but it is the Wigner-Seitz cell of the reciprocal lattice obtained from the triangular lattice.

with the creation $c_i^\dagger$ and annihilation c_i operators of electronic states at lattice site i. The electrons on the isolated sites are brought into movement by a kinetic hopping term,

$$\mathcal{H}_0 = -t \sum_{\langle i,j \rangle} c_i^\dagger c_j, \tag{3.5}$$

where the sum is running over nearest neighbor sites i and j. The kinetic hopping term also contains the nearest-neighbor hopping strength t. By assuming all sites to be at the same energy level and performing a global energy shift, only the hopping Hamiltonian (3.5) remains and builds the simplest possible graphene tight-binding Hamiltonian.

The previously completely localized electrons now form a Bloch state extended over the whole crystal minimizing the systems total energy. For extended graphene the periodic repetition of the atomic sites allows for using Bloch's theorem connecting the wavefunction on different sites by a phase factor depending on the crystal momentum $\boldsymbol{k}$ and the relative position of the adjacent sites,

$$c_j^\dagger = \mathrm{e}^{\mathrm{i}\boldsymbol{k}\cdot(\boldsymbol{r}_j - \boldsymbol{r}_i)} c_i^\dagger. \tag{3.6}$$

Omitting the details of the calculations we simply present the resulting energy dispersion,

$$E(\boldsymbol{k}) = \pm t \sqrt{3 + 2\cos(k_x a) + 4\cos\left(\frac{k_x a}{2}\right)\cos\left(\frac{\sqrt{3}k_y a}{2}\right)}, \tag{3.7}$$

plotted in Fig. 3.2. For the calculation the basis of section 3.1 was used. Comparing the bandstructure obtained from the tight-binding Hamiltonian to ab-initio calculations allows for the determination of the size of the hopping parameter. We will use $t = 2.6\,\mathrm{eV}$ which is the value used in literature most often. From Fig. 3.2 the important role of the corners of the 1.B.Z. can be seen where the bands are touching. Accordingly, these points are called valleys, and the low-energy states of graphene can be *valley polarized* in bulk graphene. Short-range disorder and edges, however, might introduce mixing of the two valleys.

Additionally, the dispersion close to the K-points is linear giving rise to a linear expansion of the Hamiltonian in $\boldsymbol{q} = \boldsymbol{k} - \boldsymbol{K}^{(\prime)}$ [28]. The linearization yields an effective Hamiltonian for a two-component wavefunction with the amplitude on the two sublattices as its components. Its form is

$$\mathcal{D} = \hbar v_F \boldsymbol{\sigma} \cdot \boldsymbol{k} \qquad \text{in valley } K \text{ and} \tag{3.8}$$

$$\mathcal{D}' = -\hbar v_F \boldsymbol{\sigma}^* \cdot \boldsymbol{k} \qquad \text{in valley } K'. \tag{3.9}$$

This is the well-known Dirac Hamiltonian for massless fermions. For graphene the sublattice index adopts the role of the real spin, giving rise to the term pseudospin. The Dirac equation for graphene contains pseudospin Pauli matrices, σ. The Fermi velocity of the original Dirac Hamiltonian is the speed of light, whereas in graphene

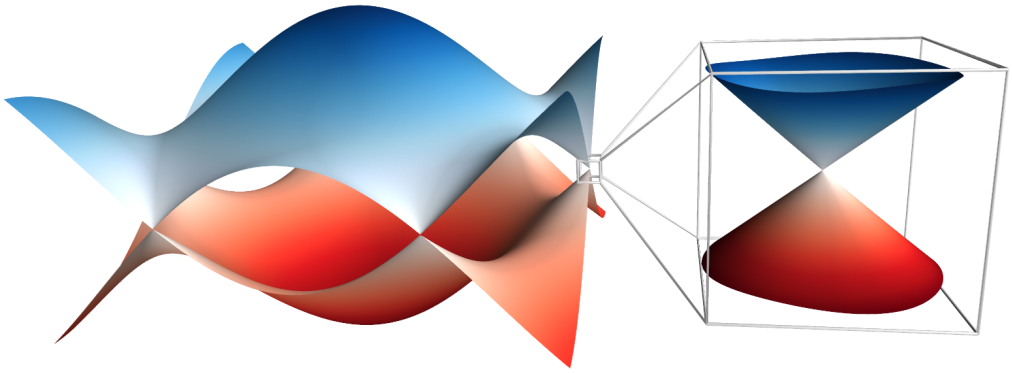

Figure 3.2.: Dispersion of graphene in k-space. Clearly visible are the six touching points. Close to them, the zoomed-in picture emphasizes the linearity close to the *Dirac* points.

a reduced "speed of light", $v_F = \frac{\sqrt{3}}{2\hbar}ta = 10^6\mathrm{m/s}$ is found. The K-points or valleys obtain the additional name Dirac points, used equivalently in literature.

The Dirac Hamiltonian is obtained by a Taylor expansion of the tight-binding Hamiltonian in the close vicinity of the Dirac points up to linear order in momentum [28]. With increasing energy the tight-binding dispersion deviates from the linear Dirac dispersion and becomes anisotropic. It assumes a trigonal shape and this phenomenon is called *trigonal warping*.

In order to account for imperfections in graphene an additional potential is added in the tight-binding Hamiltonian,

$$\mathcal{H}_{\text{potentials}} = \sum_i V_i c_i^\dagger c_i. \tag{3.10}$$

Smooth potentials appear as simple electrostatic potentials in the Dirac Hamiltonian diagonal in pseudospin space. The situation becomes more complicated when the potential contains fluctuations on the atomic lengthscale. For the special case of a potential with alternating sign on the two sublattices,

$$V_i = \begin{cases} +M & \text{on sublattice } A, \\ -M & \text{on sublattice } B, \end{cases} \tag{3.11}$$

sublattice symmetry is broken, and an energy gap is opened at the K points. The corresponding term in the effective Dirac Hamiltonian takes the form of a mass term. In intermediate cases the potential has to be separated into a smooth $V(\boldsymbol{x})$ and a rapidly oscillating $M(\boldsymbol{x})$ potential,

$$\mathcal{D} = \hbar v_F(\tau\sigma_x k_x + \sigma_y k_y) + M(\boldsymbol{x})\sigma_z + V(\boldsymbol{x})\sigma_0. \tag{3.12}$$

Here we introduced the *valley spin* τ being $+1$ (-1) in valley K (K').

3.2.2. Electrons with spin

The spin degree of freedom is added to the tight-binding model by turning the scalar potentials and hopping terms in the Hamiltonian into matrices acting in real spin space. The presented spin-dependent terms will be divided into Zeeman-like terms acting on one lattice site and spin-orbit coupling terms being introduced as spin-dependent hopping terms.

Zeeman like terms come in two ways: the Zeeman term as it is known from text-books, accounting for a para- or ferromagnetic ordering, and a *staggered magnetization*, which in analogy to the previously introduced mass potential is characterized by an opposite sign on the two sublattices. The latter accounts for an antiferromagnetic magnetization. We write these terms as

$$\mathcal{H}_{\text{magnetization}} = \sum_{i;\sigma,\sigma'} c^{\dagger}_{i,\sigma} \left[(\boldsymbol{M}\boldsymbol{s})_{\sigma\sigma'} + (\boldsymbol{M}^z\boldsymbol{s})_{\sigma\sigma'} \right] c_{i,\sigma'}, \tag{3.13}$$

containing the vector of real spin Pauli matrices $\boldsymbol{s}$ and the magnetization $\boldsymbol{M}$ as well as the staggered magnetization $\boldsymbol{M}^z$. The sum is, in addition to the lattice index i, running over spin indices σ and σ'.[2] In the effective Dirac Hamiltonian they act as a Zeeman term, diagonal in pseudospin space, and as a mass term with an additional dependence on the real spin,

$$\mathcal{D}_{\text{magnetization}} = \boldsymbol{M}(\boldsymbol{r}) \cdot \boldsymbol{s}\sigma_0 + \boldsymbol{M}^z(\boldsymbol{r}) \cdot \boldsymbol{s}\sigma_z. \tag{3.14}$$

From the possible spin-orbit coupling terms we restrict ourselves at this point to the presentation of the intrinsic spin-orbit coupling and the extrinsic spin orbit coupling usually denoted Bychkov-Rashba coupling.[3] Both were originally introduced by Kane and Mele in 2005 [65]. They used group theoretical arguments to obtain the form of spin dependent terms in graphene focusing on the intrinsic spin-orbit interaction which is responsible for the quantum spin hall effect in graphene. The graphene Hamiltonian including the intrinsic SOC is usually referred to as the Kane-Mele Hamiltonian and is the first example of a topological insulator. The experimental observation of the quantum spin hall effect in pristine graphene is, however, extremely hard due to the weak intrinsic SOC [41, 66] and with the upcoming of mercury-telluride quantum wells as reliable realization of a two-dimensional topological insulator interest in graphene concerning this field disappeared.

Later Huertas-Hernando used perturbation theory on a multi-band tight-binding model to explain SOC in the π orbitals of graphene [67] and also calculated the strength of the spin-orbit coupling. This calculation was refined by Konschuh et al. [47] with a more complex multi-band tight-binding model including also higher orbitals of the carbon atoms which appeared to have an important effect especially on the intrinsic spin-orbit coupling [41, 47].

[2] We stick to this somewhat confusing notation using $\boldsymbol{s}$ as the vector of Pauli matrices acting in real spin spin space, and σ being the real spin index within the tight-binding description and the pseudospin Pauli matrices in the Dirac theory to be consistent with literature. As the use of Dirac and tight-binding theory is strictly separated the meaning of σ should always be unambiguous.

[3] The terms extrinsic and Bychkov-Rashba spin are used interchangeably within thesis. Often it is also simply refered to as the Rashba term.

Shortly summarizing this approach, the basis is the atomic SOC in carbon,

$$\mathcal{H}_{\text{SO, atom}} = \Delta_{\text{carbon}} \boldsymbol{L} \cdot \boldsymbol{s} = \Delta_{\text{carbon}} \left(\frac{L_+ s_- + L_- s_+}{2} + L_z s_z \right). \tag{3.15}$$

Apparently, coupling between electrons of opposite spin involves also coupling of electrons with different orbital angular momentum and, hence, the inclusion of not only the p_z orbitals. The Hamiltonian is reduced to separated blocks for σ and π orbitals, where only the latter are relevant for electron transport, by performing a Löwdin transformation as explained in appendix B of Ref. [47]. This allows for effective spin dependent hopping terms between the π orbitals. In pristine graphene only the spin-orbit coupling connects p_z orbitals to p_x and p_y orbitals and, hence, a spin-dependent hopping is only present as a second order process in the atomic spin-orbit coupling strength, Δ_{carbon}. This intrinsic coupling vanishes due to the symmetry of the graphene lattice for nearest neighbors so the result is an effective next-nearest neighbor coupling,

$$\mathcal{H}_{\text{SO}} = \mathrm{i} \frac{\Delta_{\text{SO}}}{3\sqrt{3}} \sum_{\langle\langle i,j \rangle\rangle;\sigma,\sigma'} v_{ij} c^\dagger_{i,\sigma} (s_z)_{\sigma\sigma'} c_{j,\sigma'}. \tag{3.16}$$

The parameter $v_{ij} = \pm 1$ depends on the orientation of two nearest neighbor bonds connecting sites i and j. Δ_{SO} sets the strength of the intrinsic SOC. It has a very small value of $24\,\mu$eV [41, 47] since it can only be derived by an expansion up to second order in Δ_{carbon}/t.

A direct coupling between p_z and other carbon orbitals, triggered for example by a curvature of the graphene surface or the influence of an external electric field, allows for an effective first order spin-dependent coupling of the π orbitals, called extrinsic or, in analogy to the nomenclature used in conventional two-dimensional electron or hole systems, Bychkov-Rasha spin-orbit coupling,

$$\mathcal{H}_{\text{BR}} = \frac{2\mathrm{i}\lambda_{\text{BR}}}{\sqrt{3}} \sum_{\langle i,j \rangle;\sigma,\sigma'} c^\dagger_{i,\sigma} \left[(\boldsymbol{d}_{ij} \times \boldsymbol{s})_z \right]_{\sigma\sigma'} c_{j,\sigma'}. \tag{3.17}$$

Its strength λ_{BR} depends on the curvature radius or the size of the external electric field, respectively. It explicitly depends on the vector $\boldsymbol{d}_{ij}$ connecting sites i and j.

In the effective Dirac Hamiltonian their analogs appear as spin-pseudospin coupling terms,

$$\mathcal{D}_{\text{SO}} = \Delta_{\text{SO}} \tau s_z \sigma_z, \text{ and} \tag{3.18}$$

$$\mathcal{D}_{\text{BR}} = \lambda_{\text{BR}} (\tau \sigma_y s_x + \sigma_x s_y). \tag{3.19}$$

It can be seen that the intrinsic SOC formally resembles the staggered magnetization except for the additional valley index τ. Accordingly, it opens a gap at the Dirac points [see Fig. 3.3 (a)]. The size of the corresponding gap is given by Δ_{SO}, which also defines the energy range the quantum spin Hall state could be observed within. Spin degeneracy is kept by the intrinsic SOC, but it is lifted by the Bychkov-Rashba term. In contrast to the original Bychkov-Rashba coupling it does not depend on the momentum but rather creates a constant splitting of the spin-subbands; see Fig.

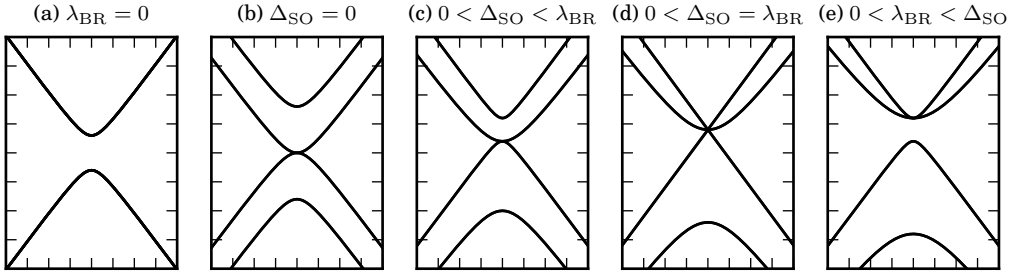

Figure 3.3.: Energy dispersion of graphene in the vicinity of the K-points. The bandstructure is plotted for different scenarios. (a) and (b) show the cases of only one kind of spin-orbit coupling being finite. In figures (c) - (e) we show the case of competing strenghts of the intrinsic and the Bychkov-Rashba SOC. See text for further details.

3.3 (b). For the case of comparable Δ_{SO} and λ_{BR} the corresponding bandstructures are plotted in Fig. 3.3 (c) - (d). The bandstructure obtained from the Dirac Hamiltonian is

$$\varepsilon_{\mu\nu} = \mu\lambda_{\mathrm{BR}} + \nu\sqrt{(\hbar v_F k)^2 + (\lambda_{\mathrm{BR}} - \mu\Delta_{\mathrm{SO}})^2}, \tag{3.20}$$

with indices μ for the spin subband and ν for the electron and hole branches. In the case of pure Bychkov-Rashba spin-orbit coupling the splitting of the spin-subbands is clearly visible close to the Dirac points. The bandstructure is symmetric with respect to the Fermi level. This symmetry is broken under the assumption of a finite intrinsic SOC, but still the dispersion stays gapless as long as $\Delta_{\mathrm{SO}} < \lambda_{\mathrm{BR}}$; see Fig. 3.3 (c). In the particular case where $\Delta_{\mathrm{SO}} = \lambda_{\mathrm{BR}}$ we observe a triply degenerate state at $E = \lambda_{\mathrm{BR}}$ for $k = 0$. Two of the participating bands show a linear dispersion similar to the Dirac bandstructure shifted by λ_{BR}; see Fig. 3.3 (d). A gap is opened when $\Delta_{\mathrm{SO}} > \lambda_{\mathrm{BR}}$; see Fig. 3.3 (e).

From the Dirac Hamiltonian for valley K we can calculate the eigenstates,

$$\Psi_{\mu\nu} = \frac{1}{C_{\mu\nu}} \begin{pmatrix} 1 \\ \frac{\varepsilon_{\mu\nu} - \Delta_{\mathrm{SO}}}{\varepsilon_0} \mathrm{e}^{\mathrm{i}\varphi} \\ -\mu\mathrm{i}\frac{\varepsilon_{\mu\nu} - \Delta_{\mathrm{SO}}}{\varepsilon_0} \mathrm{e}^{\mathrm{i}\varphi} \\ -\mu\mathrm{i}\mathrm{e}^{-2\mathrm{i}\varphi} \end{pmatrix} \tag{3.21}$$

in a spin-pseudospin basis with components $(A\uparrow, B\uparrow, A\downarrow, B\downarrow)$. The momentum is included through its orientation φ with respect to the x-axis and implicitly through the dispersion $\varepsilon_{\mu\nu}$ and the spin-less dispersion ε_0. The normalization constant is $C_{\mu\nu} = \left\{2\left[1 + \left(\frac{\varepsilon_{\mu\nu} - \Delta_{\mathrm{SO}}}{\varepsilon_0}\right)\right]\right\}^{1/2}$. The spin expectation value $\langle \boldsymbol{s} \rangle$ calculated from the solutions of the Dirac Hamiltonian is orthogonal to the momentum lying in the graphene plane, independent of the value of Δ_{SO}. The same texture of the spin-orbit field is obtained for two-dimensional electron gases in the presence of Bychkov-Rashba

coupling. Strictly spoken, there exist fluctuations of the spin expectation value on an atomic lengthscale [68] which are masked in the Dirac approximation.

In the next section we want to give a short example of how spin dependent terms can be important for electron transport in graphene by revisiting the Klein tunneling in the presence of spin-orbit coupling.

3.3. Klein tunneling in the presence of spin-orbit coupling

We want to use the presented formalism to investigate Klein tunneling in graphene. Klein tunneling is a phenomenon originally known from particle physics [69, 70]. It describes the possibility of a massless Dirac fermion to form a propagating state in a classically forbidden region. This is in sharp contrast to particles obeying the Schrödinger equation which would form an evanescent mode in a classically forbidden region. Massless Dirac fermions, however, can travel within potential barriers as their own anti-particle. At normal incidence the transmission is even perfect.

For electrons in graphene this property has been predicted [71, 72, 73] and observed [31, 74] within various signatures. We can calculate the transmission probability for a potential step in graphene to illustrate the meaning of Klein tunneling. Let's consider an electron approaching the potential step with a momentum $\boldsymbol{k} = (k_x, k_y)$. For arbitrary potential height V, at Fermi energy E_F the transmission probability of an electron propagating towards the potential step at an angle φ, where the angle is given by $\tan\varphi = k_y/k_x$, can be calculated as

$$T(\varphi, \theta) = \frac{2\cos\varphi\cos\theta}{1+\cos(\varphi+\theta)}. \tag{3.22}$$

The outgoing solution's angle θ is given by

$$\sin\theta = \frac{\sin\varphi}{1-v}, \tag{3.23}$$

with $v = V/E_F$. The case of normal incidence, $\varphi = \theta = 0$, results in $T = 1$ for every choice of the potential height v. Moreover, when $0 < v < 2$, the incoming wave is perfectly reflected for $\sin\varphi > |1-v|$. In Fig. 3.4 we plotted the transmission as a function of incoming angle for several values of the potential height v. The longitudinal momentum follows from the calculation of the leads' selfenergies. The transverse momentum is obtained from the manually defined Bloch phase factor $\exp(\mathrm{i}k_B W)$. It contains the width W of the periodically repeated supercell and the Bloch momentum k_B which for the lowest transverse mode fulfills $k_B W = k_y W$.[4] The question we want to ask in this section is how this behavior changes in the presence of spin-orbit coupling. An extension to *p-n* junctions in the presence of SOC is a natural step and is, additionally, appropriate to demonstrate the possibility of the numerical framework used within this thesis. The results presented here are in accordance with the ones presented in Ref. [75]. Reference [36] contains extracts from this section and

[4] At larger energies or for wider systems higher harmonics of the transverse wavefunction can play a role. Instead of $k_B W = k_y W$ we have to consider $k_B W = 2n\pi + k_y W$ with a positive integer n.

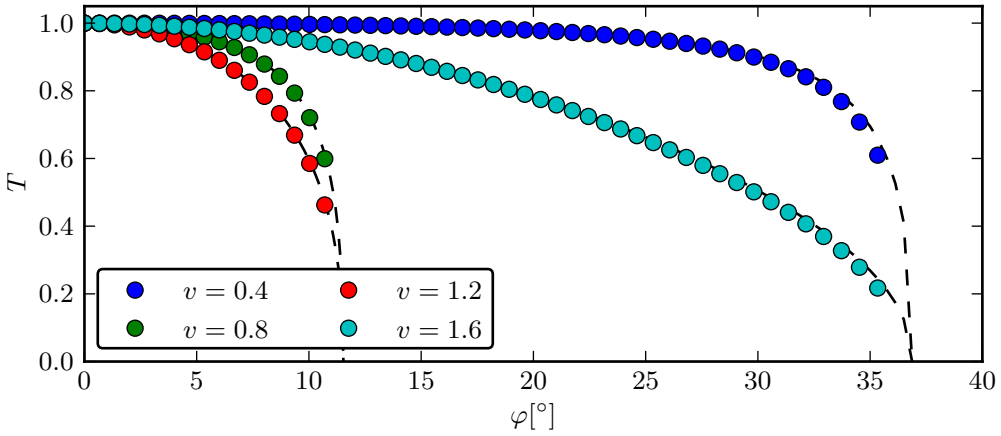

Figure 3.4.: Transmission T through a bipolar graphene p-n junction as a function of the electron's incidence angle φ. We plotted the analytic result, eqn. (3.22), as dashed lines. Colored circles are the numerical results.

gives further insight into the physics of graphene p-n-p junctions in the presence of Bychkov-Rashba SOC and for smooth p-n junctions.

A striking feature of massless Dirac particles is the perfect transmission through potential steps at normal incidence. The intrinsic spin-orbit coupling acts similar to a mass term and, hence, leads to a suppressed transmission. The introduction of Rashba SOC modifies dispersion and eigenstates allowing at least partial transmission of a propagating state. By increasing λ_{BR} the gap induced by the intrinsic SOC decreases. At the point where the gap closes, $\lambda_{\mathrm{BR}} = \Delta_{\mathrm{SO}}$, we encounter again two linearly dispersing bands; see Fig. 3.3 d). We checked that, for a wide range of parameters, for those bands the potential step is transparent. In Fig. 3.5 we plotted the reflection probability through a potential step with a step height of $V_0 = -2 \cdot \Delta_{\mathrm{SO}}$ at an energy of $E_F = -0.5 \cdot \Delta_{\mathrm{SO}}$. Left of the potential step we set $V(x, y) = 0$, $\forall x < 0$, in the region right of the step we have a finite constant potential $V(x, y) = V_0$, $\forall x \geq 0$. The Rashba coupling is varied from 0 to $1.2 \cdot \Delta_{\mathrm{SO}}$. For these values there is one open hole-like channel in the lead with zero potential and in the lead with the finite potential there are two open electron-like states.

In analogy with the spinless case we also investigated the angle-dependence of transmission through the graphene p-n junction in presence of SOC. This case, too, has been investigated analytically [75] and our numerical calculation confirms the results of the Dirac approximation within the full tight-binding model. The parameters are again choosen in a way that the left lead supports only one hole-like state. In the right lead the spin-orbit coupling leads to a splitting of the Fermi surface into two circles with different Fermi momenta. The conservation of the transverse component of the momentum implies that at sufficiently large energy one of the two spin subbands turns into an evanescent state in the n-doped region of the p-n junction.

We calculate the transmission as a function of incidence angle by varying the transverse momentum k_y. The curve is continuous but not smooth where $k_y = |\boldsymbol{k}_{\mathrm{o},1}|$, the

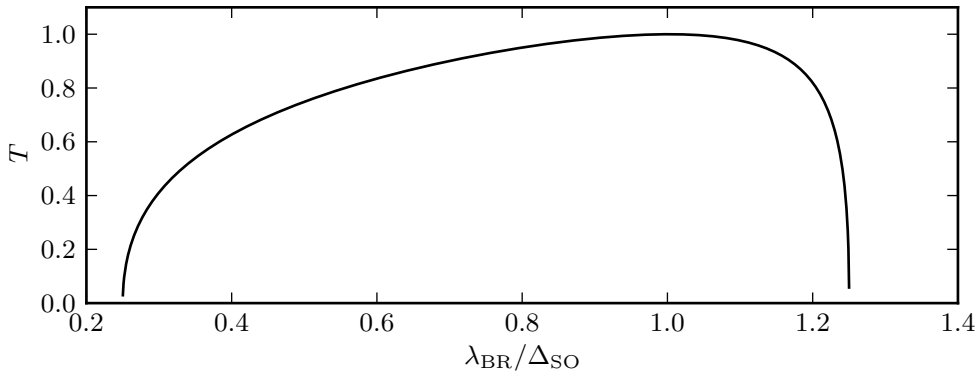

Figure 3.5.: Transmission probability of a bipolar graphene p-n junction with SOC as function of the Rashba coupling strength. The strength of the intrinsic SOC and the Fermi level have been fixed for this calculation.

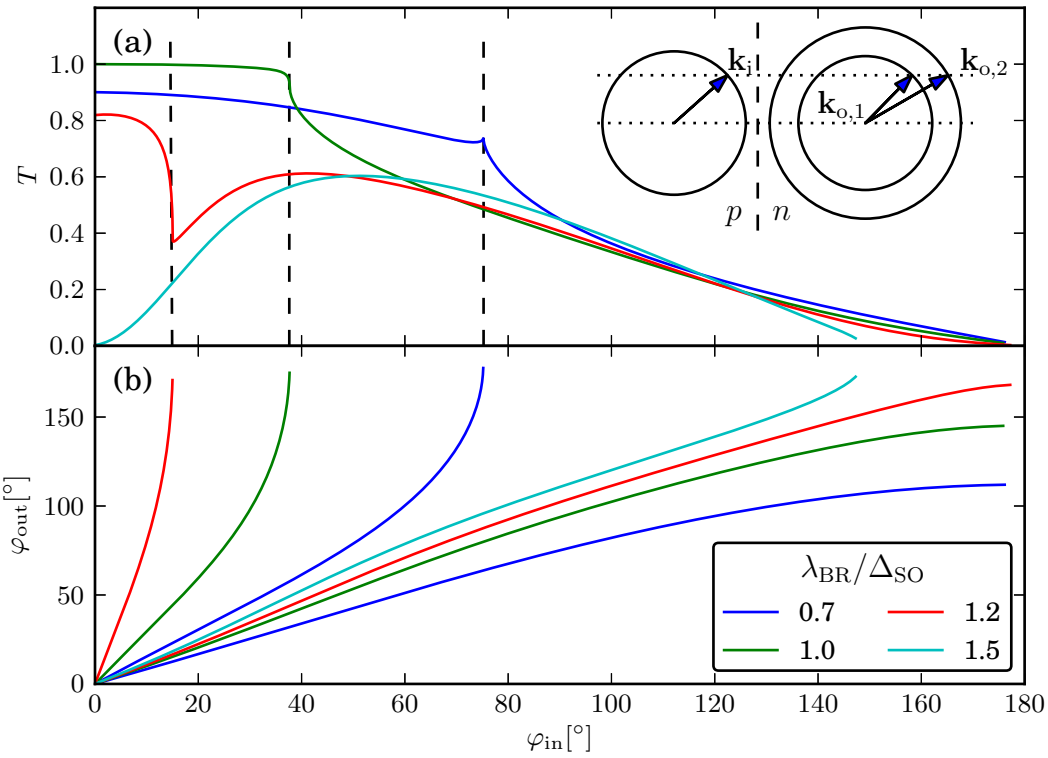

Figure 3.6.: (a) Transmission function of a bipolar p-n junction with SOC as a function of incidence angle. The inset shows a sketch of the different momenta involved in the scattering problem. (b) Momenta direction of the outgoing modes with respect to the k_x axis as a function of the angle of the incoming electron's momentum.

momentum of the inner Fermi circle in the right lead. In Fig. 3.6 we plotted both transmission and the angle of the outgoing states as function of incidence angle. We also included a sketch of the Fermi surface in both the p- and the n-region. In a nutshell, spin-orbit coupling has, in this example, a crucial influence on electron transport beyond a pure modification of the spin transport. The most striking feature of Klein tunneling in graphene, the perfect transmission at normal incidence, is destroyed, and spin-subband splitting leads to a complex non-differentiable angular dependence of the transmission.

The techniques presented here can also be used to calculate the solution of more complex while still analytical solvable problems. Such studies have been performed within Ref. [36] for p-n-p junctions which are encountered more often in experiments than p-n junctions, and for smooth potential changes instead of sharp potential steps. For smooth potentials it turns out that the analytical solutions possibly deviate from tight-binding calculations and are only valid qualitatively.

3.4. Summary

In this chapter, we pointed out which model will be used throughout this thesis for describing electrons in graphene. We calculated its bandstructure and showed how spin-dependent terms alter its electronic properties. Eventually we chose the Klein tunneling to illustrate the particularity of electrons in graphene and how their resemblance to massless Dirac particles is important. This example was also used to demonstrate the capabilities of our numerical simulations.

In the following two parts we use the concepts presented up to this point to investigate transport in complex graphene structures and nanostructures. The questions we address comprise the influence of spin-orbit coupling on spin transport. In the first part, we will show how small localized magnetic moments lead to very strong spin relaxation. Finally, in the second part, we will address the formation of magnetic moments by electron-electron interactions and their influence on electron transport.

Part I.

Spin Relaxation in Graphene

4. Introduction

The field of graphene spintronics was started in 2007 by Tombros et al. [76] from the University of Groningen. Pioneering works in the field of spintronics have been published in Groningen before like the spin injection in all-metallic spin valve devices [15]. The idea of using the spin Hanle effect [13], i. e. the response of the spin dynamics to an external magnetic field, was first successfully used in Groningen to obtain the spin relaxation time in aluminum [15]. In Ref. [76] the successful injection of spin polarized electrons in graphene was demonstrated by the presence of a notable spin-valve effect and a clear Hanle spin precession. The reported spin relaxation length at 77K was approximately 2μm extracted both from spin-valve and Hanle spin-precession measurements. This number provided confidence about using graphene for further spintronics applications where spin relaxation lengths do not even need to be that high because typical lengths within which information has to be transferred can be significantly smaller than that.

Nevertheless, the corresponding spin relaxation was shorter than expected. Given a diffusion constant of $D = 2.2 \times 10^{-2}\mathrm{m}^2/\mathrm{s}$ [76] the corresponding spin relaxation time was $\tau_s \approx 90$ps. While further experiments were performed [77, 78, 79, 80, 81] and other groups joined the research on spintronics in graphene [82, 83, 84] a critical theoretical debate on spin relaxation in graphene was started by Huertas-Hernando et al. [85] and later substantiated by Ertler et al. [86] finding spin relaxation times between 10ns and 1μs. Apparently, there is a large discrepancy between experiment and theory. The model used in Ref. [86] was based on Bychkov-Rashba spin-orbit coupling due to electric fields created by charges trapped in the nearby substrate. This contributes to the spin relaxation via randomization of the dynamics in k space, the Dyakonov-Perel mechanism, and due to randomization of SOC in real space, which in this thesis will be denoted as the *Sherman mechanism* [37, 38].

Further analytic models and predictions about spin relaxation in graphene were published in the next years. An explicit derivation of the Sherman spin relaxation rate for graphene was given in Ref. [87]. In Refs. [88, 89, 39, 90, 91] kinetic spin Bloch equations are used to analyze different scenarios of spin relaxation focusing on Dyakonov-Perel spin relaxation and the Sherman spin relaxation mechanism. A work explicitly treating the Elliot-Yafet spin relaxation mechanism in graphene can be found in Ref. [92].

Mechanisms we will not investigate are subsumed under the term inelastic scattering, like electron-electron scattering [88] and electron-phonon scattering [90, 93, 94]. Electron-electron interaction is a strong source of spin relaxation but the calculated spin relaxation rates are still too low to explain the experiments [88]. Electron-phonon interactions yield sufficiently large spin relaxation rates only at room temperature [90]. Refs. [93, 94] find even lower spin relaxation rates and Fratini et al. [94] state that

the spin relaxation times they calculated are indeed very large and should rather be seen as an upper limit than the actually measured one.

From all the presented works, only Ref. [39] claims to have found the dominant spin relaxation mechanism. They can calculate sufficiently large spin relaxation rates to explain experimental data from their KSBEs at high adatom concentrations. The debate, however, is not finished yet and the dominant role of spin-orbit disorder and the Sherman mechanism is still doubted. A new proposal was made by Kochan et al. [33] suggesting resonant scattering from magnetic impurities as the dominant spin relaxation mechanism.

We will investigate different scenarios of spin relaxation in graphene. The approach followed in this thesis is the use of numerical spin transport simulations. They allow for a less idealized modeling of quantum transport in graphene than the analytic works and enable us to check analytic results within the given parameters. Moreover, effects not feasible within analytic approaches can be investigated. The latter include potential fluctuations on an atomic length scale, e. g. from adsorbed adatoms [40, 95, 42, 43], or the inclusion of intrinsic SOC, which also may be strongly enhanced by the adsorption of certain adatoms [96].

The main questions addressed in this part of the thesis are the importance of adatoms for the high spin relaxation rates and to find signatures of the adatom-induced spin relaxation to identify their role in the experiments, which, up to now, have always been categorized in terms of Elliot-Yafet or Dyakonov-Perel mechanism.

We start by defining and thoroughly investigating Elliot-Yafet and Dyakonov-Perel spin relaxation mechanisms in Chapter 5. The investigation of a toy model representing the presence of adatoms forming covalent bonds with the carbon atoms in graphene is the topic of Chapter 6. In Chapter 7, the last chapter of this part of the thesis, we present a more realistic model of adatoms also including the formation of magnetic moments and resonant scattering as suggested in Ref. [33].

5. Dyakonov-Perel and Elliot-Yafet mechanisms in graphene

In the long debate about the spin relaxation in graphene, two mechanisms were most often held responsible: the Elliot-Yafet (EY) mechanism [97, 98] and the Dyakonov-Perel (DP) mechanism [99]. They are covered in standard textbooks and reviews on spin transport (e. g. Refs. [100, 101]), so we will only shortly sketch their mode of action.

In this chapter we show how the aforementioned spin relaxation mechanisms can be modeled and investigated numerically in graphene. Analytical works treating both mechanisms exist for graphene. These preliminary works will be compared to our numerical results. This rather fundamental investigation is necessary to judge the numerical results obtained for more complex scenarios of spin transport in the following chapters. Moreover a numerical approach allows for a more thorough investigation as the only limitation is the system size. For instance, analytic works on spin relaxation in graphene are always restricted to the case of pure Bychkov-Rashba interaction neglecting intrinsic SOC. There exist, however, situations where the intrinsic SOC cannot be neglected and plays an important role for spin relaxation.

5.1. The Dyakonov-Perel mechanism in graphene

We use a semiclassical picture to explain the DP mechanism considering electrons that are moving freely in a solid until being scattered by an impurity. The scattering event randomizes the electron's momentum keeping its phase and spin information intact. Between two scattering events a k-dependent effective magnetic field $\mathbf{\Omega}_k$ rotates the spin. As the magnetic field depends on the direction and, possibly, the size of the momentum k, after each scattering event the precession axis is randomized. In the semiclassical picture an electron can travel along different paths from point A to point B, each involving different scattering sites. The different spin phases accumulated along these paths can eventually lead to a reduced spin polarization at the final point.

Notably, while this mechanism requires the presence of disorder in the system, a very strong disorder actually keeps the spin information intact. This phenomenon is called *motional narrowing*. Its regime is characterized by the spin precession length $\ell_{\mathrm{SO}} \propto 1/|\mathbf{\Omega}_k|$ being large compared to the mean-free path l_{tr} so that between two scattering events only a small rotation takes place. Similarly in quasi-ballistic nanowires with a lateral constriction width W small compared to the spin precession length ℓ_{SO} the Dyakonov-Perel mechanism is suppressed.

The spin rotation accumulated between two scattering events is on average $\delta\varphi = \tau_p \Omega_k$ where τ_p is the elastic scattering time. We neglect fluctuations of Ω_k along the Fermi circle and rather assume a spin splitting only depending on $|\boldsymbol{k}|$. $\delta\varphi$ is also the

step width of a random walk the electron's spin is performing. Spin relaxation occurs on a time scale τ_S where the mean rotation reaches unity,

$$1 = \delta\varphi\sqrt{\tau_S/\tau_p} \qquad \Rightarrow \tau_S = 1/(\Omega_k^2\tau_p). \tag{5.1}$$

According to Eq. (5.1) the Dyakonov-Perel mechanism is usually accounted the dominant spin-relaxation mechanism when the spin relaxation time is found to scale linearly with the inverse of the momentum relaxation time.

It helps to understand basic spin transport properties of a given system. Moreover, an appropriate system for numerical simulations can be defined clearly and be controlled well. Hence, it will serve as the first example of spin-dependent transport simulations in graphene. To this end we impose a long-range disorder potential on our systems which originates from charges in the vicinity of the graphene sheet. The particular choice of the disorder potential is

$$V_{\mathrm{dis}}(\boldsymbol{x}) = \sum_{i=1}^{N_{\mathrm{dis}}} V_i \mathrm{e}^{-|\boldsymbol{x}-\boldsymbol{x}_i|^2/2\sigma_{\mathrm{dis}}^2}. \tag{5.2}$$

The N_{dis} charges act on the graphene electrons through a screened Coulomb potential. V_i is the height of the potential emanating from a single impurity and is chosen uniformly within the range $[-V_0, V_0]$. The decay length σ_{dis} is a constant of the disorder potential. V_0, σ_{dis} and the impurity concentration are chosen in a way that the mean free path is consistent with experimental data.[1]

In DP spin relaxation the Larmor frequency determines the size of $\Omega_{\boldsymbol{k}}$. Hence, the spin relaxation rate is directly related to the energy splitting of the spin sub-bands. Systems without Rashba SOC, where states of opposite spin are still degenerate, are insensitive to the DP spin relaxation mechanism. For systems with an extrinsic spin-splitting such that the intrinsic contribution can be neglected, $\lambda_{\mathrm{BR}} \gg \Delta_{\mathrm{SO}}$, the splitting for both electron and hole branch is $\Delta\varepsilon = 2\lambda_{\mathrm{BR}}$. Competing sizes of both intrinsic and extrinsic SOC lead to a complex k-dependence of the spin splitting close to the Dirac point. Away from the Dirac point the splitting is given by

$$\Delta\varepsilon = 2\lambda_{\mathrm{BR}}\left[1 - \Delta_{\mathrm{SO}}/(\hbar v_F k)\right] \tag{5.3}$$

assuming both $\lambda_{\mathrm{BR}}, \Delta_{\mathrm{SO}} \ll \hbar v_F k$. This value eventually converges against the case of pure extrinsic SOC for even larger energies.

The spin precession time can be calculated from the Larmor frequency at the given subband splitting $\Delta\varepsilon$,

$$\tau_{\mathrm{SO}} = \frac{1}{\omega_{\mathrm{Larmor}}} = \frac{\hbar}{\Delta\varepsilon} = \frac{\sqrt{3}ta}{2v_F\Delta\varepsilon}. \tag{5.4}$$

[1] Normally V_0 is approximately $0.1t$, σ_{dis} is several lattice constants, the number of charges is a fraction of the total number of lattice sites, usually somewhere between 0.01 and 0.2. Then our calculations are consistent with spin transport experiments where the mean free path is usually between 10nm and 100nm.

The spin precession length, i. e. the distance an electron has covered when its spin completes a full rotation, is

$$\ell_{\mathrm{SO}} = v_F \tau_{\mathrm{SO}} = \frac{\sqrt{3}}{2\Delta\varepsilon} ta. \tag{5.5}$$

For Bychkov-Rashba type spin splitting with $\lambda_{\mathrm{BR}} = 3 \times 10^{-6} t \approx 10\mu\mathrm{eV}$, which corresponds to a constant electric field of approximately $1\mathrm{V/nm}$, we calculate a spin-orbit length of $\ell_{\mathrm{SO}} \approx 35\mu\mathrm{m}$ and a spin precession time of $\tau_{\mathrm{SO}} \approx 33\mathrm{ps}$. Reported mean free paths are of the order $\mathcal{O}(10\mathrm{nm})$, so the scattering time is approximately 50fs. Consequently motional narrowing is expected and a spin relaxation time in the order of microseconds.

A comprehensive study of the Dyakonov-Perel mechanism in graphene has been published in Ref. [89] using the ansatz of kinetic spin Bloch equations (KSBE) predicting an exponential decay of an initial spin polarization. Let the x-axis be the transport axis and y the transverse in-plane component. The z-axis is orthogonal to the graphene plane. If the initial spin polarization had a fraction within the x-z plane, in addition to the exponential decay of spin polarization, an oscillation of the spin orientation should be seen. Notably this was not expected from the two-component drift-diffusion model formerly used to describe spin transport [100, 102]. The different components of the spin polarization vector evolve like

$$S_y(L) \propto \mathrm{e}^{-L/L_{S\perp}} \begin{pmatrix} 0 \\ 1 \\ 0 \end{pmatrix}, \tag{5.6}$$

$$S_{x/z}(L) \propto \mathrm{e}^{-L/L_{S\parallel}} \begin{pmatrix} \cos(L/L_{\mathrm{SO}}) \\ 0 \\ \sin(L/L_{\mathrm{SO}}) \end{pmatrix}. \tag{5.7}$$

The spin dynamics is, thus, governed by the phenomenological lengths L_{SO}, the spin oscillation length, and $L_{S\perp}/L_{S\parallel}$, the perpendicular and parallel spin relaxation lengths.[2] The boundary conditions were chosen in a way that $\lim_{L\to\infty} S_\mu(L) = 0$ and $S_\mu(0) = S_0 \hat{e}_\mu$ where μ indicates the spin injection/detection axis x, y or z and $\hat{e}_\mu$ is the unit vector pointing along that direction.

For a numerical calculation of the spin density we calculate the spin-dependent transmission amplitudes and from them extract the charge transmission,

$$T = \mathrm{Tr}(t^\dagger t), \tag{5.8}$$

and the spin transmission,

$$T_\mu = \mathrm{Tr}(t^\dagger s_\mu t s_\mu), \tag{5.9}$$

respectively. The normalized spin transmission $T_{S\mu} = T_\mu/T$ is proportional to the spin polarization and - in an equilibrium situation - to the spin density. Hence, as a

[2] The terms perpendicular and parallel refer to the relation to the orientation with respect to the average spin-orbit field, which in our example is the y-axis.

function of system length, it can be used to extract the spin relaxation length, $L_{S\perp}$ or $L_{S\parallel}$, respectively, the spin oscillation length L_{SO} and, indirectly, the corresponding times $\tau_{S\parallel}$, $\tau_{S\perp}$ and τ_{SO}. We therefore assume, motivated from KSBE, $T_{S\mu}$ to be of the form

$$T_{Sy} = \mathrm{e}^{-L/L_{S\parallel}}, \tag{5.10}$$

$$T_{Sx/z} = \mathrm{e}^{-L/L_{S\perp}} \cos\left(\frac{L}{L_{\mathrm{SO}}}\right). \tag{5.11}$$

The charge transmission in the diffusive regime is given by [103]

$$T = \frac{N}{1 + \frac{2L}{\pi l_{\mathrm{tr}}}}. \tag{5.12}$$

With the number of open channels N given as an external parameter, from the numerical calculation the mean free path l_{tr}, the spin oscillation length L_{SO} and the spin relaxation length L_S can be extracted. For the calculation of the transmission as a function of the system length we use the optimized recursive Green's function method presented in section 2.3.3.

Zhang and Wu [89] have calculated the perpendicular spin relaxation length

$$L_{S\perp} = \frac{2\sqrt{7}}{(2\sqrt{2}-1)\sqrt{1+2\sqrt{2}}} \frac{\hbar v_F}{2\lambda_{\mathrm{BR}}}, \tag{5.13}$$

the parallel spin relaxation length

$$L_{S\parallel} = \frac{\hbar v_F}{2\lambda_{\mathrm{BR}}}, \tag{5.14}$$

and the spin oscillation length

$$L_{\mathrm{SO}} = \frac{\hbar v_F}{2\lambda_{\mathrm{BR}}}, \tag{5.15}$$

for systems with purely Rashba spin-orbit coupling. The spin oscillation length L_{SO} is the same as the spin precession length, ℓ_{SO}, calculated from the Larmor frequency in equation (5.5). $L_{S\perp}$, $L_{S\parallel}$ and L_{SO} were obtained in the strong scattering limit, i. e. momentum relaxation only due to electron-impurity scattering. They are independent of the scattering time. The resulting anisotropy of the spin relaxation lengths is $L_{S\parallel}/L_{S\perp} \approx 0.68$ differing from the result obtained from two-component drift-diffusion equations [100]. In the drift-diffusion approach a distinction was made between spins polarized in- or out-of-plane with respect to the 2D system. Out-of-plane polarized spins were expected to loose the phase on average twice as fast as in-plane polarized spins.

Exemplary curves obtained from our calculations are shown in Fig. 5.1 for systems with a very high constant Rashba SOC, $\lambda_{\mathrm{BR}} = 10^{-3}t = 2.5\mathrm{meV}$. We chose a large spin-orbit coupling so spin relaxation is clearly visible by the naked eye. An oscillation

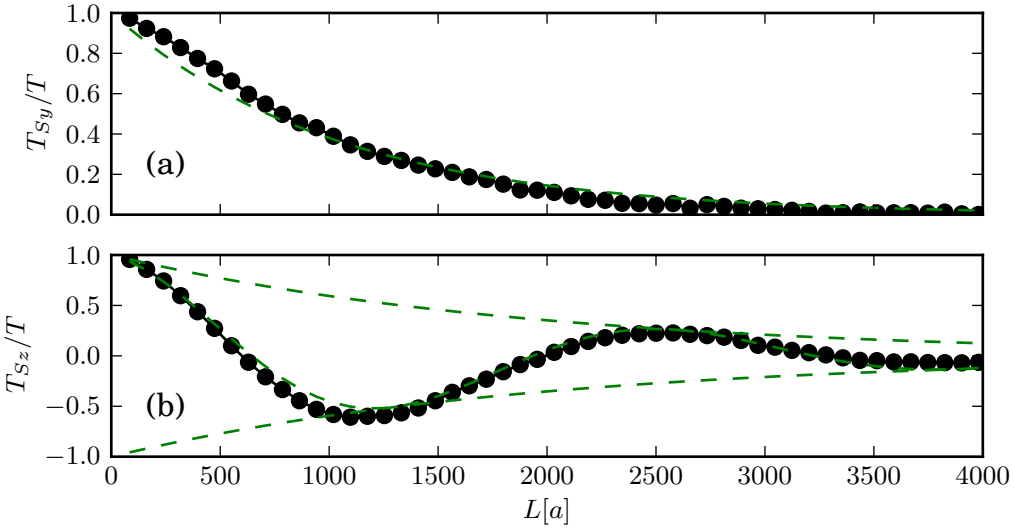

Figure 5.1.: Spin transmission as a function of system length. (a) *Parallel* spin transmission identifiable by the pure exponential decay in contrast to the case of (b) *perpendicular* spin transmission. In the latter case the spin transmission is described by an exponentially damped cosine. See text for further details.

as predicted by Ref. [89] is visible and we, additionally, find the oscillation length to be constant over a wide energy range and for different values of the mean-free path. While qualitatively the anisotropy is correctly predicted from the KSBE ansatz a quantitative disagreement regards the anisotropy factor, which we find to be exactly 0.5. Moreover the spin relaxation length on our numerical simulations is larger than the one obtained from KSBEs by a factor 2 – 4.

We analyzed the DP spin relaxation also in the presence of intrinsic SOC and found, according to our predictions, that Δ_{SO} only weakly affects the spin relaxation length. In Fig. 5.2 we compare the spin relaxation length to the size of the gap, Eqn. (5.3). Deviations are only present for large values of Δ_{SO} where the condition $\lambda_{\mathrm{BR}}, \Delta_{\mathrm{SO}} \ll E_F$ is not fulfilled anymore. The anisotropy ratio is 0.5.

In the major part of our numerical calculations the spin relaxation length stays constant when the mean free path changes. We calculate momentum and spin relaxation times from the corresponding lengths using

$$\tau_p = l_{\mathrm{tr}}/v_F, \tag{5.16}$$

$$\tau_S = L_S^2/D, \tag{5.17}$$

with the diffusion constant $D = \frac{1}{2} v_F l_{\mathrm{tr}} = \frac{1}{2} v_F^2 \tau_p$. As expected from the drift-diffusion equations [100] as well as from the KSBE [89] the spin relaxation length scales as the inverse of the momentum relaxation time, $\tau_S \propto 1/\tau_p$.

To summarize, we investigated the Dyakonov-Perel mechanism in graphene showing the coexistence of spin precession and relaxation confirming results from Zhang and

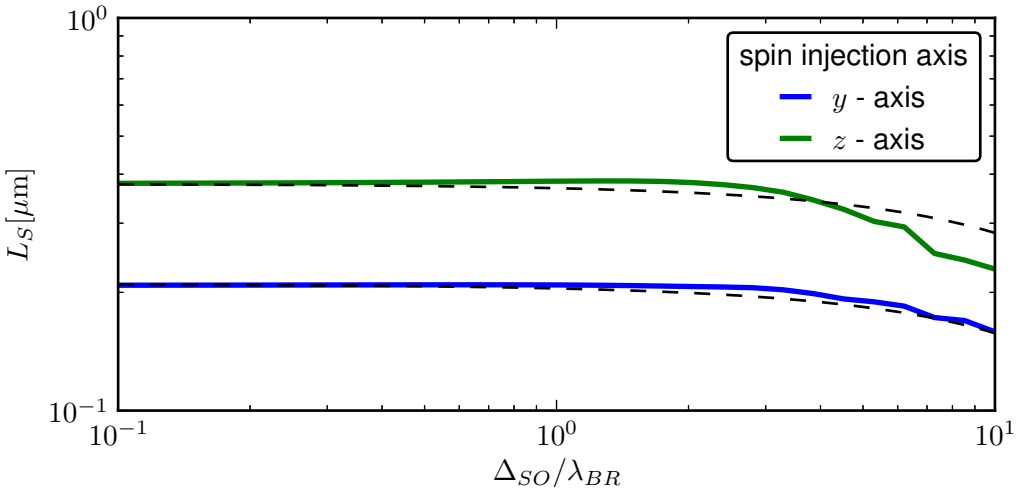

Figure 5.2.: Spin relaxation length for different strengths of the intrinsic SOC, Δ_{SO}, and for different injection axes. The Bychkov-Rashba SOC is fixed at $\lambda_{\mathrm{BR}} = 0.001t$. Dashed lines are proportional to the spin-splitting. Assumptions made in the calculation of the gap size lead to deviations when Δ_{SO}/E_F approaches unity.

Wu obtained from KSBE [89]. Due to approximations made in the analytical derivation of the spin dynamics no exact correspondence was found in the observation of the anisotropy of the spin relaxation. The analytical result can nevertheless be used to estimate the approximate spin relaxation length (up to a factor of $2-4$) in graphene due to the DP mechanism. For strong disorder potentials, $V_0 = 0.2t$, we observe a deviation from the expected relation between scattering time and spin relaxation time, and also the dependence on Δ_{SO} is more pronounced. We already mentioned that for those values the calculation of the spin splitting is not easy anymore but is also hints at a crossover to the Elliot-Yafet mechanism which is described in detail in the next section.

5.2. Elliot-Yafet mechanism in graphene

When the Dyakonov-Perel mechanism is dominant spin relaxes by precession in an effective magnetic field between scattering events. The opposite case – spin gets changed simultaneously with momentum scattering – is called Elliot-Yafet spin relaxation mechanism.

In Elliot's original work [97] and Yafet's later extension [98], spin relaxation emanates from states with only approximately defined spin

$$|k,+\rangle = \alpha_k|\uparrow\rangle + \beta_k|\downarrow\rangle, \tag{5.18}$$

where $|\alpha_k| \gg |\beta_k|$ allowing the assignment as spin up or down. This admixture is assumed due to the presence of a weak spin-orbit coupling. Scattering off a potential,

diagonal in spin space, has a finite spin flip probability due to this spin superposition with the transition rate calculated via Fermi's Golden rule,

$$\tau_s^{-1} \propto \tau_p^{-1} \frac{\lambda^2}{\Delta E^2}. \tag{5.19}$$

Here, λ is the strength of the spin orbit coupling, and ΔE is the separation to the nearest band with the same transformation properties. The linear relation between momentum and spin relaxation rate shown in equation (5.19) is the signature leading to a classification for a system showing EY type spin relaxation in contrast to DP type spin relaxation with an indirect proportionality between τ_s and τ_p [see Eq. (5.1)].

Ochoa et al. [92] published a relation similar to equation (5.19) for graphene with Bychkov-Rashba SOC,

$$\tau_s^{-1} \propto \frac{(2\lambda_{\mathrm{BR}})^2}{E_F^2} \tau_p^{-1}, \tag{5.20}$$

calling it the *Elliot relation for graphene*. We investigate the EY spin relaxation mechanism numerically. The system used for that purpose is defined by a Hamiltonian

$$\mathcal{H} = \mathcal{H}_0 + \mathcal{H}_{\mathrm{SOI}}(\Delta_{\mathrm{SO}}, \lambda_{\mathrm{BR}}) + \mathcal{H}_{\mathrm{Zeeman}}(\boldsymbol{B}) + V \sum_i \mathrm{e}^{-\frac{x_i^2+y_i^2}{\xi^2}} |i\rangle\langle i|. \tag{5.21}$$

Electrons are scattered at the potential defined in the last term of the Hamiltonian centered around $(x, y) = (0, 0)$ with a Gaussian decay and a decay length ξ. The system is subjected to a background spin-orbit coupling ($\propto \lambda_{\mathrm{BR}}$ and $\propto \Delta_{\mathrm{SO}}$). We calculate all scattering amplitudes $t_{ij,\sigma\sigma'}$ and the total spin flip probability

$$T_{\mathrm{sf}} = \sum_{i,j;\sigma} |t_{ij,\sigma(-\sigma)}|^2. \tag{5.22}$$

The spin index σ is assigned with respect to a quantization axis defined by the system or to some spin expectation values, respectively. To avoid the influence of edges we assume periodic boundary conditions in the lateral direction.

To verify the Elliot-Yafet relation given in Ref. [92] we defined a system with only Bychkov-Rashba background SOC. Spin up and down are defined by the eigenstates of the Hamiltonian. Hence, the polarization axis is orthogonal to the electron's momentum. Numerically calculating the spin-flip probability, Eq. (5.22), we find

$$T_{\mathrm{sf}} \propto E^{-2} \text{ and} \tag{5.23}$$

$$T_{\mathrm{sf}} \propto \lambda_{\mathrm{BR}}^2, \tag{5.24}$$

as predicted by Ochoa et al. [92]. The numerical results are shown in Fig. 5.3. The given system, however, does not allow to determine the relation between scattering time and spin relaxation time.

A serious shortcoming of this method shall be mentioned. We calculated the scattering probability between the two spin-subbands but only in this particular case we can identify it with a spin flip. For instance, calculation of charge currents usually requires an integration over different angles of incoming electrons and, thus, over modes

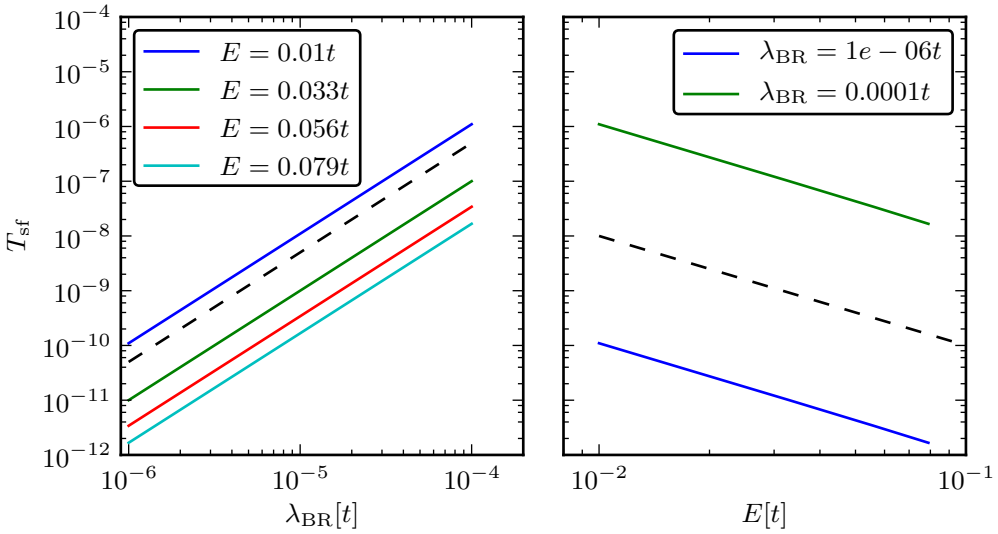

Figure 5.3.: The verification of the Elliot relation predicted in Ref. [92] showing the spin flip probability both as a function of energy E and Bychkov-Rashba SOC λ_{BR}. The predicted course is indicated by dashed lines.

in different spin states. Another example where this interpretation of spin relaxation fails is the case of a nanoribbon of sufficiently large width or high energy such that it carries several transverse modes. In that case each mode is classified along an individual spin quantization axis not necessarily parallel to the axes of other modes due to the different velocity directions. Again, calculating the total transmission implies summing over different spin states.

We next show numerical results for systems where the provided Elliot relation (5.20) holds and extend it to other, more general systems. To this end we include a small Zeeman term, which lifts the spin degeneracy in the leads and provides a spin polarization axis. Spin-up and -down states are, however, only approximately defined [see equation (5.18)] in the presence of SOC and provided that the Zeeman splitting exceeds the strength of the SOC. The term spin flip will be used with respect to these states. The effect of the Zeeman field on the scattering is negligible as the length an electron propagates during a Larmor oscillation is several orders above the system length.

Revisiting Eqn. (5.20) in this case reveals that the given Elliot relation also holds for more general systems when the spins are polarized along a magnetic field parallel to the z-axis. The spin flip probability then is a function of $(\lambda_{\mathrm{BR}}/E_F)^2$. We find a similar relation also when considering only the *intrinsic* SOC for spins polarized *in* the graphene plane. For that case we find within the whole parameter range under consideration

$$T_{\mathrm{sf,\,x}} \propto \frac{\Delta_{\mathrm{SO}}^2}{E_F^2}. \tag{5.25}$$

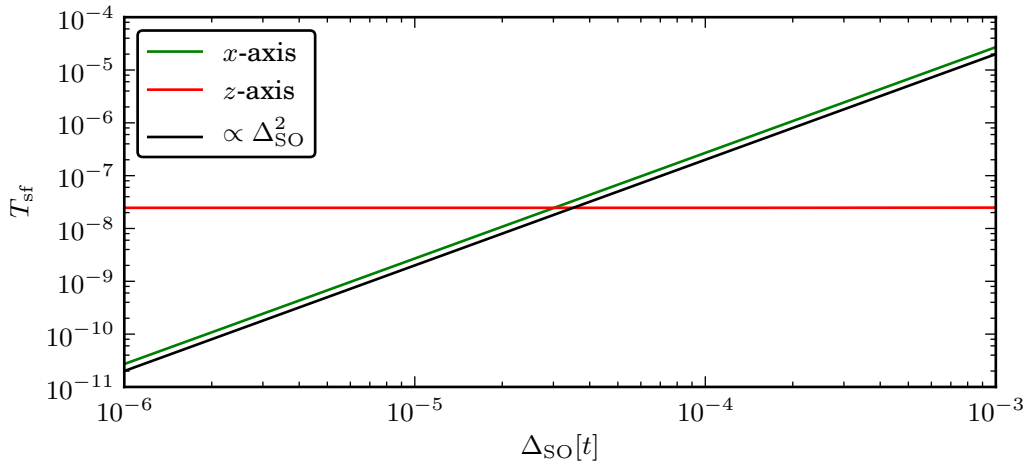

Figure 5.4.: Anisotropy of the Elliot-Yafet mechanism. In-plane (green) and out-of-plane (red) spin flip probability are numerically calculated for different values of the intrinsic SOC. The strength of Bychkov-Rashba SOC is $\lambda_{\mathrm{BR}} = 3 \times 10^{-5} t$.

Spins polarized out-of-plane are never influenced from the intrinsic SOC in this EY setup also when considering both intrinsic and Bychkov-Rashba SOC at the same time. The influence of the intrinsic SOC is visualized in Fig. 5.4.

One has to be cautious that deviations from this simple Elliot relation exist. In-plane spin relaxation with Bychkov-Rashba SOC is insensitive to energy changes,

$$T_{\mathrm{sf},x} \propto \lambda_{\mathrm{BR}}^2 E_F^0. \tag{5.26}$$

In the case of both types of SOC it is insensitive to a change in λ_{BR} as long as the strength of the Bychkov-Rashba SOC is comparable to Δ_{SO}.

Anticipating the following chapter we also comment on spin scattering due to a potential off-diagonal in spin space,

$$\begin{aligned}\mathcal{H}_{\mathrm{off}} =& \mathrm{i}\frac{\delta\Delta_{\mathrm{SO}}}{3\sqrt{3}} \sum_{\langle\langle i,j\rangle\rangle;\sigma,\sigma'} \mathrm{e}^{-\frac{\bar{x}_{ij}^2+\bar{y}_{ij}^2}{\xi^2}} v_{ij} c_{i,\sigma}^\dagger (s_z)_{\sigma\sigma'} c_{j,\sigma'} \\ &+ \frac{2\mathrm{i}\delta\lambda_{\mathrm{BR}}}{\sqrt{3}} \sum_{\langle i,j\rangle;\sigma,\sigma'} \mathrm{e}^{-\frac{\bar{x}_{ij}^2+\bar{y}_{ij}^2}{\xi^2}} c_{i,\sigma}^\dagger \left[(\boldsymbol{d}_{ij} \times \boldsymbol{s})_z\right]_{\sigma\sigma'} c_{j,\sigma'}.\end{aligned} \tag{5.27}$$

Here $(\bar{x}_{ij}/\bar{y}_{ij})$ are the coordinates of the center between lattice sites i and j. A locally increased curvature or several types of adatoms might induce such an increased local spin-orbit coupling like hydrogen or fluorine which form a covalent bond with the carbon atoms in the graphene sheet. The induced spin-orbit coupling can reach values up to several meV leading to a spin-flip rate several orders of magnitude larger than calculated for scatterers diagonal in spin space.

We calculate the spin scattering rates for the perturbations off-diagonal in spin space from the Dirac Hamiltonian terms,

$$\mathcal{D}_{\mathrm{SO}} = \tau\delta\Delta_{\mathrm{SO}} \begin{pmatrix} 1 & 0 & 0 & 0 \\ 0 & -1 & 0 & 0 \\ 0 & 0 & -1 & 0 \\ 0 & 0 & 0 & 1 \end{pmatrix}, \text{ and} \tag{5.28}$$

$$\mathcal{D}_{\mathrm{BR}} = \mathrm{i}\delta\lambda_{\mathrm{BR}} \begin{pmatrix} 0 & 0 & 0 & (1-\tau) \\ 0 & 0 & (1+\tau) & 0 \\ 0 & -(1+\tau) & 0 & 0 \\ -(1-\tau) & 0 & 0 & 0 \end{pmatrix}, \tag{5.29}$$

using Fermi's golden rule and assuming $\boldsymbol{k}$-isotropic scattering:

in-plane	out-of-plane
$w_{\mathrm{SO}} = \frac{2\pi}{\hbar}\frac{2(\delta\Delta_{\mathrm{SO}})^2}{\hbar v_F}\rho(E_F)$,	$w_{\mathrm{SO}} = 0$,
$w_{\mathrm{BR}} = \frac{2\pi}{\hbar}\frac{2(\delta\lambda_{\mathrm{BR}})^2}{\hbar v_F}\rho(E_F)$, and	$w_{\mathrm{BR}} = \frac{2\pi}{\hbar}\frac{4(\delta\lambda_{\mathrm{BR}})^2}{\hbar v_F}\rho(E_F)$.

Scattering rates are proportional to the density of states $\rho(E_F)$. Apparently, also the EY mechanism exhibits anisotropic spin relaxation. It is, however, sensitive to the intrinsic spin-orbit coupling over the whole parameter range in contrast to DP spin relaxation.

Numerically we find that the spin-flip probability T_{sf} depends quadratically on the strength of the local spin-orbit coupling (both intrinsic and Bychkov-Rashba). In contrast to the aforementioned spin relaxation rate for background SOC it does not depend on Fermi energy. In Fig. 5.5 we plot exemplary data for a system with Bychkov-Rashba SOC both as a background term and a perturbation. We see a competition between the background SOC and the one induced in the scattering region. Spin flip is dominated by the stronger parameter. The background SOC is, however, not expected to reach values as high as the ones induced from adatoms.

From these calculations it is hard to judge about the EY mechanism as the relevant spin relaxation mechanism. Spin flip probabilities from background SOC are very low. A simple extrapolation neglecting correlations between different scattering sites cannot result in a notable spin relaxation. In the last section we saw that spin relaxation while still weak could nearly completely be attributed to the Dyakonov-Perel mechanism. On the other hand, a local enhancement of spin-orbit coupling significantly increases spin flip. We keep the question open for further treatment in this thesis.

5.3. Summary

We have investigated both the Dyakonov-Perel and the Elliot-Yafet spin relaxation mechanisms in graphene. Dyakonov-Perel spin relaxation is characterized by an indirect proportionality between spin and momentum relaxation rate. For a careful choice of the spin polarization the spin signal is showing cosine-shaped oscillations.

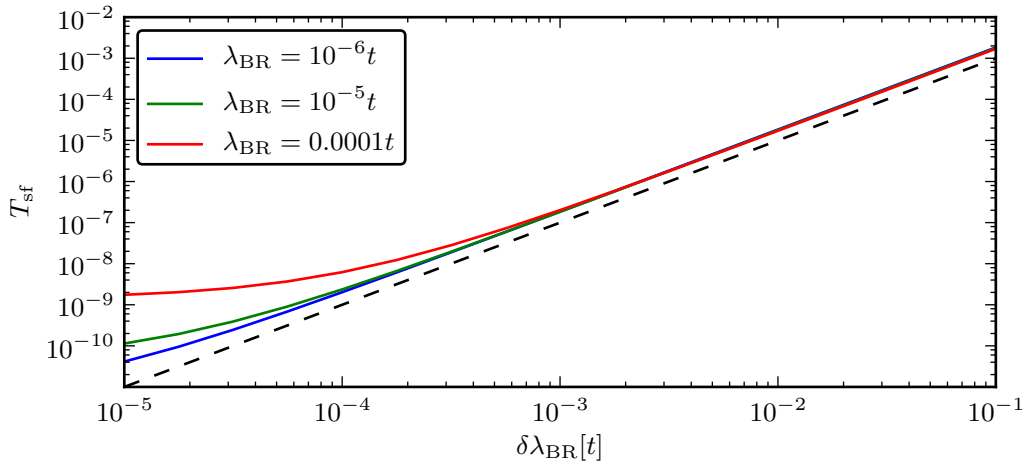

Figure 5.5.: Spin flip probability T_{sf} as a function of a Bychkov-Rashba perturbation $\delta\lambda_{\mathrm{BR}}$ at different values of the background SOC. For the numerical calculation we used the perturbation, Eq. (5.27), with $\delta\Delta_{\mathrm{SO}}$ set to zero. All curves eventually converge against the quadratic dependence on the Rashba impurity strength (dashed line).

We also showed how spin can be scattered by spin-independent potentials, leading to Elliot-Yafet spin relaxation.

For the distinction in experiments a back-gate-sweep is performed to measure the spin-relaxation time at different momentum scattering times and to choose the dominant spin relaxation mechanism by their relation. We showed that due to the complex energy dependence of the Elliot-Yafet spin flip probability this procedure might be misleading. Indeed the calculations for graphene show predominantly characteristics of Dyakonov-Perel spin relaxation, which has seldomly been observed experimentally [104], while from experiments, mostly, the Elliot-Yafet mechanism is favored [76, 78, 79, 81, 105].

A more profound analysis could be given by comparing spin relaxation with respect to different polarization axes and possibly for different values of the spin-orbit parameters. Anisotropic spin relaxation is also known from electron systems with parabolic dispersion. There it can be used, for instance, to compare the ratio between Rashba and Dresselhaus SOC parameters. An equality of those is required to observe the persistent spin helix (PSH) [22, 21] which is a phenomenon observable in two-dimensional electron systems where Dyakonov-Perel spin relaxation is completely suppressed. In graphene there is no Dresselhaus term [106], the intrinsic spin-orbit coupling is known to keep the average direction of the effective magnetic field unchanged so no PSH is to be expected for graphene.

In any case studying anisotropic spin relaxation in graphene could help getting answers about the dominant spin relaxation mechanism. Experimental obstacles have prevented such an analysis so far. The form anisotropy of the usually used cobalt or palladium contacts prefers magnetization in one direction. Forcing the magnetization of the contacts to another direction implies very strong magnetic fields. Altering the

intrinsic SOC is also not feasible. Optical spin injection and detection is a possible route for this analysis.

On the other hand, the discrepancy between experimental and theoretical spin relaxation rate suggests other mechanisms or sources of spin relaxation. The influence of locally increased SOC was already shortly addressed in the context of Elliot-Yafet spin relaxation For local spin splitting in the range of $\mathcal{O}(10^{-3}t)$ a substantial increase of the spin-flip probability, T_{sf}, was obtained. Such a system acts as a building block for spin-orbit disorder which will be the focus of the next chapter.

6. The Sherman spin relaxation mechanism in graphene

In the previous chapter we presented the Dyakonov-Perel and the Elliot-Yafet spin relaxation mechanism and showed that in graphene they, alone, cannot be responsible for spin relaxation in graphene. To explain the spin relaxation rate in the whole temperature range, Refs. [88, 90] refer to locally increased SOC from adatoms which is randomized in position space. In this chapter we want to focus on the inclusion of such spin-orbit fields fluctuating in position space. While the Dyakonov-Perel mechanism is based on randomization of the time-evolution of an electron state in $\boldsymbol{k}$-space, the randomization of the spin-orbit coupling in position space also potentially relaxes spin. This mechanism was proposed for graphene by Dugaev et al. [87] based on works for two-dimensional electron gases with a parabolic dispersion [37, 38]. Nowadays it is often referred to as *Sherman* spin relaxation mechanism after the author of Ref. [37] who also contributed to Refs. [38, 87]. Dugaev et al. [87] considered local fluctuations of a Bychkov-Rashba SOC due to rippling of the graphene surface. SOC from ripples implies a large correlation length for randomized spin-orbit parameters with low peak values. Moreover, ripples create Rashba coupling while leaving the intrinsic SOC untouched.

Adsorbed adatoms are another possibility to obtain a position dependence of the SOC. Castro-Neto and Guinea suggested a phenomenological model for adatoms on graphene which locally induce a partial sp^3-hybridization of the carbon orbitals, and, hence, increase the SOC around the adatoms [40]. They, too, predicted an enhancement of Rashba coupling only. Weeks et al. [96] showed that the presence of heavy adatoms – indium and thallium – alters bandstructure and eigenstates in a way equivalent to the intrinsic SOC. In the case of adatoms the correlation length of the *spin-orbit disorder* is much shorter than for the ripples considered by Dugaev et al. Peak values of the spin-orbit coupling will, however, be larger by several orders of magnitude.

In this chapter we present the effective model used for our numerical calculations and show how the results for the short-ranged Rashba disorder can be compared to the results for long-range Rashba disorder. Similar investigations have been performed by Zhang and Wu [39] using a KSBE ansatz. Our results shall be compared to those results and will be distinguished from the spin relaxation mechanisms presented in the last chapter.

We will start in the next section by introducing the analytic description of the Sherman model and adopt it to the short range spin-orbit disorder induced by adatoms in the following chapter. Our numerical calculations will be compared to analytical predictions afterwards. Finally, we will summarize that and explain why this model also fails to explain the high spin relaxation rate found in spin transport experiments in graphene.

6.1. Sherman spin relaxation mechanism

To obtain the spin relaxation rate by randomized spin-orbit coupling, E. Sherman and his co-workers [37, 38, 87] calculated the time evolution of the spin-density matrix $s_{\boldsymbol{k}}$ from the kinetic equation for the density matrix $\rho_{\boldsymbol{k}}$. This technique is originally known from Ref. [107] where it was used to include the effects of SOC in the study of spin currents. The relevant parts are

$$\frac{\partial \rho_{\boldsymbol{k}}}{\partial t} = \frac{1}{\mathrm{i}\hbar}[\mathcal{H}_{\mathrm{pre}}, \rho_{\boldsymbol{k}}] + \left(\frac{\partial \rho_{\boldsymbol{k}}}{\partial t}\right)_{\mathrm{coll}}, \tag{6.1}$$

where the right-hand side contains the von-Neumann equation for the density matrix, describing spin precession $\mathcal{H}_{\mathrm{pre}}$, and spin relaxation due to scattering, the so-called collision integral. The Boltzmann equation defines the time dependence of the density matrix of momentum $\boldsymbol{k}$. Different momenta are coupled through the collision integral. We neglected further terms usually included for the description of drift and diffusion. These would define the spatial distribution of electron- and spin-density. We, however, want to restrict ourselves to the time-evolution of the spin polarization.

It is instructive to oppose the Sherman spin relaxation mechanism to the Dyakonov-Perel mechanism. The latter one was based on the randomization of the particle movement in $\boldsymbol{k}$ space and, hence, on a randomization of the effective magnetic field an electron is experiencing during its propagation. For the Sherman mechanism a position dependence of the spin-orbit coupling is important leading to a randomization of the effective magnetic field during electron propagation and to spin relaxation even for constant wave vector $\boldsymbol{k}$.

The idea is shortly summarized in a classical picture. In a diffusive mesoscopic conductor different paths connect the two leads, but an individual effective spin-orbit coupling along each path leads to different phases for different paths. Summing over these phases the spin signal becomes reduced in comparison to the incoming state. We will sketch calculations from Ref. [87] for the collision integral for random Rashba coupling,

$$\left(\frac{\partial \rho_{\boldsymbol{k}}}{\partial t}\right)_{\mathrm{coll}} = -\frac{4k s_z \hat{s}_{\boldsymbol{k}}}{\pi v_F \hbar^2} \int_0^{2k} \frac{C(q)}{\sqrt{4k^2 - q^2}} \mathrm{d}q. \tag{6.2}$$

Here, $C(q)$ is the Fourier transform of the two-point correlation function of the spin-orbit disorder. In that case without electrostatic potential disorder, the collision integral is proportional to the spin-density matrix appearing in the separation of the density matrix,

$$\rho_{\boldsymbol{k}} = \rho_{0,\boldsymbol{k}} + s_z \hat{s}_{\boldsymbol{k}}, \tag{6.3}$$

between the spin-independent part, $\rho_{0,\boldsymbol{k}}$, and the spin-dependent part, $\hat{s}_{\boldsymbol{k}}$. The $\boldsymbol{k}$-space correlator of the Rashba disorder from Ref. [87] is

$$C(q) = 2\pi \langle \lambda^2 \rangle \xi^2 \mathrm{e}^{-q\xi}, \tag{6.4}$$

where ξ is the correlation length of the Rashba disorder and $\langle\lambda^2\rangle = \int \mathrm{d}\boldsymbol{r}\lambda^2(\boldsymbol{r})$. Analogous calculation have been performed by Zhang and Wu [39] who obtain a slightly different result,

$$C(q) = 4\pi\langle\lambda^2\rangle\xi^2\mathrm{e}^{-\xi^2q^2}, \tag{6.5}$$

as they assume a different real space correlation of their disorder.

The obtained spin relaxation rate following Dugaev et al. [87] is

$$\frac{1}{\tau_S} = \frac{4\pi k_F}{v_F\hbar^2}\langle\lambda^2\rangle\xi^2[I_0(2k_F\xi) - L_0(2k_F\xi)], \tag{6.6}$$

with I_0 and L_0 being the modified Bessel and Struve functions of zeroth order. The expression can be approximated for both the semiclassical ($k\xi \gg 1$) and the quantum case ($k\xi \ll 1$),

$$\frac{1}{\tau_S} = \frac{4\xi}{v_F\hbar^2}\langle\lambda^2\rangle \begin{cases} 1 & k\xi \gg 1, \\ \pi k\xi & k\xi \ll 1. \end{cases} \tag{6.7}$$

Zhang and Wu obtain an equivalent result. In the following section the calculation of the spin relaxation rate shall be adopted to short-range spin-orbit disorder induced by adatoms.

6.2. Impurity-Induced Spin-Orbit Coupling in Graphene

Castro-Neto and Guinea suggested the presence of adatoms to enhance the spin-orbit coupling locally [40]. This increased SOC then drops to zero already at a distance of one lattice constant from the adatom. Calculations suggest that spin relaxation due the spin-orbit coupling from adsorbed adatoms is the the dominant spin relaxation mechanism in graphene as both the Elliot-Yafet as well as the Dyakonov-Perel signatures of spin relaxation in experiments can be reproduced [39]. Further, in Ref. [39] spin relaxation time obtained from numerically solving the kinetic spin Bloch equations are in line with experimental data if parameters are chosen appropriately. We want to use a tight-binding model including such spin-orbit impurities to gain an understanding of the involved spin relaxation mechanism and to judge on its ability to lead to a high spin relaxation rate.

Bychkov-Rasha spin-orbit coupling in graphene (see chapter 3.2) relies on an extrinsic coupling between different carbon orbitals. Castro-Neto and Guinea suggested a local sp^3 hybridization of the carbon atoms which form a covalent bond with the adatoms. In the sp^3 hybridized state the π bonds encounter a strongly enhanced spin-orbit coupling. The coupling should reach values up to 5meV. They parametrize the amount of hybridization with the factor A ranging from 0 for sp^2 hybridized atoms to 0.5 for fully sp^3 hybridized atoms. The local value of the SOC is $\lambda(\boldsymbol{r}) = A(\boldsymbol{r})\sqrt{3(1-A^2(\boldsymbol{r}))}\lambda_{\mathrm{SO}}^{at}$, where $\lambda_{\mathrm{SO}}^{at}$ is the atomic spin-orbit coupling strength of carbon ($\approx$ 7meV). In contrast to Ref. [87] where a low SOC strength but large cor-

relation length was assumed, Ref. [40] leads to the opposite scenario. We re-derived the Sherman spin relaxation rate for this case in Appendix C,

$$\frac{1}{\tau_S(k)} = \frac{2\pi\langle\lambda^2\rangle}{v_f\hbar^2}\xi \begin{cases} 8\xi k & \xi k \ll 1 \\ \frac{3}{2} & \xi k \gg 1 \end{cases} \tag{C.12}$$

which is the same as for the correlations considered in Refs. [87, 39] except for some prefactors. While the slowly varying SOC from ripples implies the semiclassical limit, the increased SOC from adatoms decays over only a few interatomic distances where the quantum case is relevant. For that case we obtain

$$\frac{1}{\tau_S} = \frac{16\pi\xi_{\mathrm{Ad}}^2 k_F}{v_F\hbar^2}\langle\lambda^2\rangle = \frac{16\pi\xi_{\mathrm{Ad}}^2 E_F}{v_F^2\hbar^3}\langle\lambda^2\rangle = \frac{6\pi^2\xi_{\mathrm{Ad}}^4\lambda_{\mathrm{Ad}}^2\rho_{\mathrm{Ad}}E_F}{v_F^2\hbar^3}, \tag{6.8}$$

where λ_{Ad} is the peak strength of the spin-orbit interactions induced by the adatoms.

In this model approach we simulate the presence of adatoms by choosing a set of N_{Ad} carbon sites as centers of the spin-orbit disorder. We explained the possibility of increased Rashba SOC but we also know about the possibility of increased intrinsic SOC by adatoms [96]. Consequently, both intrinsic and Bychkov-Rashba SOC are altered in the vicinity of the N_{Ad} sites. The strength of this modifications decays as

$$f(r) = A(r)\sqrt{3(1 - A^2(r))}, \tag{6.9}$$

where r is the distance from a center of the spin-orbit disorder, and the hybridization parameter $A(r)$ exhibits an exponential decay $A(r) = \exp(-r/\xi_{\mathrm{Ad}})$ with the decay length ξ_{Ad}. As the p_z electrons in the sp^3 hydridized atoms are involved in σ-bonds instead of the π-bonds as in pristine graphene, we would also expect momentum scattering from the presence of adatoms which is represented by an electrostatic potential with the same functional form as the spin-orbit parameters. The influence of these parameters shall be investigated in the following sections as well as the influence of non-physical parameters like adatom density ρ_{Ad} and decay length ξ_{Ad}.

6.3. Numerical Results

We use the recursive Green's function method presented in sections 2.3.2 and 2.3.3 to calculate transmission T, and spin transmission $T_{s\mu}$ with respect to quantization axis μ. We include the local fluctuations of the potentials due to adatoms presented in the last section and a background disorder potential already previously used before in this thesis,

$$V_{\mathrm{dis}}(\boldsymbol{x}) = \sum_{i=1}^{N_{\mathrm{dis}}} V_i \mathrm{e}^{-|\boldsymbol{x}-\boldsymbol{x}_i|^2/2\sigma_{\mathrm{dis}}^2}. \tag{5.2}$$

An impression of the potential landscape is given in Fig. 6.1. Mean-free path l_{tr}, spin relaxation length L_S and spin precession length L_{SO} are extracted according to equations (5.10)–(5.12). In Fig. 6.2 we show the average spin transmission for one set of parameters where the average is calculated with respect to different configurations of

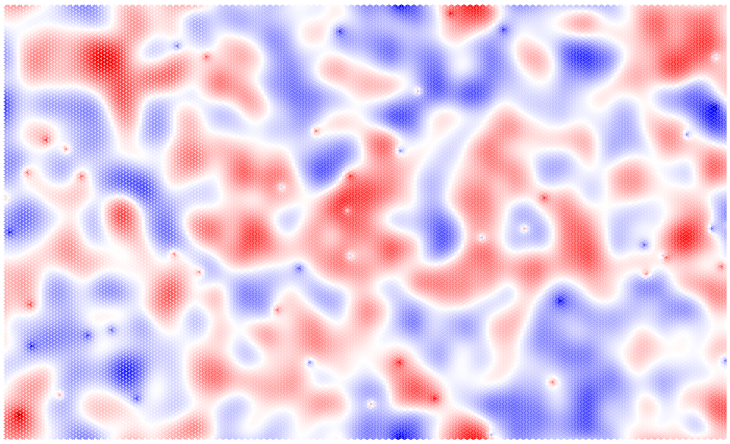

Figure 6.1.: Visualization of the potential landscape in our simulated graphene systems. We have a long-range background-potential leading to the formation of electron-hole puddles. The adatoms induce a short-range potential. In the sketch we can see p- and n-doped regions in red and blue color, respectively. They are separated by white charge-neutrality lines.

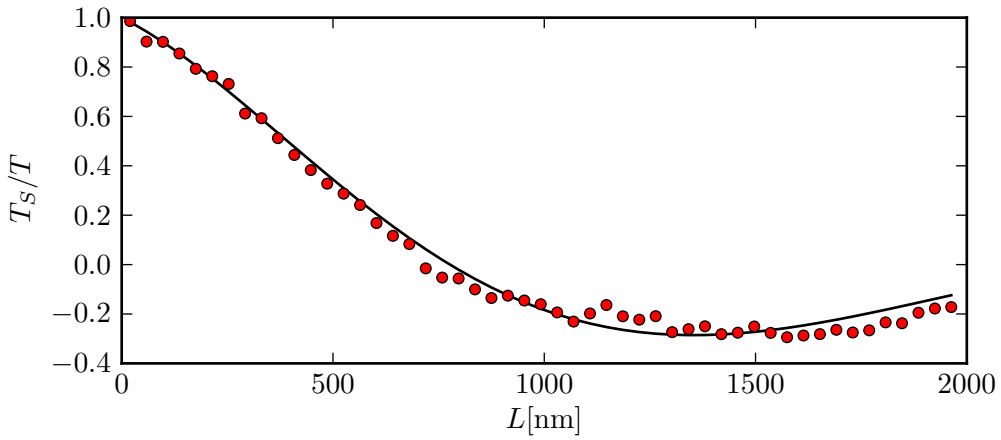

Figure 6.2.: Normalized spin transmission T_{Sz}/T as a function of system length L. Solid line is a fit to an exponentially damped cosine, and red dots show the numerically calculated spin transmission. Calculations have been performed for an adatom concentration of 7%, which induces a local Rashba spin-orbit coupling with a strength of 8meV.

potential and spin-orbit disorder. We chose showcase parameters to render the characteristics visible. The form is an exponentially damped cosine as we have obtained before from the calculations for the Dyakonov-Perel mechanism. Note that the cosine shape of the spin transmission hints at two things. First, a notable spin precession is present in the system indicating Dyakonov-Perel spin relaxation. Second, the average spin-orbit coupling is finite which is an artifact of the numerical procedure assigning local spin-orbit coupling moments to the individual impurities.

We first verify the Sherman spin relaxation rate. For ballistic transport the spin relaxation length is directly proportional to the spin relaxation time,

$$L_S^{\text{ballistic}} = v_F \tau_S = \frac{\sqrt{3}}{16\pi^2} \frac{(ta)^3}{\xi_{\text{Ad}}^4 \lambda_{\text{Ad}}^2 \rho_{\text{Ad}} E_F}, \tag{6.10}$$

using the quantum mechanical extrapolation of the Sherman spin relaxation rate, Eq. (6.8). For typical parameters, $\xi_{\text{Ad}} = a$, $\lambda_{\text{Ad}} = 0.002t$, $E_F = 0.1t$, the spin relaxation length at $\rho_{\text{Ad}} = 0.002/a^2 \approx 10^{12}/\text{cm}^2$ is approximately 1mm. If transport is diffusive, i. e. $L_S \gg l_{tr}$, the spin relaxation is proportional to the square root of the spin relaxation time τ_S and we get

$$L_S^{\text{diffusive}} = \sqrt{D\tau_S} = \sqrt{\frac{l_{tr}}{2}} \sqrt{L_S^{\text{ballistic}}} = \sqrt{\frac{l_{tr}}{2}} \sqrt{\frac{\sqrt{3}}{16\pi^2} \frac{(ta)^3}{\xi_{\text{Ad}}^4 \lambda_{\text{Ad}}^2 \rho_{\text{Ad}} E_F}}. \tag{6.11}$$

The spin relaxation length with the aforementioned parameters at a mean-free path of $\mathcal{O}(10^2\text{nm})$ is of the order of 1μm.[1] We varied the mean free path by changing the disorder parameters. In Fig. 6.3 we plot how for these cases the spin relaxation length depends on $\rho_{\text{Ad}}\xi_{\text{Ad}}^4$. We can identify the ballistic regime where $L_S \propto 1/(\xi_{\text{Ad}}^4 \rho_{\text{Ad}})$. The ballistic formula also applies for weakly disordered systems, in the quasi-ballistic regime where the mean-free path is comparable to the system size. By increasing disorder both mean-free path and spin relaxation length get reduced and we can identify a diffusive regime of spin relaxation where $L_S \propto \sqrt{1/(\xi_{\text{Ad}}^4 \rho_{\text{Ad}})}$. Notably we obtain spin relaxation lengths larger than the analytical estimate by a factor of 10.

Numerical calculations also confirm the relation between the spin relaxation and the induced Rashba spin-orbit coupling, $\lambda_{\text{BR}}^{\text{Ad}}$; see Fig. 6.4.

Which other signatures does the adatom-assisted Sherman mechanism show? The numerical calculation of spin transport for a large number of graphene samples at different parameters reveals how obstructive the classification in terms of EY or DP spin relaxation can be. We find that spin relaxation length is not independent of the mean-free path. Equation (6.11) suggests a square root dependence between the mean-free path and the spin relaxation length. We find a power law behavior lying between the linear relation from EY mechanism and the square root dependence. We plotted the effective parameters l_{tr}, and L_S in Fig. 6.5. Evaluating the spin-flip ratio Γ_{sf} as a function of the momentum scattering rate τ_p^{-1}, Fig. 6.6, hints at a linear relation. However, these statements are rather tentative due to the uncertainty of

[1] $\rho_{\text{Ad}} = 0.002/a^2$ is a rather large density for spin-orbit impurities if we assume them to be adsorbed adatoms. Densities lower by 2 to 3 orders of magnitude are expected if adatoms are not deposited artificially.

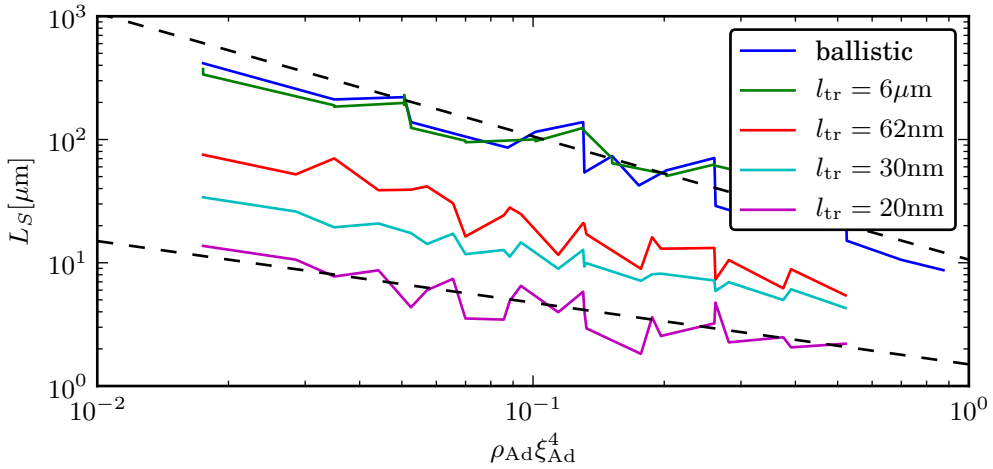

Figure 6.3.: Dependence of spin relaxation length on "Sherman parameter" for ballistic and diffusive systems. Dashed lines indicate the ballistic expectation value, $L_S \propto \xi_{\mathrm{Ad}}^{-4}\rho_{\mathrm{Ad}}^{-1}$, and the diffusive expectation value $L_S \propto \xi_{\mathrm{Ad}}^{-2}\rho_{\mathrm{Ad}}^{-1/2}$.

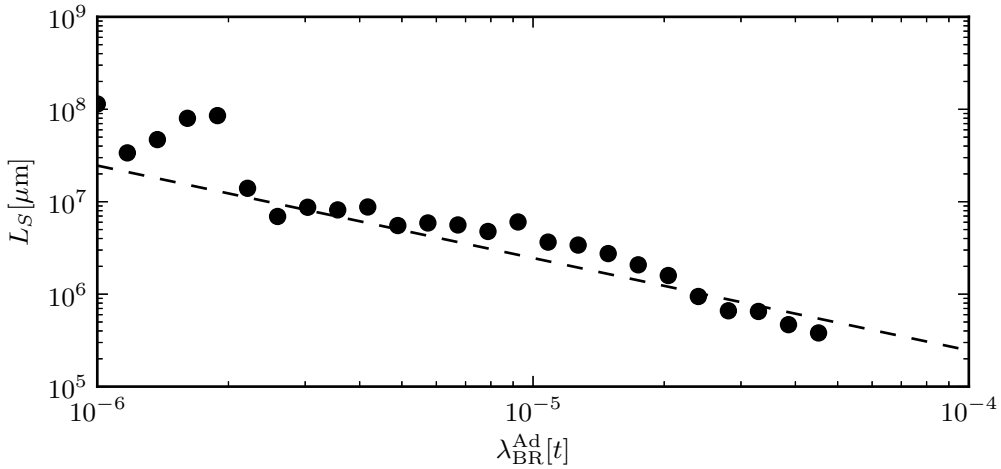

Figure 6.4.: Spin relaxation length as a function of increased Rashba coupling $\lambda_{\mathrm{BR}}^{\mathrm{Ad}}$ for diffusive systems; the dashed line is proportional to $1/\lambda_{\mathrm{BR}}^{\mathrm{Ad}}$.

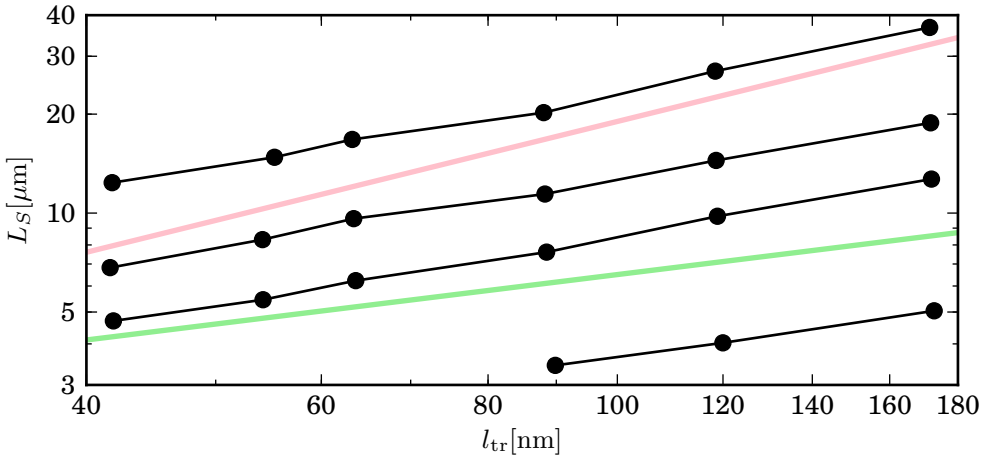

Figure 6.5.: L_S as a function of l_{tr}. Spin relaxation is induced by adatoms which create a random SOC. They are not connected linearly (pink line) like in EY spin relaxation. Still spin scattering increases when momentum scattering gets stronger. From the theory of the Sherman spin relaxation, a square root dependence would rather be expected (green line).

the numerical calculations. In any case, there is a clear influence of the mean free path on spin relaxation length which would not be expected from Dyakonov-Perel spin relaxation, and in the simple classification scheme the EY mechanism would be favored without knowing the microscopic details.

It turned out that the inclusion of intrinsic spin-orbit coupling from the adatoms has a distinct influence on in-plane and out-of-plane polarized spins. We plot how the spin flip ratio Γ_{sf} evolves as a function of $\Delta_{\mathrm{SO}}^{\mathrm{Ad}}/\lambda_{\mathrm{BR}}^{\mathrm{Ad}}$ in Fig. 6.7 and discover a large resemblance with the anisotropy of the Elliot-Yafet spin relaxation, Fig. 5.4. A negligible change of the spin flip ratio with increasing $\Delta_{\mathrm{SO}}^{\mathrm{Ad}}$ for out-of-plane polarized spin is contrasted by a significant increase of Γ_{sf} for in-plane polarized spins.

We want to emphasize that spin relaxation lengths are obtained from calculations at high concentrations of sites with increased spin-orbit coupling. Otherwise spin relaxation is very weak and our systems are too short to fit the exponential decay of the spin transmission at sufficiently high accuracy. In those cases we considered the spin-flip ratio $\Gamma_{\mathrm{sf}} = T_{\mathrm{sf}}/T_{\mathrm{sc}}$, the ratio between spin-flip and spin-conserving transmission probabilities. Notably, the systems we considered are 2μm long. Consequently, as spin decay at this length is rather weak, spin relaxation lengths in our simulated systems is clearly larger than reported spin relaxation lengths.

6.4. Discussion and Summary

Both spin precession and spin-flip scattering seem to be involved in the spin relaxation from fluctuating spin-orbit fields. While the relations between the different involved physical parameters pretend that the Elliot-Yafet mechanism is the dominant spin

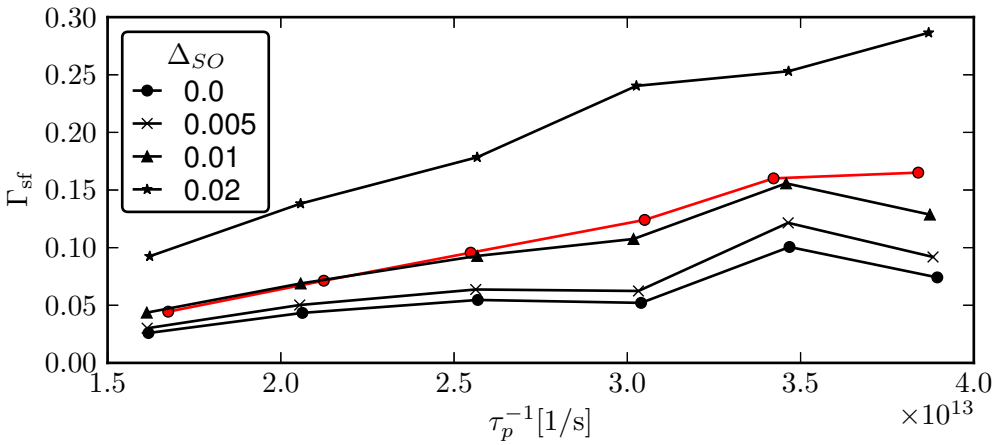

Figure 6.6.: The spin flip ratio $\Gamma_{\rm sf} = T_{\downarrow\uparrow}/T_{\uparrow\uparrow}$ as a function of the system's mean free path. Parameters are $\rho_{\rm Ad} = 0.001$, $\lambda_{\rm Ad} = 0.01t$, and values for $\Delta_{\rm SO}^{\rm Ad}$ are given in the legend. We plotted out-of-plane (red curve) and in-plane spin relaxation (black curves). The out-of-plane spin flip ratio is not affected by $\Delta_{\rm SO}^{\rm Ad}$.

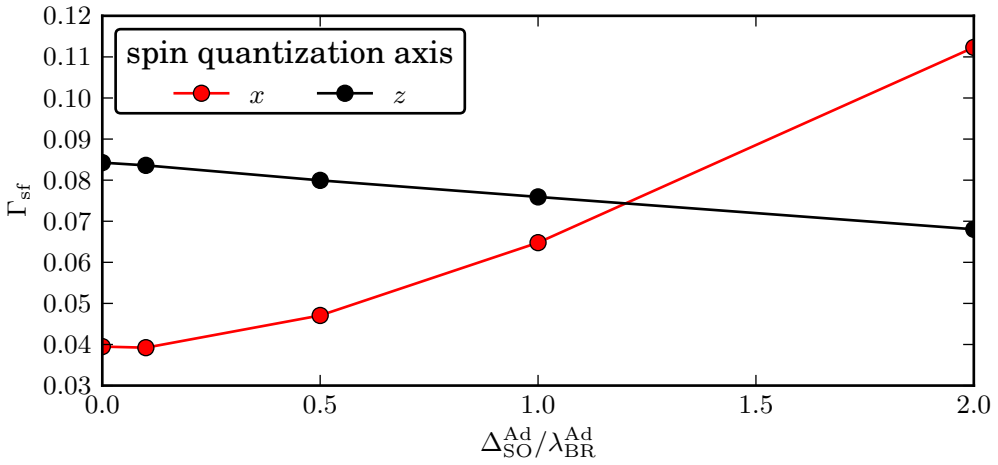

Figure 6.7.: Spin relaxation length as a function of $\Delta_{\rm SO}^{\rm Ad}$ at $\rho_{\rm Ad} = 0.001$, $\lambda_{\rm BR}^{\rm Ad} = 0.01t$, $E_F = 0.11t$. The anisotropy of L_S can be controlled by varying the intrinsic spin-orbit coupling induced by the adatoms.

relaxation mechanism in graphene, the oscillatory spin transmission is an indication for Dyakonov-Perel spin relaxation.

Besides this conceptional investigation of the spin relaxation due to random fluctuations of the spin-orbit coupling we draw also general conclusions on the potential of explaining the high spin relaxation rate found in experiments. In all the presented data spin relaxation lengths are several orders above the experimentally found $\mathcal{O}(1\mu\text{m})$. We can choose parameters to reproduce this high spin relaxation rate. Therefore local peak heights of Bychkov-Rashba spin-orbit coupling $\lambda_{\text{BR}}^{\text{Ad}} = 0.003t = 7.8\text{meV}$ at adatom densities $\rho_{\text{Ad}} \geq 0.01$ would be required.

We know from section 5.2 that a single impurity with similar parameters leads to a spin-flip probability of 10^{-6}. Neglecting correlations between impurities this spin-flip probability is simply multiplied by the number of scattering centers to obtain the spin flip ratio. So, the total number of impurities should be $\mathcal{O}(10^5)$ to achieve sufficiently large spin relaxation. This is the case for $\rho_{\text{Ad}} \geq 0.01$. Zhang and Wu proposed an interplay between Dyakonov-Perel spin relaxation and spin-flip from a random Rashba field [39]. In our numerical calculations Dyakonov-Perel spin relaxation is of minor importance. With a decay length of $1.1a$ for the spin-orbit coupling and a Fermi velocity of 10^6m/s an electron spends $\tau_D \approx 1$ femtosecond in the zone around an adatom. Assuming an average spin splitting of $\mathcal{O}(1\text{meV})$ implies spin precession times τ_{Larmor} between 100fs and 1ps. From that it follows that $\tau_D \ll \tau_{\text{Larmor}}$ and, hence, motional narrowing suppresses spin relaxation according to the Dyakonov-Perel mechanism. The oscillatory part of the spin transmission has to be attributed to a residual finite average spin-orbit coupling. Hence, spin-flip scattering from the spin-orbit disorder is dominating over Dyakonov-Perel like spin relaxation.

In summary, while studying the effective modeling of adatoms in graphene gives interesting insights into spin transport physics in graphene, this model seems inadequate to describe the real situation encountered in experiments. This judgment is mainly justified by the large discrepancy of the numerically calculated and the experimentally measured spin relaxation times. The adatom densities required to achieve sufficiently large spin relaxation rates were too large. We, however, do not refuse the potential of adatoms to be a possible source of the high spin relaxation rate in graphene and want to stress that no coincidence between experiment and theory can be achieved within this model. In the next chapter we present a more realistic way of modeling adatoms in graphene. That model will allow for a resonant state forming in the vicinity of the adatom enhancing both the lifetime of the electron near the adatom as well as the spin flip rate by a single impurity.

7. Atomistic description of adsorbed adatoms

The previous chapters were dedicated to the investigation of spin relaxation in graphene by spin-orbit coupling (SOC) which possibly exhibits fluctuations in position space. While we obtained a deep insight into the physics of spin relaxation by SOC in graphene we were not able to explain the relatively spin relaxation rates found in the experiments. Neither the well-established mechanisms, like the Dyakonov-Perel and the Elliot-Yafet mechanism due to background SOC nor the spin-orbit disorder attributed to adsorbed adatoms (Sherman mechanism) gave sufficiently high rates for parameters expected to occur in real experimental setups. The model used in the last chapter, however, did not include resonance effects. To this end we implemented an extended tight-binding model for graphene in the presence of adsorbates, which has been developed in Refs. [95, 42, 43, 33].

Similar to the model used in chapter 6 the adsorption of adatoms to the graphene surface results in strongly increased spin-orbit interaction for both hydrogen and fluorine adatoms. For hydrogenated graphene, an additional formation of local magnetic moments is predicted [33].

We will use the presented model to perform transport calculations and to quantify the resulting spin relaxation. The role of resonant states as well as comparison between SOC and local magnetic moments will be discussed.

7.1. Tight-binding model for adsorbates

We model adatoms as a single-level system with an on-site energy $\varepsilon_{\mathrm{AD}}$ [95, 108]. This description is assuming adatoms to be located at *top positions*, i. e. directly above a carbon site. Other adsorption positions are the *bridge position*, where the adatom is sitting above the center of a carbon-carbon link, and the *hollow position*, where the adatom is located in the center of one hexagon.

In the tight-binding description we include additional vertices representing the adatom sites. Adatoms and their nearest-neighbor carbon sites are coupled through a kinetic hopping element of strength T.

$$\mathcal{H} = \mathcal{H}_0 + \varepsilon_{\mathrm{AD}} \sum_m h_m^\dagger h_m + T \sum_{\langle m,i \rangle} (h_m^\dagger c_i + \mathrm{H.c.}). \tag{7.1}$$

Additionally, in the vicinity of the adatom the Bychkov-Rashba SOC

$$\mathcal{H}_{\mathrm{AD,\,BR}} = \frac{2\mathrm{i}\Lambda_{\mathrm{BR}}}{3} \sum_{\langle C_{\mathrm{Ad}},j \rangle} \left\{ A_\sigma^\dagger [(\boldsymbol{d}_{C_{\mathrm{Ad}},j} \times s) \cdot \hat{z}]_{\sigma\sigma'} B_{j,\sigma'} + \mathrm{H.c.} \right\}, \tag{7.2}$$

and the intrinsic SOC

$$\begin{aligned}\mathcal{H}_{\mathrm{AD,\,I}} =& \frac{\mathrm{i}\Lambda_I^A}{3\sqrt{3}} \sum_{\langle\langle C_{\mathrm{Ad}},j\rangle\rangle} v_{C_{\mathrm{Ad}}j}[A_\sigma^\dagger (s_z)_{\sigma\sigma'} c_{j,\sigma'} + \mathrm{H.c.}] + \\ &+ \frac{\mathrm{i}\Lambda_I^B}{3\sqrt{3}} \sum_{\langle\langle B_i,B_j\rangle\rangle} v_{B_iB_j}[B_\sigma^\dagger (s_z)_{\sigma\sigma'} B_{j,\sigma'} + \mathrm{H.c.}],\end{aligned} \tag{7.3}$$

appear [95]. Sums are running over functionalized carbon adatoms, C_{Ad}, located below the adsorbed adatoms or their nearest-neighbors, B_i, and their respective nearest-neighbors $\langle\cdot\rangle$ or next-nearest-neighbors $\langle\langle\cdot\rangle\rangle$. Moreover, we rewrite creation and annihilation operators on the functionalied carbon sites as $A_i^{(\dagger)}$ and on their nearest-neighbors as $B_i^{(\dagger)}$ for better readability and to emphasize their modified role. Local strength of SOC is given by $\Lambda_{\mathrm{BR}}/\Lambda_I^{A/B}$. Apart from that differing coupling strength, they correspond to the formerly used intrinsic and Rashba SOC.

An adatom at the *top position* breaks the sublattice symmetry giving rise to a further spin-orbit coupling term

$$\begin{aligned}\mathcal{H}_{AD,PIA} =& \frac{2\mathrm{i}\Lambda_{\mathrm{PIA}}^A}{3} \sum_{\langle\langle C_{\mathrm{Ad}},j\rangle\rangle} \left\{ A_\sigma^\dagger [(\boldsymbol{d}_{C_{\mathrm{Ad}},j} \times s)\cdot\hat{z}]_{\sigma\sigma'} c_{j,\sigma'} + \mathrm{H.c.} \right\} + \\ &+ \frac{2\mathrm{i}\Lambda_{\mathrm{PIA}}^B}{3} \sum_{\langle\langle B_i,B_j\rangle\rangle} \left\{ B_\sigma^\dagger [(\boldsymbol{d}_{i,j} \times s)\cdot\hat{z}]_{\sigma\sigma'} B_{j,\sigma'} + \mathrm{H.c.} \right\},\end{aligned} \tag{7.4}$$

which acts on the same next-nearest-neighbor links as the increased intrinsic SOC (7.3).[1] No term similar to the latter one has been included in the previous chapters of this thesis. In other *honeycomb materials* like silicene and two-dimensional germanium and tin a similar SOC has to be considered due to the buckled lattice structure with the two sublattices shifted oppositely along the z-axis. There it is commonly labeled *intrinsic Rashba coupling* [109]. We can approximate the PIA SOC in the effective low-energy Hamiltonian by

$$\mathcal{D}_{\mathrm{PIA}} = \frac{a}{2}\Lambda_{\mathrm{PIA}}(k_x s_y - k_y s_x), \tag{7.5}$$

which resembles the Rashba SOC obtained for 2DEGs. Here a is the lattice constant, $k_{x/y}$ are momentum operators. The effective magnetic field created from the PIA SOC is lying in the x-y plane. It is perpendicular to the momentum as for Rashba SOC. In contrast, spin splitting is proportional to the momentum instead of being constant. We will later show its outstanding role in SOC mediated spin relaxation.

[1] The strength parameter is conventionally labeled as Λ_{PIA} originating from Pseudospin Inversion Asymmetry.

	Hydrogen	Fluorine
$\varepsilon_{\mathrm{AD}}$	$0.062t \approx 0.16\mathrm{eV}$	$-1.27t \approx -3.3\mathrm{eV}$
T	$2.885t \approx 7.56\mathrm{eV}$	$2.3t \approx 5.98\mathrm{eV}$
Λ_{BR}	$1.27 \cdot 10^{-4}t \approx 0.33\mathrm{meV}$	$0.00435t \approx 11.3\mathrm{meV}$
Δ^A_{SO}	$-8.1 \cdot 10^{-5}t \approx -0.21\mathrm{meV}$	$0t = 0\mathrm{eV}$
Δ^B_{SO}	$0t = 0\mathrm{eV}$	$0.0013t \approx 3.2\mathrm{meV}$
Λ^B_{PIA}	$-2.96 \cdot 10^{-4}t \approx -0.77\mathrm{meV}$	$-0.003t \approx -7.9\mathrm{meV}$

Table 7.1.: Tight-binding parameters for the effective description of graphene with adsorbed hydrogen or fluorine atoms. Parameters taken from Refs. [95, 33] for hydrogen and from Refs. [42, 43] for fluorine.

Locally also spin splitting can be induced [33],

$$\begin{aligned}\mathcal{H}_{\mathrm{AD,\ Zeeman}} = \sum_{m,\sigma} \Big[& h^\dagger_{m\sigma}(\boldsymbol{J}_H \cdot \boldsymbol{s})_{\sigma\sigma} h_{m\sigma} + \\ & + \sum_{i \in NN} B^\dagger_{i,\sigma}(\boldsymbol{J}_{1,m}\boldsymbol{s})_{\sigma\sigma} B_{i,\sigma} \\ & + \sum_{i \in NNN} c^\dagger_{i,\sigma}(\boldsymbol{J}_{2,m}\boldsymbol{s})_{\sigma\sigma} c_{i,\sigma} \Big] .\end{aligned} \tag{7.6}$$

The outer sum is running over the adatom sites m and the spin splitting is given by $|\boldsymbol{J}_H|$. No splitting is expected on the carbon under the adatom, but we expect spin splittings of size $|\boldsymbol{J}_1|$ on their nearest-neighbors, NN, and $|\boldsymbol{J}_2|$ on their next-nearest-neighbors, NNN. Magnetic moments around one adatom are parallel, $\boldsymbol{J}_H \parallel \boldsymbol{J}_1 \parallel \boldsymbol{J}_2$, but they can have opposite signs. For different adatoms the magnetic moments need not be parallel.

For fluorine adatoms a debate about the appearence of local magnetic moments is still ongoing. Experimentally indications of magnetization in fluorinated graphene have been found [110, 111, 112]. Density functional theory calculations disagree on this question and for different choices of functionals either favor magnetism in fluorinated graphene [113] or find it to be non-magnetic [114, 115, 116]. A final answer has not been given yet.

In the case of hydrogenated graphene there is a consensus about the existence of local magnetic moments [34, 33]. For the purpose of this work we rely on parameters obtained from DFT calculations in Refs. [95, 33] for hydrogen. Orbital parameters and SOC strengths are summarized in table 7.1. In hydrogenated graphene the expected magnetic moments are $J_H = -0.32t$, $J_1 = 0.27t$, and $J_2 = -0.07t$.

The parameters of fluorinated graphene are also listed in table 7.1 and are taken from Refs. [42, 43]. When referring to fluorinated graphene we assume the absence of local magnetic moments, $J_H = J_1 = J_2 = 0$. For testing purposes we also performed calculations in fluorinated graphene with magnetic moments. The parameters used in that case will be stated in the corresponding passage.

7.2. Density of states of fluorinated and hydrogenated graphene

We calculate the density of states (DOS) for hydrogenated and fluorinated graphene considering only the orbital contribution of the adatoms, neglecting the spin degree of freedom. To this end we set up a rectangular graphene supercell and add one single adatom. Opposite edges are connected by a complex valued hopping $t \cdot \mathrm{e}^{\mathrm{i}\Phi_{x/y}}$ according to Bloch's theorem. For each pair of Bloch phases $\Phi_x, \Phi_y \in [0, 2\pi[$ we can calculate the Hamiltonian's eigenenergies. Eventually for a fine grid in $\Phi_x - \Phi_y$ space the eigenenergy distribution converges against the density of states.

We calculated the DOS for supercells of different sizes corresponding to different adatom densities. The data shown in Fig. 7.1 was calculated for a supercell which consists of approximately 1000 carbon atoms and 1 adatom. While the linear DOS of graphene is already dominant we see particular clear deviations for both the hydrogenated and the fluorinated case.

For hydrogenated graphene, the most drastic influence is the opening of a gap in the spectrum with a very pronounced peak within the gap for the impurity state which resides on and close to the adatom. The peak width is of the order $\mathcal{O}(0.001t) \approx \mathcal{O}(1\mathrm{meV})$. From the DOS we expect a strong influence on charge transport and assume a strongly reduced transmission as hydrogenated graphene becomes isolating in the adatom's vicinity signalized by the opening of a gap.

The DOS of fluorinated graphene for energies above the charge neutrality point coincides with the linear DOS of pristine graphene, it deviates for energies smaller than zero. A pronounced peak like for hydrogenated graphene is not visible. Moreover, there is no gap opening, but we can roughly identify the impurity state which is spread over a large energy range by strong deviations from the DOS of pristine graphene.

So, we can predict already from the DOS the presence of strong momentum scattering in functionalized graphene. The energy range where this enhanced scattering is relevant differs for the considered elements.

We also calculated the local density of states (LDOS) near the adsorbates making use of Eq. (2.5). For both types of considered adatoms we assert that the LDOS is not symmetric with respect to energy; see Fig. 7.2 for comparison. The LDOS is significantly smaller on the covered carbon atom than on its nearest-neighbors and on the adatom itself. This difference is, however, much more pronounced for hydrogenated than for fluorinated graphene.

When comparing DOS and LDOS of hydrogenated graphene we notice an influence of the adatom in a wider energy range with two separate maxima. This is caused by the leads' level broadening reflecting the reduced lifetime of the states. In our calculations leads exhibit an armchair edge which is known to induce both level shift and level broadening [117]. The narrow peak of the DOS of hydrogenated graphene allows for this observation. The DOS of fluorinated graphene shows to much noise to determine a unique position and width of the impurity state, which in turn prevents a detailed comparison with the LDOS.

The broken sublattice symmetry in functionalized graphene was already mentioned in the last section when presenting the spin-dependent terms arising in the vicinity of

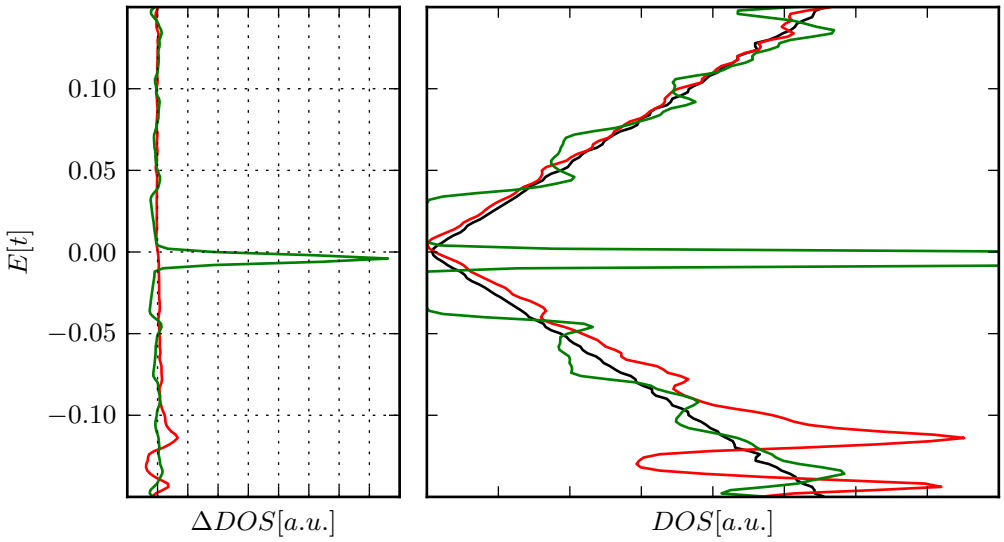

Figure 7.1.: Density of states for hydrogenated (green) and fluorinated (red) graphene at an adatom density of 10^{-3} compared with the DOS of pristine graphene (black). The difference of the DOS of hydrogenated and fluorinated graphene with respect to the DOS of pristine graphene is plotted in the left panel.

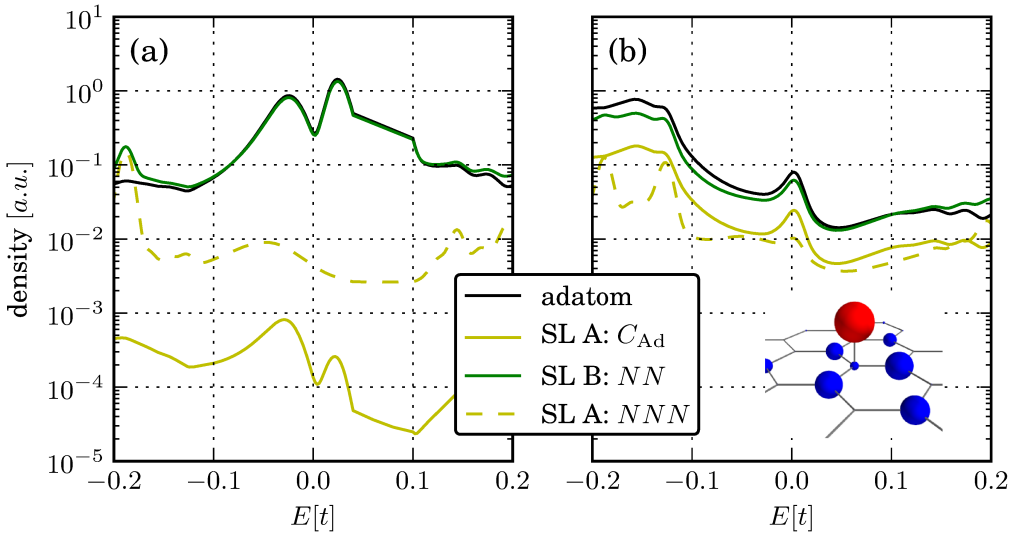

Figure 7.2.: Local density of states at different points in the lattice for (a) hydrogenated and (b) fluorinated graphene: the adatom, the functionalized carbon site (C_{Ad}), its nearest-neighbors (NN), and its next-to-nearest-neighbors (NNN).

the adatom. The LDOS confirms this property. In Fig. 7.2 the pseudospin inversion assymetry is reflected in the difference between yellow and green lines.

Both SOC and magnetization are of minor impact on the local density of states. However, they are important for spin transport as will be substantiated in sections 7.4 and 7.5.

7.3. Adatoms and charge transport

To investigate charge transport we calculate the momentum scattering probability of a single impurity. To this end, we consider a scattering region with a width of $65a \approx 16$nm containing one adatom and impose periodic boundary conditions along the transverse direction. For this system we calculate the momentum scattering probability

$$T_p = N - \sum_{i,\sigma} |t_{ii,\sigma\sigma}|^2, \tag{7.7}$$

which is the sum of all scattering probabilities except for the diagonal transmission probabilities, i. e. the non-scattered trajectories, subtracted from the total number of open channels, N. It is the equivalent to the scattering probability obtained from analytical calculations in the Born approximation.

Momentum scattering shows a non-monotonic dependence on the Fermi energy (see Fig. 7.3). It is most effective close to the resonance energies that we already obtained from the density of states. For hydrogenated graphene reaches values up to 0.7. Note that the peak width in the transmission curve of hydrogenated graphene, Fig. 7.3, covers a larger energy range than the peak in the density of states of comparable systems. We attribute this to level broadening which is caused by the leads. The same broadening has been seen in the local density of states. The equivalence to massless Dirac fermions results in forbidden backscattering for electrons in graphene [72]. We saw a manifestation of this property in the Klein tunneling studied in section 3.3. Adatoms can enable backscattering as we see from diffusive transport for systems with both a Gaussian background disorder, Eq. (5.2), and a random distribution of adatoms. It becomes evident for transport close to charge neutrality, where there is only one propagating channel per valley and spin which cannot be reflected in the absence of adatoms.

In Fig. 7.4 we plotted the mean-free path of hydrogenated graphene as a function of energy for different adatom concentrations. The mean-free path for systems without adatoms is 4 orders larger than the system length. Formally we would interpret this as a signature for ballistic systems but it is merely an indication of the forbidden backscattering which in that case doesn't allow to extract the momentum scattering length from the total transmission. We have to assume diffusive transport in the sense that there exists a momentum scattering length short compared to the system size. Regardless, there is no decay of the transmission, $T \propto 1/L$, as we have seen in the multi-channel calculations.

Only in the presence of adatoms the mean free path gets reduced either by inducing inter-valley scattering and/or by breaking chirality (see again Fig. 7.4). We assume

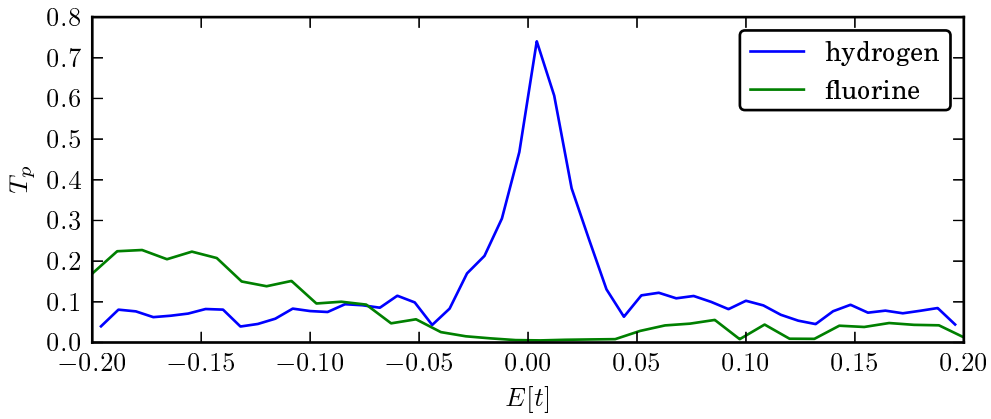

Figure 7.3.: Momentum scattering rate of a single adatom. We plot the values for a hydrogen adatom (blue line) and a fluorine adatom (green line).

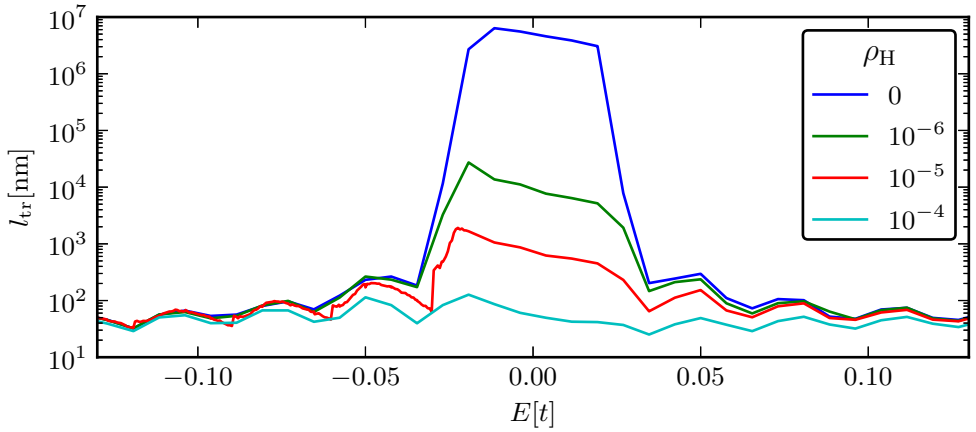

Figure 7.4.: Mean free path l_{tr} as a function of energy E at different concentrations ρ_H of hydrogen adatoms. The width of the graphene supercell is $180a \approx 45$nm. We can identify the single-mode region where backscattering is forbidden. The mean free path decreases linearly with the adatom concentration. In the multi-channel regime, on the other hand, adatoms do not influence the mean free path.

both effects to be involved as apparently chirality, i. e. the strong coupling between momentum and pseudospin, is broken by adatoms that break the sublattice symmetry. On the other hand it is known that point-like defects introduce scattering between the valleys in graphene. This finding holds for both hydrogen and fluorine adatoms.

7.4. Spin relaxation in random spin-orbit fields

We now turn our interest to spin transport by investigating the spin-flip potential of the SOC induced by the adatoms. This is done in three steps. The first step is the scattering from a single adatom similar to the model used for the investigation of the Elliot-Yafet mechanism. We extend our investigations by considering many adatoms scattered randomly over the scattering region. In a third step we consider additional scattering by the well-known Gaussian disorder, Eq. (5.2) and extract spin lifetimes following the procedure demonstrated already before by fitting predicted decay functions, Eqs. (5.8) and (5.9), to the (spin) transmission of systems with different lengths.

7.4.1. Spin-dependent scattering from a single adatom

For the system used to obtain the momentum scattering probability T_p, Eq. (7.7), we additionally calculate the spin scattering rate

$$T_{\mathrm{sf}} = \sum_{i,j;\sigma} |t_{ij,\sigma(-\sigma)}|^2. \tag{7.8}$$

The spin-flip ratio T_{sf}/T_p is considered to be proportional to the Fermi's Golden Rule scattering rates' ratio τ_S^{-1}/τ_p^{-1}. This calculation is performed for both hydrogen and fluorine, but instead of working with the bare parameters obtained from DFT calculations, we reduce the strengths of the SOC terms simultaneously by a factor $\chi_{SOC} \in [0.001, 1]$.

The spin-flip ratio, T_{sf}/T_p, of both a hydrogen or a fluorine adatom shows only weak dependence on Fermi energy. Its dependence on χ_{SOC} is quadratic and we find

$$T_{\mathrm{sf}}/T_p = \begin{cases} 2 \times 10^{-6} \chi_{SOC}^2 & \text{fluorine,} \\ 8 \times 10^{-8} \chi_{SOC}^2 & \text{hydrogen,} \end{cases} \tag{7.9}$$

for in-plane polarized spins. The spin-flip ratio is twice as large for out-of-plane polarized spins. We know that the same anisotropy ratio was also obtained for the Elliot-Yafet spin relaxation in pure Rashba systems. A suppression of the influence of the increased intrinsic SOC can, hence, be assumed, which we will analyze in more detail in the next section. Notably, the spin-flip rates for both considered adatoms are not significantly larger than for the formerly used model of spin-orbit disorder.

7.4.2. Spin-dependent scattering from a cluster of adatoms

We increase the system size to study the effect of many adatoms distributed randomly over the scattering region. The considered systems are $70a$ wide and $1000a$ long. We

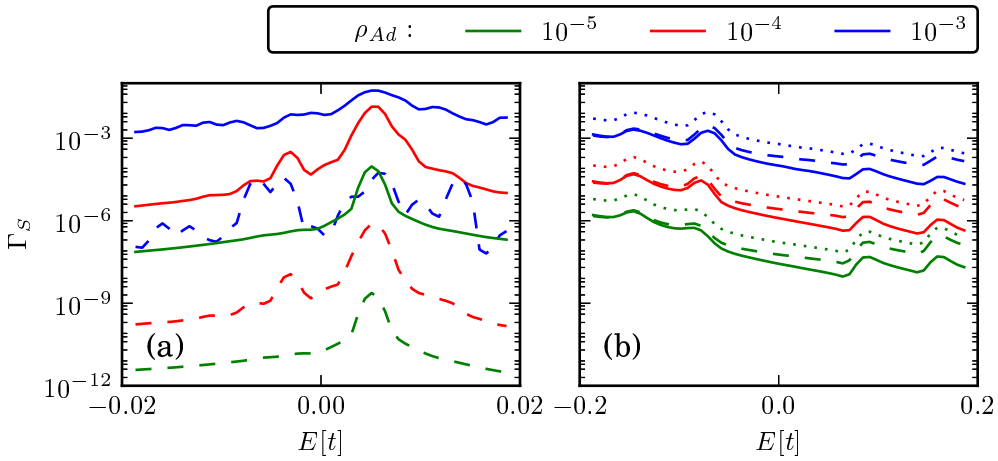

Figure 7.5.: Spin-flip probability Γ_S of (a) hydrogenated and (b) fluorinated graphene as a function of Fermi energy. Adatom densities ρ_{Ad} vary between 10^{-5} and 10^{-3}.

calculate total transmission T, Eq. (5.8), and spin transmission $T_{s\mu}$, Eq. (5.9). No other sources of scattering than the adatoms are present in the system. Again we impose periodic boundary conditions.

The calculations of the spin-flip probability $\Gamma_S = T_{\mathrm{sf}}/T = 1 - T_{S,z}$ reveals the importance of the newly introduced PIA SOC. In Fig. 7.5 we present calculations on spin transport. Therein, solid lines represent the full tight-binding model. We also modified the strengths of the different types of SOC but not simultaneously as in the single adatom limit. For instance, a dotted line stands for adatoms only inducing PIA SOC, while dashed lines stand for systems where there is no PIA contribution at all. In hydrogenated graphene, ignoring the PIA contribution leads to a decreased spin-flip probability by more than 3 orders of magnitude. In fluorinated graphene the difference is not so crucial, but still the PIA SOC alone is the most effective term for spin-flip in the whole energy range. The calculations show a more pronounced dependence on Fermi energy as the ones for single adatoms reflected the DOS.

To understand the importance of the different SOC terms involves a comparison with the local density of states. Let us first have a look at the Rashba SOC. It leads to a spin flip probability proportional to $|\Lambda_{\mathrm{BR}}\langle B\downarrow|s_{x/y}|A\uparrow\rangle|^2$, where $|A\uparrow\rangle$ is the amplitude of the wavefunction on the covered atom, spin-up component, and $|B\downarrow\rangle$ is the spin-down component of the wavefunction on one of its nearest-neighbors. Both Λ_{BR}^2 and the matrix element $|\langle B\downarrow|s_{x/y}|A\uparrow\rangle|^2$ influence the size of the spin-flip probability. But we already showed that the local density of states $\langle A\uparrow|A\uparrow\rangle$ is suppressed and, for hydrogen, several orders of magnitude smaller than the density of states on other carbon sites. This makes the increased Rashba SOC inefficient for spin relaxation. A similar argument can be given for the intrinsic SOC. On the other hand the PIA SOC involves only nearest-neighbors of the covered atoms. Since these lead to a large spin-coupling matrix element $|\langle B_i\downarrow|s_{x/y}|B_j\uparrow\rangle|^2$, compared to the other SOC terms, spin-flip capability of the PIA term is rather large. Notably, the differences of

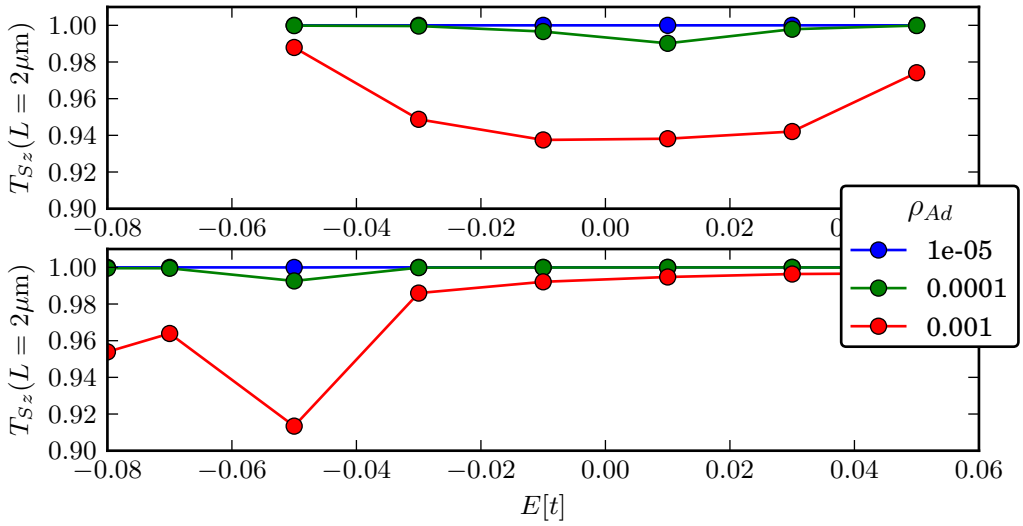

Figure 7.6.: Spin polarization as extracted from (a) hydrogenated and (b) fluorinated graphene. Because the exponential decay of T_{Sz} is too slow to effectively extract the spin relaxation length we directly plot the final spin transmission.

wavefunction amplitudes on the involved carbon sites is more pronounced for hydrogen adatoms than for fluorine.

A remarkable property of hydrogen adatoms is their potential in momentum relaxation. Close to charge neutrality, even low concentrations of adatoms ($\rho_H \geq 10^{-5}$) reduce transmission to $T < 1/2$ which is in line with the results obtained in the single adatom limit. Densities of $\rho_H \gtrsim 10^{-3}$ open a gap in the dispersion and turn graphene into an insulator. Strong backscattering can also be obtained in fluorinated graphene. It has, however, to be figured out if the energy range where fluorine adatoms lead to strong momentum relaxation, is experimentally accessible.

7.4.3. Adatoms in diffusive graphene

While so far momentum relaxation has been induced by the local potentials from the presence of adatoms we now include an additional background potential disorder V_{dis} according to equation (5.2). We calculate transmission as a function of system length and can use the results to obtain the mean free path l_{tr}. Independent of the mean free path spin relaxation was weak in our systems. In fact a reliable extraction of the spin relaxation length, L_S, was not feasible because the weak decay of the spin relaxation led to large residuals in fitting the results to an exponential. Instead we plot in Fig. 7.6 the normalized spin transmission for $L = 2\mu$m. T_{Sz} is mostly significantly larger than 0.9. A stronger decrease of the spin transmission can be observed close to the resonance energies at high adatom concentrations. Note that hydrogenated graphene becomes insulating at these large adatom concentrations. Moreover, the drop of the spin polarization can be mainly ascribed to precession in the residual average spin-

orbit field. Spin relaxation in the sense of a randomization happens on even longer lengthscales.

These results and the ones obtained from the effective model, investigated in the previous chapter, are not able to explain the spin relaxation rates in graphene. Rather, we can safely assume that spin relaxation due to SOC is of little importance in most experiments. In both models, adatom densities of $\rho_{\mathrm{Ad}} > 0.01$ are required for a significant spin relaxation. Such densities can be obtained artificially [111] but for most systems we can rule out the importance of spin relaxation due to spin-orbit disorder since such large adatom densities would have been noticed in Raman spectra or by scanning tunneling microscopy.

On the other hand we want to stress that the atomistic model features a complex, non-monotonic dependence of spin transport on energy mainly determined by the orbital part of the Hamiltonian which cannot be obtained from the effective model.

As SOC in no model considered so far in this work and in literature is suitable for explaining the high spin relaxation rate we continue by including the formation of magnetic moments in the next section.

7.5. Magnetic moment formation

Bare graphene is a non-magnetic material. It can, however, become magnetic under certain circumstances. A prominent source of magnetism is the presence of zigzag edges which will be a topic of this work (see Part II of this thesis and Ref. [118]). Adatoms are a further source of magnetism as we already announced in section 7.1. A comprehensive review of magnetism in graphene can be found in Ref. [34].

Similar to the previous chapter we investigate spin transport in the presence of adatom-induced magnetism in two steps. We begin with the investigation of the spin-flip ratio of a single adatom. Data relevant for experimentalists is then extracted from calculations of diffusive graphene systems.

7.5.1. Single adatom limit

We use the same systems as for the investigation of SOC induced spin relaxation in the single adatom limit. Now, we neglect SOC terms but set the magnetic moments to finite values: $J_H = -\chi_J 0.32t$, $J_1 = \chi_J 0.27t$, and $J_2 = -\chi_J 0.07t$, where the scaling factor χ_J is used to simultaneously rescale the magnetic moments as we did before with χ_{SOC}. The spin flip-ratio T_{sf}/T_p is calculated as a function of both χ_J and E. We summarize the results in Figs. 7.7 and 7.8. For small values of $\chi_J \ll 1$ as well as for energies away from the resonance energy the spin flip ratio scales quadratic in χ_J. At resonance we see a saturation of the spin-flip ratio. Its functional form is [33]

$$T_{\mathrm{sf}}/T_p = \Gamma_{\mathrm{sat}} \frac{\chi_J^2}{\chi_J^2 + \chi_0^2}. \tag{7.10}$$

The curve is determined by the saturation value Γ_{sat} and by χ_0 which defines a threshold value. At this threshold spin rotation becomes fast enough to change the spin orientation significantly during the lifetime of the impurity state. This lifetime is inversely proportional to the spread of the state in energy space.

Fitting our numerical results to Eq. (7.10) yields $\Gamma_{\text{sat}} = 0.58$ and $\chi_0 = 0.51$. For $\chi_J \ll \chi_0$ the spin flip ratio goes as $T_{\text{sf}}/T_p = 2.3\chi_J^2$ which is severals orders of magnitude larger than under the consideration of pure SOC, cf. Eq. (7.9).

We compare $\chi_0 J_H$ to the width of the peak in the momentum scattering rate (see Fig. 7.3) which is approximately $\Delta E_{\text{peak}} \approx 0.05t$. The peak width is smaller than the spin splitting at the hydrogen site $\Delta E_{\text{peak}} = 0.05t < 0.16t = |\chi_0 J_H|$. However, this comparison neglects the magnetic moments on other lattice sites than on the adatom. So we rather have to assume an effective reduced magnetization due to the opposite direction of the involved magnetic moments. To substantiate this argument and to make our results consistent, we repeated the calculation explicitly setting $J_1 = J_2 = 0$, keeping only J_H finite. We obtain $\Gamma_{\text{sat}} = 0.42$ and $\chi_0 = 0.2$ from this calculation where $|\chi_0 J_H| = 0.064t$ is only slightly larger than the resonance width. Similar perturbative calculation performed by Denis Kochan [33] using the bare width of the DOS peak obtain consistent results.

Magnetic moments located at the adatoms induce spin-flip ratios several orders of magnitude larger than SOC. At saturation the ratio reaches values of order 0.1. In combination with the high momentum relaxation rate found we expect a high efficiency in spin relaxation from magnetic adatoms. Hence, we now investigate spin transport in diffusive graphene with magnetic adatoms.

7.5.2. Resonant magnetic scatterers in diffusive graphene

In order to investigate spin relaxation from adatoms inducing magnetism in diffusive graphene we, again, revert to the combination of randomly distributed adatoms and the Gaussian background disorder, Eq. (5.2). Let us begin with the main result and reveal a simple, but strong statement. From our numerics, we see that hydrogen adatoms by their local magnetic moments lead to low spin relaxation times comparable to the ones found in the experiments – even at low adatom concentrations. Resonant magnetic scatterers are the strongest source of spin relaxation considered in this work, and also in literature no other scattering mechanism of comparable spin-flip capability has been presented. In the following we want to substantiate the importance of the facts that we are dealing with *magnetic* impurities and *resonant* scattering.

The importance of magnetic adatoms is already apparent from the single adatom limit when comparing the pure SOC case with the case of magnetic impurities. We showed that the spin-flip ratio in the latter case exceeds the non-magnetic impurity by several orders of magnitude. An argument to understand this difference is based on the different nature of spin splitting in the two cases. Spin precesses around a constant axis in the case of magnetization, i. e. a Zeeman term, the axis is changed simultaneously with the momentum in the case of spin orbit coupling. Thinking of the impurity state as a very small quantum dot the effective magnetic field of the SOC changes its direction within very short timescales and this rapid randomization decreases the efficiency of spin relaxation due to strong motional narrowing (see section 5.1). Spin precession in a constant magnetic field is not affected by motional narrowing.

To investigate the importance of *resonant* scattering we perform calculations setting $T = 0$, so hopping to the adatom is forbidden. Magnetic moments remain unchanged. Note that effectively the magnetization on the adatom is removed from the system but

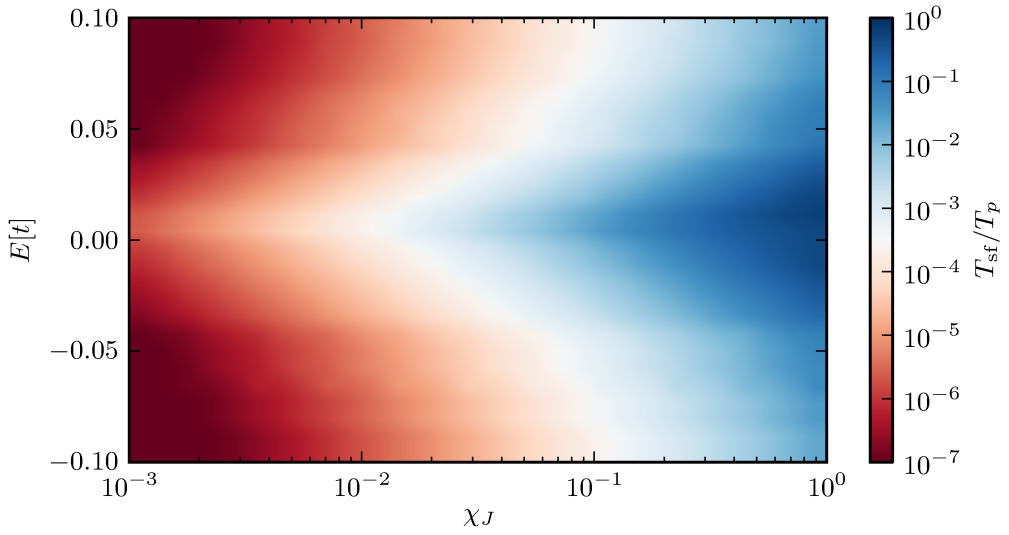

Figure 7.7.: Spin-flip ratio as a function of energy E and scaling factor χ_J. The factor χ_J is used to scale all magnetic moments involved in the model at the same time. Here, $\chi_J = 1$ corresponds to the values obtained from DFT calculations.

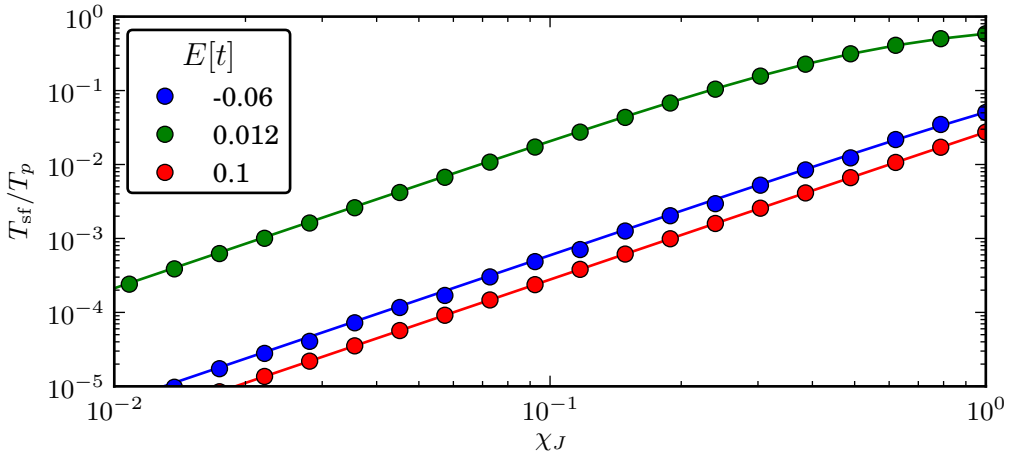

Figure 7.8.: Spin-flip ratio as a function of scaling factor χ_J for a few selected energies. Numerical data is plotted as circles, the solid lines are fits to Eq. (7.10). While the spin flip ratio at $E = -0.06t$ (blue curve) and at $E = 0.1t$ (red curve) are completely determined by a quadratic behaviour, closer to the resonance energy at $E = 0.012t$, preliminaries of a saturation can be seen.

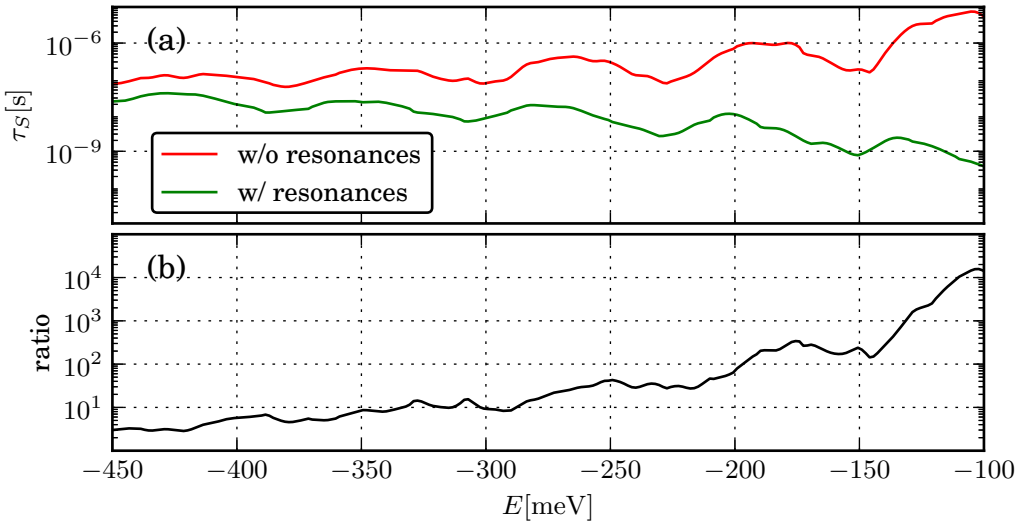

Figure 7.9.: Spin relaxation times obtained for systems with resonant impurities (green line) and with non-resonant, magnetic disorder (red line); see text for further details. The black line in the upper panel is the ratio between spin relaxation times obtained from calculations without and with resonant scatterers. Oscillations of the spin relaxation times exist due to opening of new transverse channels in the leads.

we know from model calculations in the single adatom limits that this does not necessarily imply a reduced effective magnetization because of the antiparallel alignment of the different magnetic moments. We performed calculations in the multi-channel regime which enables an extraction of the scattering length l_{tr}. This excludes energies too close to the resonance energy where the effect of resonant scattering is expected to be even larger. We plot the resulting spin relaxation times in Fig. 7.9 (a). They were calculated from the spin relaxation length assuming diffusive transport, $\tau_S = L_S^2/D$. The ratio between the spin relaxation times in the two considered cases, plotted in Fig. 7.9 (b), starts from approximately 10 for energies far from the resonance and exceeds 10^4 for the available energy closest to the resonance energy. Accordingly, spin relaxation length has a maximum ratio of 10^2 between non-resonant and resonant scattering.

To further investigate the dependence of spin relaxation on the size of the local magnetic moments we repeat the calculations with magnetic moments, modified by a factor χ_J at an adatom concentration of $\rho_H = 10^{-4}$ and for different Fermi energies.[2] From Fig. 7.10 we can identify the resonance energy slightly above charge neutrality by the high spin relaxation rate even for strongly decreased magnetic moments. We picked a set of energies used to obtain the data in Fig. 7.10 in order to achieve a better look at the dependence of L_S on χ_J. These lines are shown in Fig. 7.11. From our

[2]We chose a large concentration of adatoms to make sure there is enough intervalley scattering in the system so we can, reliably, determine the mean free path.

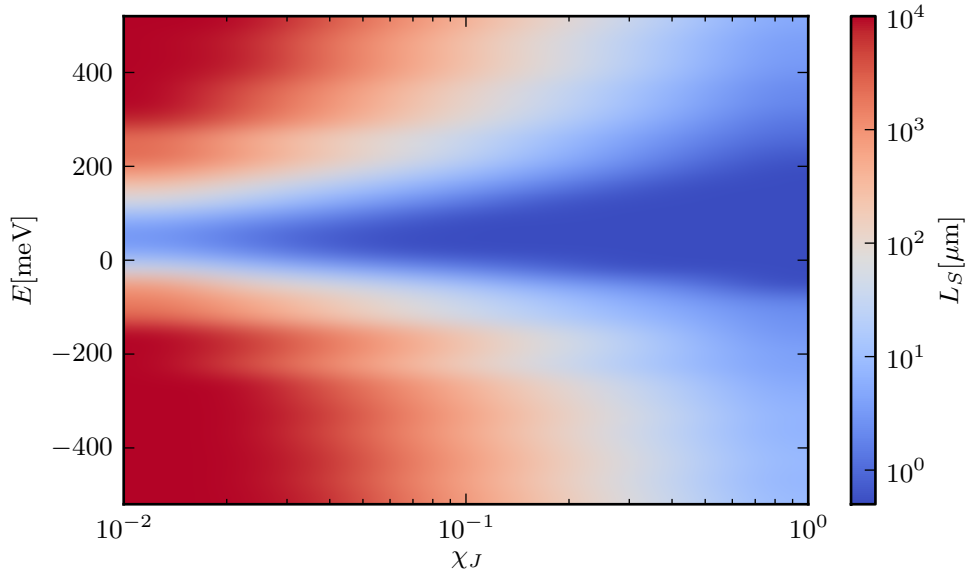

Figure 7.10.: Spin relaxation length as a function of energy E and scaling factor χ_J. A low spin relaxation length $L_S \approx 1\mu$m, i. e. a high spin relaxation rate, is seen at resonance energy. Away from that line, spin relaxation length increases up to values of several millimeters.

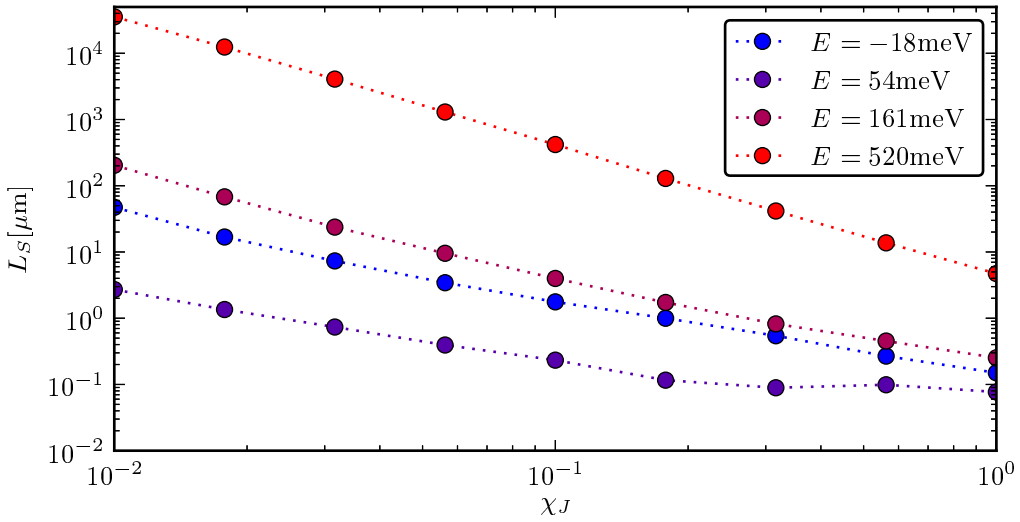

Figure 7.11.: Spin relaxation length as a function of scaling factor χ_J at different energies. For resonance energy, we observe a saturation of L_S at $\chi_J = 0.2$. For lower values it decays linearly with χ_J. At $E = 520$meV (and similarly for $E = -520$meV, which is not plotted here), L_S decays quadratically with χ_J. For intermediate energies we see a gradual transition.

discussion of the single-adatom limit it is known that spin relaxation time τ_S scales as χ_J^{-2} until it eventually saturates. Since in diffusive systems the transversed distance is associated with an average time $t = L^2/D$ we expect the spin relaxation length to scale as χ_J^{-1}. This is exactly what we find at energies close to resonance. There, the spin relaxation length saturates for $\chi_J = 0.2$ at $L_S = 100$nm. For larger energies the proportionality is rather χ_J^{-2}. This value is rather close to the average adatom-adatom distance.

The simple comparison to the single adatom calculations and the appearance of two different regimes should be handled with care. Although our numerics give no concluding answer on this issue we want to comment on the appearance of the different regimes. Spin-flip as obtained for one hydrogen adatom gives the ratio of spin-flip probability to momentum scattering rate *due to the impurity*. We now consider an additional source of momentum scattering, the Gaussian background disorder. It has been shown that the impurity state decays differently with distance from the adatom at different energies. Close to the resonance energy it is characterized by a power law decay, while off resonance it decays exponentially [108]. The increased extent of the impurity states close to resonance turns it into the dominant scatterer for both momentum and spin relaxation and, thus, adatoms govern the overall transport dynamics. A thorough analysis for spin relaxation in the presence of qualitatively different scatterers whereof only one type is sensitive to spins is needed to explain the behavior at energies far from the resonance. This, however, lies beyond the scope of this thesis.

Finally, we present the spin relaxation times extracted numerically, and extrapolate the values expected in experimental setups. Using the DFT values for the magnetic moments, $\chi_J = 1$, we extract spin relaxation times ranging from $\mathcal{O}(10\text{fs})$ at resonance energy to $\mathcal{O}(1\text{ns})$ at the edges of the examined energy range. Those calculations were performed at an hydrogen concentration of $\rho_H = 10^{-4}$. We assume that the spin relaxation rate scales linearly with the number of adatoms with an increased spin relaxation time at lower concentrations. The average distance between adatoms at the considered concentration of $\rho_H = 10^{-4}$ is 20nm. Such a large density is not expected for graphene unless added artificially. Moreover, it can be excluded that such high densities are a result of the fabrication process as they would be observed in Raman spectra or scanning tunneling microscopy. Intrinsically we expect densities around $\rho_H = 10^{-6}$, corresponding to an adatom distance of 200nm. Still, directly at the resonance energy the expected spin relaxation time is $\mathcal{O}(1\text{ps})$, off resonance we obtain an extrapolated spin relaxation time of $\mathcal{O}(100\text{ns})$.

The spin relaxation time induced by hydrogen adatoms exhibits a strong energy dependence which manifests in a spread over 5 orders of magnitude. This is an obstacle for holding hydrogen adatoms liable for the large spin relaxation rates experiments observe.

In a similar fashion, other resonant scatterers can significantly contribute to spin flip. We also performed calculations for fluorine adatoms with additional magnetic moments. Spin relaxation length was larger than for comparable hydrogen concentrations, but at fluorine densities of $\rho_F = 10^{-5}$, it was not more than a few micrometers. Moreover, the energy range used for the calculation of L_S was much larger than in the hydrogen case due to the larger width of the fluorine impurity band.

7.6. Summary

We presented and utilized an atomistic tight-binding description of graphene in the presence of adatoms. While the model is formulated in a general manner we used parameters obtained from DFT calculations for adsorbed fluorine and hydrogen adatoms. For these examples we carefully investigated different facets of electron transport and extracted the influence of different tight-binding parameters and adatom distribution on both charge and spin transport.

We find that adatoms lead to strong momentum relaxation which is not mirrored by the simpler model description used in chapter 6 where adatoms were modeled by short-range fluctuations of potential and spin-orbit coupling (SOC) terms. This reveals that the previously used model underestimates momentum relaxation from adatoms and, additionally, is not capable of reproducing the complex energy dependence we found using the atomistic description.

The investigation of spin relaxation due to randomized SOC produced a minor importance although SOC induced from adatoms locally reaches very large values. While the effective quantities, spin relaxation time and length, do not significantly differ for the atomistic description and the simpler model, the atomistic description allows for an extraction of the exact energy dependence, which is more complex than stated by Ref. [92] and found in our model calculations in section 5.2 and in chapter 6. Moreover, in consistency with our calculations of the local density of states in hydrogenated and fluorinated graphene, the importance of the newly considered PIA SOC could be made out and we explained why other spin orbit coupling terms are of minor importance.

Eventually, we showed that the formation of magnetic moments leads to a huge increase of the spin relaxation rate, and we pointed out how combined action of magnetic moments and resonant scattering imply spin relaxation rates close to experimentally found values. Fluorine and hydrogen were chosen as examples as there exist sophisticated models based on detailed investigations with *ab initio* methods. Similar influence on spin transport can, for instance, be expected from vacancies which are also known to polarize graphene magnetically and, additionally, lead to the existence of a resonant state. Finally, other adatoms or even molecules might adsorb to the graphene surface and participate in spin relaxation if they create local magnetic moments. Our study of fluorinated and, in particular, of hydrogenated graphene shows that scattering from resonant magnetic impurities should be considered the dominant source of spin relaxation in graphene.

Part II.

Edge Magnetism in Graphene

8. Introduction

Understanding graphene edges is of profound interest for the investigation of the electronic properties of graphene nanostructures. There exist peculiar electronic features which strongly depend on the orientation of the graphene edges. While *ac* nanoribbons can be either metallic or semiconducting depending on the ribbon width, *zz* nanoribbons are always metallic as they induce a localized edge state at the Fermi level [35, 119].

Over the last years the control of graphene edges in fabrication processes has been increased [120, 121] and the controlled creation of graphene nanostructures brings us closer to a *zz* based electronics where it is possible to make use of the physics of the *zz* edge state. An instructive example is given in Ref. [117] where a molecular system is put between two semi-infinite graphene sheets with atomically sharp terminations and the respective influence of armchair and zigzag boundaries is studied.

The *zz* edge state was first investigated in Refs. [35, 119] in the year 1996, eight years before the experimental observation of electronic transport in graphene [29]. As mentioned above, the *zz* edge state, in a spin-less model, closes the bandgap of graphene nanoribbons induced by the size quantization. Taking into account also the spin degree of freedom, based on the mean-field approximation of the Hubbard model for graphene [35, 119] and the extended Hubbard model [122], the *zz* edges are predicted to be magnetic at half filling, with oppositely polarized edges. Later, density functional theory (DFT) calculations [123, 124, 125, 126], exact diagonalization and quantum Monte Carlo simulations [127], as well as diagrammatic perturbation theory [128], produced results affirming the *zz* edge magnetization. While most techniques tend to long calculation times also effective tight-binding models have been extracted and been used to calculate charge and spin transport in small [129] and rather large [124] graphene nanoribbons. For a recent review see Ref. [34].

It should be mentioned that a clarifying experimental evidence of the magnetic edge state is still missing. There have been several reports about an increased density of states at *zz* edges observed in scanning tunneling microscopy and spectroscopy (STM/STS) measurements [130, 131, 132, 133]. Ref. [130] also reports a broadening of the peak in the DOS near half-filling which might be attributed to a spin-split state due to edge magnetization. The measurements, however, were not sensitive to spin polarization.

A possible way to indirectly measure edge magnetism in *zz* graphene nanoribbons is the spin conductance as suggested in Refs. [129, 134]. It was, however unclear if these predictions were directly applicable to experiments where both edge roughness and potential fluctuations can mask the effect of edge magnetism.

In this part of the thesis we will revisit the *zz* edge state focusing on its interplay with potential disorder and edge defects. Based on model calculations within the framework of the mean-field Hubbard model a phenomenological model will be presented allowing

for a fast calculation of transmission and spin-transmission in large zz nanoribbons with length up to 500nm and width up to 40nm. The phenomenological model includes local magnetic clusters in regions of charge neutrality close to zz edges.

Different relative orientations of the magnetic clusters are taken into account when calculating the transport properties of the considered systems. The results are evaluated statistically and compared to predictions from DMPK equations [135, 136]. We found a universal scaling of spin transmission T_S and its variance $\mathrm{Var}(T_S)$ in the localized transport regime. Moreover a controllable spin conductance is predicted. This work has been published as Ref. [118].

9. Magnetic Alignment with Disorder

So far, in this work a single-electron Hamiltonian has been used to describe electronic properties of graphene. Under the assumption of a negligible influence of electron-electron interactions and, moreover, owing to the computational complexity of a multi-particle treatment interactions were neglected in the previous chapters. It is, however, worth, having a closer look at charge and spin transport in graphene under the influence of electron-electron interactions to see under which circumstances the previous assumption is valid and to propose how interactions can be measured indirectly.

9.1. Hubbard model and Hartree-Fock approximation

The Hamiltonian of N electrons, interacting via Coulomb repulsion, can be written as a sum of single-particle Hamiltonians h_i and an interaction term $V_{i,j}$,

$$\mathcal{H} = \sum_{i=1}^{N} h_i(\hat{X}_i, \hat{P}_i) + \frac{1}{2} \sum_{\substack{i,j=1 \\ i \neq j}}^{N} V_{i,j}(\hat{X}_i, \hat{P}_i; \hat{X}_j, \hat{P}_j), \tag{9.1}$$

with the single-particle position and momentum operators $\hat{X}_i$ and $\hat{P}_i$.

Assuming the electron-electron interaction to act only locally due to strong screening the so called Hubbard Hamiltonian,

$$\mathcal{H}_{\text{Hubbard}} = \sum_{\sigma,\sigma'} \sum_{R,R'} t_{RR'}^{\sigma\sigma'} \, c_{\sigma,R}^{\dagger} c_{\sigma',R'} + \frac{U}{2} \sum_{R} c_{\uparrow R}^{\dagger} c_{\uparrow R} c_{\downarrow R}^{\dagger} c_{\downarrow R}, \tag{9.2}$$

can be derived (for details see Appendix B). The Hubbard model is one of the simplest multi-particle Hamiltonians treating fermions and two-particle interactions between them [137]. Equation (9.2) is a strong simplification of a general two-particle Hamiltonian and interactions are restricted to a local term. Due to Pauli exclusion interaction only between fermions of opposite spin is considered.

The Hubbard Hamiltonian, still, is a multi-particle Hamiltonian and, hence, not easily numerically treatable. The Hartree-Fock or mean-field approximation, Section B.3, maps the Hubbard Hamiltonian onto an effective single-particle Hamiltonian,

$$\bar{\mathcal{H}}_{\text{Hubbard}} = \sum_{\sigma,\sigma'} \sum_{R,R'} t_{RR'}^{\sigma\sigma'} \, c_{\sigma,R}^{\dagger} c_{\sigma',R'} + \frac{U}{2} \sum_{R} \left[\langle n_{R,\uparrow} \rangle c_{\downarrow R}^{\dagger} c_{\downarrow R} + \langle n_{R,\downarrow} \rangle c_{\uparrow R}^{\dagger} c_{\uparrow R} \right], \tag{9.3}$$

containing the expectation values of spin-up and spin-down density $\langle n_{R,\uparrow} \rangle$ and $\langle n_{R,\downarrow} \rangle$.

In literature the Hubbard Hamiltonian is often written in terms of particle number operators,

$$\bar{\mathcal{H}}_{\text{Hubbard}} = \sum_{\sigma,\sigma'} \sum_{R,R'} t_{RR'}^{\sigma\sigma'} \, c_{\sigma,R}^{\dagger} c_{\sigma',R'} + \frac{U}{2} \sum_{R} \left[\langle n_{R,\uparrow} \rangle n_{R,\downarrow} + \langle n_{R,\downarrow} \rangle n_{R,\uparrow} \right]. \tag{9.4}$$

The densities $\langle n_{R,\uparrow/\downarrow}\rangle$ are not given a priori but have to be found iteratively by performing the following calculation scheme:

1. Initial densities $\langle n^0_{R,\uparrow/\downarrow}\rangle$ suitable for the iteration are chosen.

2. $\langle n^i_{R,\uparrow/\downarrow}\rangle$ is calculated from

$$\bar{\mathcal{H}}_{\text{Hubbard}} = \sum_{\sigma,\sigma'}\sum_{R,R'} t^{\sigma\sigma'}_{RR'}\, c^\dagger_{\sigma,R} c_{\sigma',R'} + \frac{U}{2}\sum_R \left[\langle n^{i-1}_{R,\uparrow}\rangle c^\dagger_{\downarrow R} c_{\downarrow R} + \langle n^{i-1}_{R,\downarrow}\rangle c^\dagger_{\uparrow R} c_{\uparrow R}\right].$$

   The calculation scheme can be found in Appendix B.4

3. If self-consistency is reached, i. e. the change from $\langle n^{i-1}_{R,\uparrow/\downarrow}\rangle$ to $\langle n^i_{R,\uparrow/\downarrow}\rangle$ is sufficiently small, stop the iteration, otherwise return to step 2.

The resulting Hamiltonian contains an electrostatic potential acting equivalently on electrons of both spins,

$$V_{\text{eff, R}} = \frac{U}{4}\left(\langle n_{R,\uparrow}\rangle + \langle n_{R,\downarrow}\rangle\right), \tag{9.5}$$

and an Zeeman term $\mathcal{H}_{\text{eff. Zeeman}} = M_R s_z$, with an effective magnetization,

$$M_R = \frac{U}{4}\left(\langle n_{R,\uparrow}\rangle - \langle n_{R,\downarrow}\rangle\right). \tag{9.6}$$

While involving a self-consistency loop and, hence, still being rather time consuming, this approximation is computationally preferable to the full multi-particle problem.

From $\bar{\mathcal{H}}_{\text{Hubbard}}$ it appears that two factors mainly determine the influence of the interaction term: the interaction strength U and the local particle densities $\langle n_{R,\uparrow/\downarrow}\rangle$. The latter imply a notable effect of the interaction even for low interaction strength U when the particle density is large. In the next chapter it will be shown that the graphene zz edge state locally induces an interaction potential of $\mathcal{O}(10\text{meV})$ even for low U.

9.2. Searching for the magnetic edge state

In 1996, for the first time the mean-field Hubbard Hamiltonian has been used to investigate graphene in Ref. [35]. For bulk graphene, an antiferromagnetic ordering of the spins on the two sublattices is predicted if $U > 2t$.

At zz terminations and in particular in zz graphene nanoribbons, at half-filling a notable effect occurs also for small values of U, $U < 1t$. This is possible as graphene possesses a particular solution at energies close to 0 if the graphene system contains a zz edge implying a strongly increased local density of states at the zz edge. The corresponding states decay exponentially from the edge with a decay length γ. The decay length γ has its minimum at $k = \pi/a$. For that solution only the outermost atoms are occupied. When k deviates from π/a the decay length γ increases reaching the extended states at the K-points. With the interactions included on the mean-field level it turns out that these states are additionally spin-polarized with opposite signs

for the two sublattices. Graphene nanoribbons with zz terminations, while still being magnetically neutral, obtain oppositely magnetically polarized edges. Additionally a gap is opened from the electron-electron interaction lifting the degeneracy of the edge states. In Fig. 9.1 we show an example of a bandstructure of a zz edge state and the resulting magnetization as defined in equation (9.6).

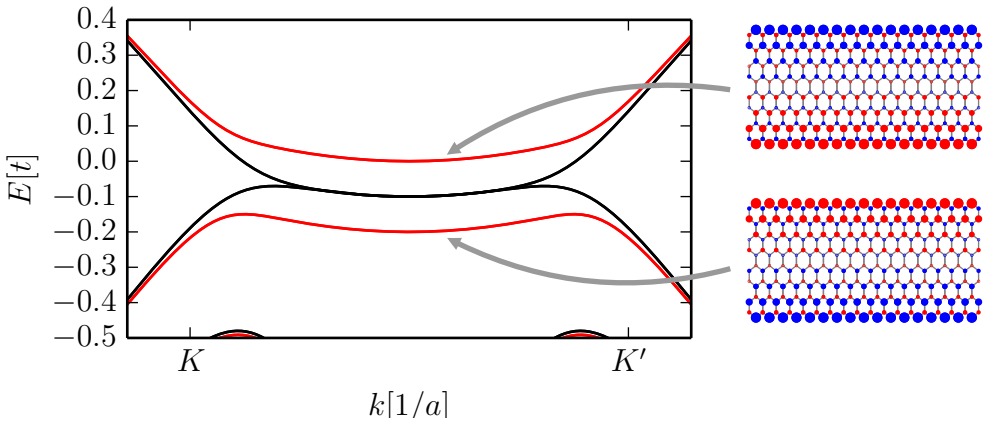

Figure 9.1.: Bandstructure of a graphene nanoribbon with (red) or without (black) magnetic ordering. The magnetic ordering leads to the opening of a gap, lifting the spin degeneracy of the edge states. The magnetic texture of the ribbons is shown in the two sketches next to the bandstructure with blue (red) indicating positive (negative) magnetization and circles sized proportional to the magnetization strength.

The original calculation was carried out for ribbons 2nm wide at constant potential without edge defect. Later calculations with other mean-field techniques as the extended Hubbard model [119] or density functional theory [123, 124, 125, 126] confirmed the magnetic edge state for systems of the same size. Moreover, Son et al. [123] proposed a finite spin conduction of graphene nanoribbons at half-filling under the influence of an transverse in-plane electric field. At edge defect rates of $6 - 12\%$ the finite spin conductance vanishes.

The edge state and its magnetic properties also result from calculations beyond mean-field approximation. In small systems it has been confirmed by direct diagonalization and in larger systems by quantum monte carlo simulations [127].

As the high density of states at zz edges is responsible for the magnetic ordering a restriction to clean zz nanoribbons is very strong, but, indeed, again using a Hartree-Fock Hubbard Hamiltonian, it has been shown that at zz edges of graphene nanoislands magnetic ordering happens within the mean-field Hubbard model [138].

A controversy has been introduced by Refs. [139, 140]. In both works different types of edge passivation are compared finding more stable solutions than the monohydrogenated edge, which is usually assumed in tight-binding simulations of graphene nanostructures and which is an essential ingredient for magnetic ordering along the edges. Other types of passivation are not magnetic and, in most cases, even do not exhibit an edge state. Furthermore Kunstmann et al. [140] state how doping decreases

magnetic ordering mediated by the building up of charge puddles which weaken edge magnetism significantly.

Experimentally, scanning tunneling microscopy has been used to investigate the graphene edges in Refs. [131, 132, 133]. These works agree on the observation of an increased density of states on edges identified as zz edges compared to bulk graphene or ac edges.

Magnetism has been observed in several forms. Nair et al. [141] find paramagnetism in graphene attributing this finding mainly to adatoms and vacancies. Ramakrishna Matte et al. [142] measure a small, but finite hysteresis in the magnetization of their graphene flakes as a signature of ferromagnetism. They also observe signatures of antiferromagnetism. The presence of ferromagnetic impurities is ruled out so that the magnetic properties are assumed an intrinsic property of the graphene samples. A clear attribution to a single source, however, is not possible. Good candidates other than the magnetization due to electron-electron interactions are defects or non-magnetic adatoms. Joly et al. [130] performed eletron spin resonance (ESR) measurements on different graphene samples observing a split state in the ESR spectrum with an intensity showing the same temperature dependence as the edge state. From that they conclude to have found the magnetic edge state. Other sources of magnetism, however, were not ruled out.

Apparently, a clear experimental evidence is still missing. Charge and spin transport have been ignored so far for this purpose. An obstacle, probably, was the supposed sensitivity of edge magnetism to potential disorder. In the remainder of this part of the thesis we want to show that edge magnetism would be observed even in the presence of potential fluctuations and how its signature in transport experiments could be observed.

In order to interpret electron transport in the context of edge magnetism a profound understanding of its mechanisms in realistic systems is essential. For this purpose a phenomenological model based on mean-field calculations for graphene nanoribbons shall be developed.

9.3. On the route to a phenomenological model

The starting point for the phenomenological model is the solution for graphene nanoribbons without any defects at half-filling. Solutions for systems $10a$ wide at $U = 0.8t$ are shown in Fig. 9.2. Figure 9.2 (a) illustrates the magnetization, equation (9.6), across the ribbon for $E_F = 0t$. The antiferromagnetic alignment of the two sublattices is clearly visible. The absolute value of the magnetization reaches its maximum $\pm M_0$ on the outermost atoms. Plotting M_0 as a function of Fermi energy E_F reveals that maximal magnetic ordering occurs when one edge state is fully occupied; See Figs. 9.2 (b) and (c). Figures 9.2 (b) and (c) also indicate how next-nearest neighbor coupling influences the system. As in the spinless case electron-hole symmetry is broken by coupling between next-nearest neighbors and that, accordingly, the edge state is shifted to lower energies.

The parameters of the simulation were chosen to reproduce results from Refs. [124, 143, 144]. The best agreement to the energy dispersion shown in Ref. [124] is achieved

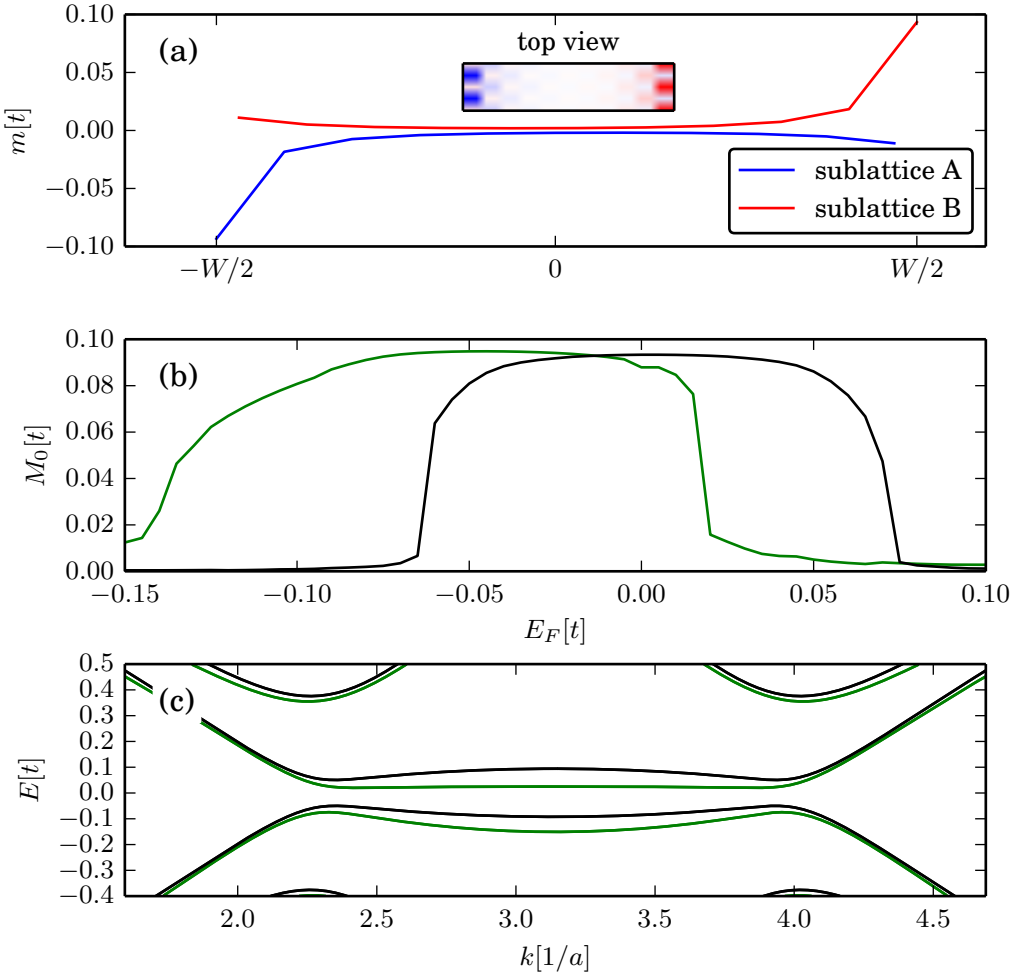

Figure 9.2.: Solution of $\mathcal{H}_{\text{Hubbard}}$ for ribbons $10a$ wide for $U = 0.8t$. (a) Magnetization across the ribbon for different values of the Fermi energy. The peak value $\pm M_0$ is reached on the rightmost / leftmost atom for sublattice A $/B$. The inset shows a colorplot of the magnetization in the graphene plane at half-filling. (b) M_0 as a function of Fermi energy E_F for $t' = 0$ (black) and $t' = 0.067t$ (green). (c) Band structure of the system for the nearest-neighbor hamiltonian (black line) and including next-nearest neighbor hopping (green).

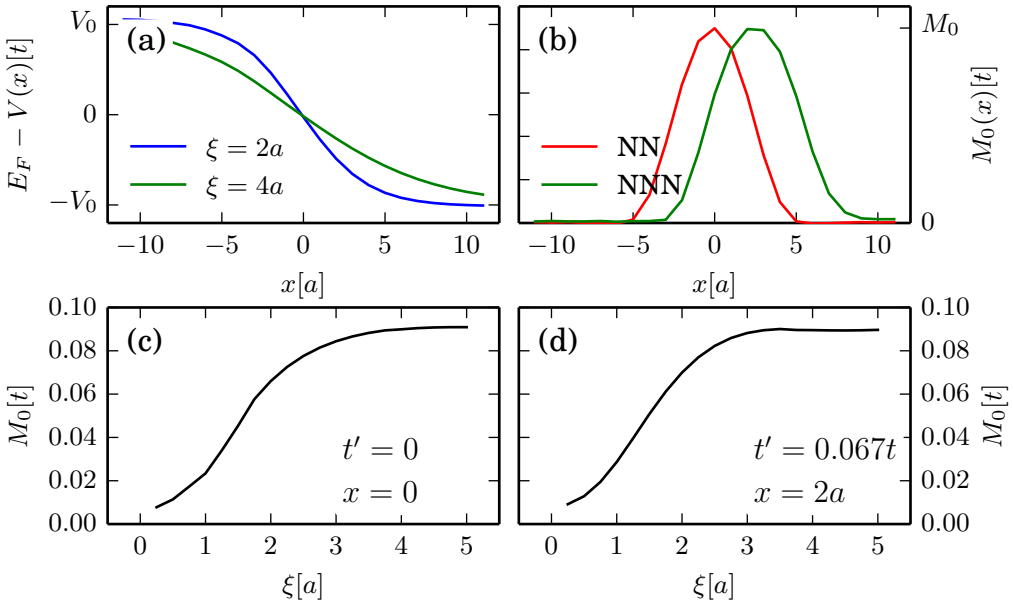

Figure 9.3.: (a) Potential along a graphene zz nanoribbon containing a smooth potential step for different extensions ξ of the step. (b) Magnetization profile along the nanoribbon as calculated from the mean field Hubbard model including nearest neighbor coupling (NN) and next-nearest neighbor coupling (NNN). The peak magnetization at the ribbon edges plotted as a function of smearing factor ξ of the potential step without (c) and with (d) next-nearest neighbor hopping considered.

by setting $t' = 0.08t$ and $U = 0.8t$. If not mentioned otherwise these parameters have been used to calculate the presented results.

We now also include electrostatic potential in our system in view of considering disorder effects on the edge magnetization. In a first step this is done by considering potential steps and barriers. The external potential profile is given by

$$V(x) = V_0 \left(\frac{1}{1 + \mathrm{e}^{(x-x_0)/\xi}} - 0.5 \right), \tag{9.7}$$

for the potential step and by

$$V(x) = V_0 \left(\frac{1}{1 + \mathrm{e}^{(x-x_1)/\xi}} - \frac{1}{1 + \mathrm{e}^{(x-x_2)/\xi}} + 0.5 \right), \tag{9.8}$$

for the potential barrier. Here x is the longitudinal coordinate within the nanoribbon, x_0, x_1 and x_2 indicate the positions of the potential steps. By varying ξ the smoothness of the junction can be controlled. The height of the potential step / barrier is given by V_0; see Fig. 9.3 (a) as well as Figs. 9.4 (a) and (b). Calculating the magnetization from the Hubbard Hamiltonian yields a finite value at the p-n junction close to the

zz edge. Fig. 9.3 (b) shows how $\langle m \rangle$ evolves along the ribbon. With next-nearest neighbor coupling the maximum is reached at a different position than without which can be understood from the calculations for the clean ribbons.

For a sharp junction, $\xi \approx a$, the magnetization does not exceed a small fraction of the bulk value, i. e. the magnetization obtained for constant potential at half-filling. While increasing the smoothness ξ of the junction M_0 increases until converging against the bulk value at $\xi \approx 4a$; see Fig. 9.3 (c) - (d).

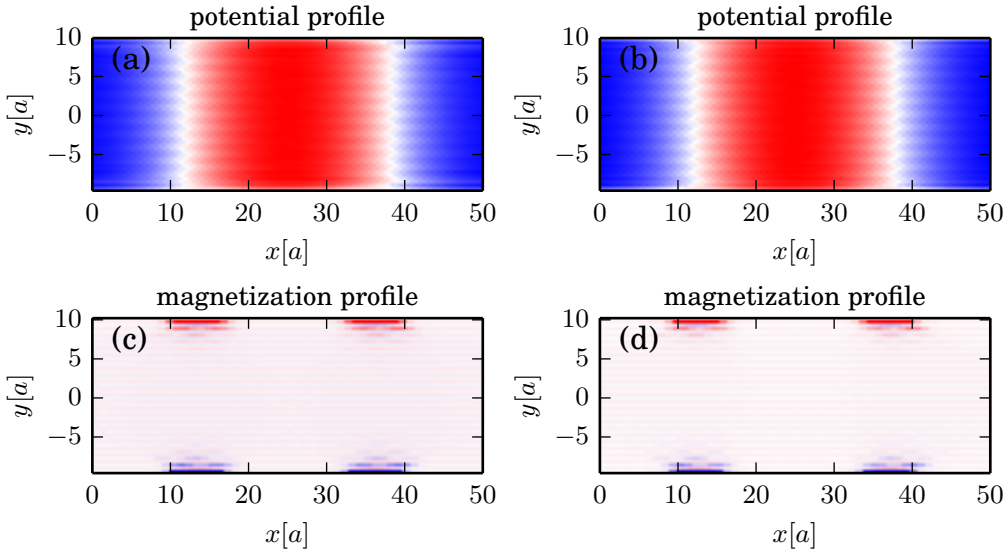

Figure 9.4.: Results of the self-consistent loop (Appendix B.4) for a graphene nanoribbon with a p-n-p junction. (a), (b) potential and (c), (d) magnetization profile after iteration without (a),(c) and with (b),(d) next-nearest neighbor hopping.

Similarly, for the slightly more complex case of a potential barrier a finite magnetization builds up at the charge neutrality points at the edges.

For Fig. 9.4(a) and (c) only nearest neighbor hopping is assumed. The Fermi energy is exactly $E_F = 0t$, the local doping, hence, ranges from $V_{\text{min}} = -0.25t$ to $V_{\text{max}} = 0.25t$.

Next-nearest neighbor coupling is included in the calculations for Figs. 9.4 (b) and (d). The Fermi energy in that case is $E_F = -0.06t$, potential ranges from $V_{\text{min}} = -0.31t$ to $V_{\text{max}} = 0.19t$. The magnetization reaches peak values of $M_0 = 0.05t$.

Calculations are, then, carried out for completely disordered systems, subjected to the formerly used disorder potential,

$$V_{\text{dis}}(\boldsymbol{x}) = \sum_{i=1}^{N} V_i \mathrm{e}^{-\frac{|\boldsymbol{x}-\boldsymbol{x}_i|^2}{2\sigma}}, \tag{5.2}$$

composed of N Gaussian scatterers centered around positions $\boldsymbol{x}_i$, each inducing a local potential V_i at $\boldsymbol{x}_i$ decaying with a characteristic length σ.

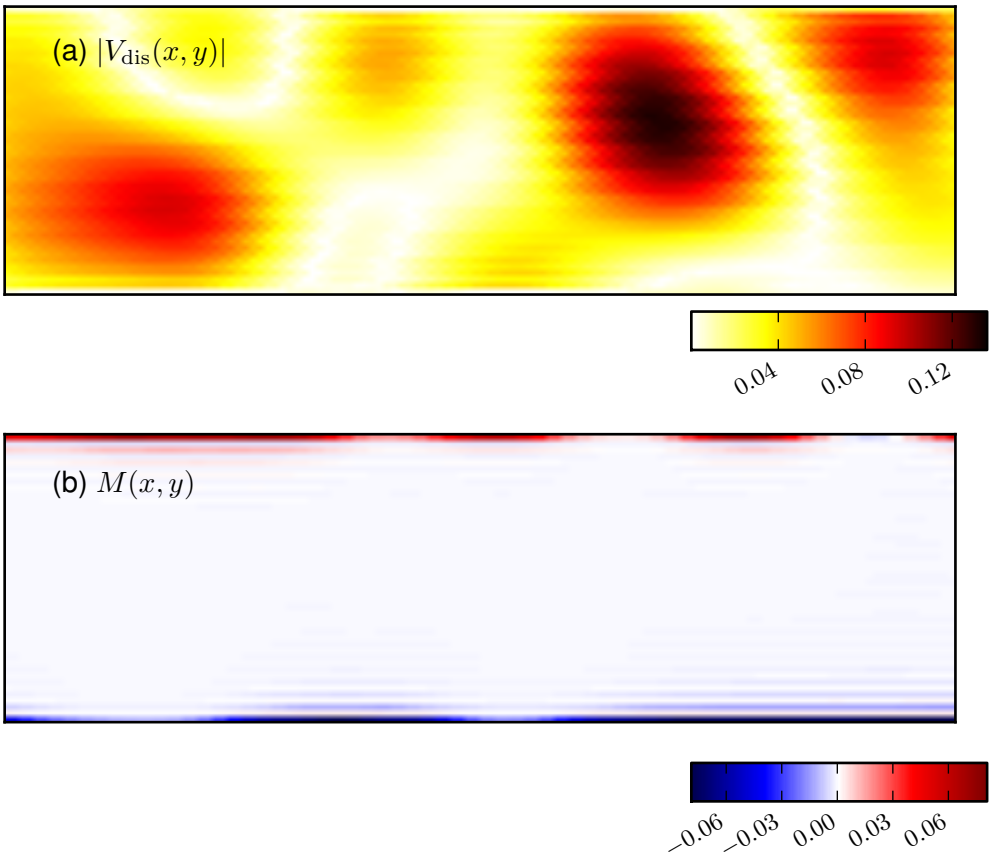

Figure 9.5.: Effective potential of a disordered graphene nanoribbon. (a) Absolute value of the electrostatic potential. (b) Magnetic moments. Magnetization is maximal where the potential $|V_{\mathrm{dis}}(\boldsymbol{x})|$ is close to 0 and vanishes above a certain threshold.

The magnetization obtained for that case, in line with the previous calculations, is finite at the edges where the local doping is close to charge neutrality; see Fig. 9.5 for an example.

9.4. Using the results for transport calculations

While the mean field Hubbard Hamiltonian is computationally preferable compared to a real multi-particle Hamiltonian, and it, moreover, allows for the treatment of large systems it still contains the self-consistency loop. The iteration involves calculating the system's Green's function G^r at several energies in the interval $E \in [E_{\mathrm{min}}, E_F]$ in order to calculate the electron density at E_F (see App. B.3). The calculation of the $G^r(E_F)$ and the scattering matrix from the converged mean-field Hamiltonian requires

only a small fraction of the time used to calculate the Hamiltonian itself. In Ref. [124] a constant magnetization is assumed, approximating solutions from DFT calculations, to skip the self-consistent loop and, hence, allowing for an efficient calculation of electron transport in large systems and for obtaining a sufficiently large amount of data for a statistical analysis.

In Ref. [124] the assumption of a constant magnetization along the ribbon is used. Here, we present a new model of the intrinsic magnetization of graphene in the presence of potential disorder. Owing to the potential fluctuations, instead of choosing a constant magnetization the magnetization is assumed to be finite only near edges with a local doping close to charge neutrality. Hence, edge atoms with a potential such that $E_{\text{low}} < E - V(\boldsymbol{x}) < E_{\text{high}}$[1] are chosen as the centers of magnetic clusters which form along the edges; See Fig. 9.6 for a demonstration. The magnetization is

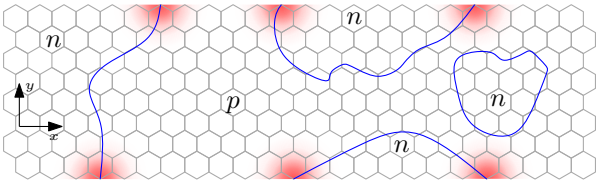

Figure 9.6.: Formation of local *zz* edge magnetic moments. Whenever isopotential lines (blue) separating n-doped from p-doped regions hit an edge, a finite magnetization is locally assumed (red); see Ref. [118]

further assumed to decay with a distance d from the clusters' centers as a Gaussian $\exp[-(d/d_0)^2]$, where d_0 is a phenomenological decay length. Within these clusters the magnetization has an opposite sign for sublattice A and B, but the net magnetization of a single cluster is nevertheless finite.

The complete Hamiltonian becomes

$$\mathcal{H} = \sum_{i,s} V(\boldsymbol{r}_i) c^\dagger_{i,s} c_{i,s} + \sum_{i,j,s} t_{i,j} c^\dagger_{i,s} c_{j,s} + \sum_{i,s,s'} \xi_i c^\dagger_{i,s} (\boldsymbol{m}_i \cdot \boldsymbol{\sigma})_{s,s'} c_{i,s'}, \tag{9.9}$$

where the sums run over atomic sites i, j and real spin indices s and s'. Here $t_{i,j} = t$ if the atoms i and j are nearest neighbour, $t_{i,j} = t'$ if the are next-nearest neighbors and zero otherwise. $\boldsymbol{\sigma} = (\sigma_x, \sigma_y, \sigma_z)$ is the vector of Pauli matrices in real spin space. ξ_i is a sublattice dependent factor and takes the value $+1$ (-1) on sublattice A (B). The last term in the Hamiltonian $\mathcal{H}$, hence, acts like a Zeeman term with different signs on the two sublattices. Its orientation and absolute value are position dependent,

$$\boldsymbol{m}_i = \sum_{l=1}^{N_\text{c}} \boldsymbol{M}_l \mathrm{e}^{-\left(\frac{d_{i,l}}{d_0}\right)^2}, \tag{9.10}$$

i. e. to determine the magnetization at an atomic site i, its distance $d_{i,l}$ from all the N_c magnetic clusters l is determined.

[1] The choice of E_{low} and E_{high} depends on the other system's parameters. Without next-nearest neighbor coupling the energy interval is chosen symmetrically around $E = 0t$, the size of the interval is of the order $\mathcal{O}(0.01t)$.

Note that an individual magnetization $\boldsymbol{M}_l$ is assigned to each magnetic cluster while the Hubbard Hamiltonian presented in the previous section would predict a uniform magnetization $\boldsymbol{M}_l$ for all clusters. Moreover, in Eqs. (9.9) and (9.10) the magnetization $\boldsymbol{m}_i$ and also the cluster magnetization $\boldsymbol{M}_l$ have been introduced as vectors. This goes beyond the Hubbard Hamiltonian, where only a distinction between spin-up and -down is possible, and, furthermore, it is taken into account that the single clusters need not be correlated. For the relative alignment of the clusters several possible cases are investigated within this thesis to compensate for the lack of a selfconsistent determination of the magnetization.

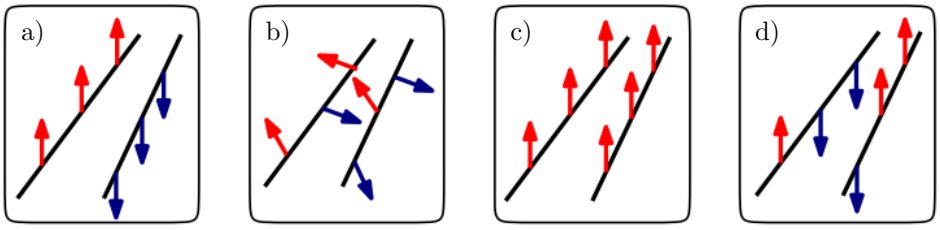

Figure 9.7.: Visualization of the different models used to describe the edge magnetization in disordered graphene nanoribbons. (a) - (c) represent the models corresponding to the respective labels of the descriptions in the text. The relative alignment on the clusters indicated in (d) is obtained if edge disorder randomizes the magnetic moments within model (a) and (c).

(a) Fully correlated magnetic clusters. All clusters have the same magnetization vector $\boldsymbol{M}_l = \boldsymbol{M}$. This is the solution directly deduced from the results in section 9.3. If the magnetic cluster formed at an edge segment is mainly composed of atoms of sublattice A (B) its net magnetization is pointing parallel (antiparallel) to $\boldsymbol{M}$. Without edge disorder this leads to lined up magnetic moments along the edges; see Fig. 9.7 (a).

(b) Uncorrelated clusters. In a contrary situation, one could also assume totally uncorrelated clusters. The mean-field description used to derive the antiferromagnetic alignment of the sublattices of graphene is not able to determine a preferred axis along which the electrons spins align. Magnetic moments at different p-n junctions need not be aligned nor collinear. Thus, it is a natural and realistic extension of model (a) to assign a random direction to the magnetization at each p-n junction; see Fig. 9.7 (b).

(c) Ferromagnetic alignment. This model is similar to model (a). The clusters, however, get assigned a direction that additionally depends on the edge they are lying on. Clusters with mainly edge atoms of sublattice A (B) point upwards (downwards) on the left edge and downwards (upwards) on the right edge; see Fig. 9.7 (c). Formally the Hubbard model allows for this solution as shown for clean zz nanoribbons (cf. Fig. 4 in Ref. [144]). This phase might be triggered by applying a small magnetic field Ref. [144].

By introducing defects along the nanoribbon termination an edge does not consist of only one sublattice anymore and, for models (a) and (c), also the magnetization gets randomized. This is visualized in Fig. 9.7 (d). We find numerically that the amount of randomization depends on the number of defects along the edges.

With the model laid out here we performed numerical transport calculations for disordered graphene nanoribbons. The calculations' results are to subject of the following chapter.

10. Transport calculations

10.1. Formalism

Electron transport is calculated in linear response approach with the generalized formular for the spin conductance,

$$G^{\mu\nu} = g_0^{\mu\nu} \operatorname{Tr}(t^\dagger s^\mu t s^\nu), \tag{10.1}$$

including the Pauli matrices $s^{\mu/\nu}$ in real spin space. The scattering matrix t is calculated from the system's retarded Green's function which, in turn, is calculated by a recursive Green's function method; see Chapter 2.

We are particularly interested in the charge conductance,

$$G^{00} = \frac{e^2}{h} \operatorname{Tr}(t^\dagger t), \tag{10.2}$$

and the spin conductance,

$$G^{z0} = \frac{e}{4\pi} \operatorname{Tr}(t^\dagger s^z t) = \frac{e}{4\pi}(T_{\uparrow\uparrow} + T_{\uparrow\downarrow} - T_{\downarrow\uparrow} - T_{\downarrow\downarrow}), \tag{10.3}$$

or the dimensionless quantities, total transmission $T = G^{00}/\frac{e^2}{h}$ and spin transmission $T_S = G^{z0}/\frac{e}{4\pi}$.

We model transport through graphene nanoribbons in the presence of random long-range disorder [Eq. (5.2)] with $V_{\text{dis}} = 0.12t$, $\sigma_{\text{dis}} = 4a$. For model (b), also the orientation of the magnetic moments at different p-n junctions is randomized. Both nanoribbons with smooth and rough edges were considered. Edge disorder is created by iterating over the edge atoms and removing them with a probability of 2%. This procedure was repeated up to ten times to increase edge disorder and to extend the size of edge defects. The edge disorder acts as an additional source of momentum scattering. It also randomizes the magnetic moments along an edge. Hence, model (a) and (c) become very similar in the presence of edge disorder; see Fig. 9.7(d)

The considered ribbons are $40-50$nm wide and $500\text{nm}-1\mu$m long. For the magnetic clusters defined in Eq. (9.10) we chose different values for the peak magnetization $|M_l|$ in the range $[0.01t, 0.1t]$ and the phenomenological decay length d_0 in the range $[2a, 3a]$. The exact choice of the magnetization parameters was only of marginal effect in all our simulations and the results presented in this chapter are valid for all considered values of $|M_l|$ and d_0.

The transport properties were calculated in a wide energy range. Here we shall restrict ourselves to the vicinity of the charge neutrality point where the effect of the edge magnetism is visible. To be more precise, the energy range of interest is defined by the strength of the potential fluctuations. Edge magnetism influences transport

through the nanoribbon only when the local doping of the edge atoms lies within a certain interval around the charge neutrality point. We choose the interval to be $\pm 0.03t$ around the charge neutrality point – smaller than for the model calculations presented in chapter 9, bearing in mind the, on average, reduced magnetization at p-n junctions. Note that the potential disorder increases the energy range, edge magnetism can be observed within compared to the clean case.

10.2. Localized mesoscopic transport

In Fig. 10.1 the average total and spin transmission, $\langle T \rangle$ and $\langle T_S \rangle$, as well as their fluctuations, $\mathrm{Var}\, T$ and $\mathrm{Var}\, T_S$, are plotted as functions of the Fermi energy for the different models of edge magnetization. Averages are calculated as ensemble averages, the variance can be understood as the size of the sample-to-sample fluctuations. Apparently, the transmission is very small, $\langle T \rangle < 1$ for all systems. Except for model (c), spin transmission $\langle T_S \rangle$ is suppressed. For the ferromagnetically aligned ribbons the position of the peaks in the spin transmission is given by the value of the magnetization. This will be explained later.

The variance of the spin transmission, $\mathrm{Var}\, T_S$, is proportional to the variance of the total transmission, $\mathrm{Var}\, T$, within the considered energy range and is always finite. While both quantities coincide for models (a) and (c), they differ for model (b). To understand the differences in model b we have to keep in mind that the spin creation conductance with respect to the z-axis is considered. The totally disordered model, however, creates a finite spin conductance for every possible quantization axis depending on the particular system. To obtain the data in Fig. 10.1 we projected to the z-axis.

Apparently, transport takes place in the localized regime. For the given system widths and energy the number of open channels varies between 2 and 50. The probability distribution of transmission eigenvalues in mesoscopic systems can be described by the Dhorokov-Mello-Pereyra-Kumar (DMPK) equations [135, 136]. From random matrix theory it follows that for localized systems, i. e. when the system length L is larger than the localization length ξ, the transmission eigenvalues approach a log-normal distribution in the limit $L/\xi \to \infty$ [103]. In the case of localized mesoscopic transport an analytical solution of the DMPK equation exists yielding the mean and the variance of $\ln T$ [145],

$$-\langle \ln T \rangle = \frac{1}{2} \mathrm{Var}(\ln T) = 2\frac{L}{\xi}. \tag{10.4}$$

This implies that the whole dynamics is governed by the single parameter ξ/L. We, hence, extracted ξ/L from numerically calculated transmission of a large number of ribbons by making use of Equation (10.4). The numerical results, see the black in lines Figs. 10.2 (a) and (b), reveal that the variance of the charge transmission for different samples plotted as a function of the system's normalized localization length, ξ/L, follows a universal curve which is given by Equation (10.4). Moreover also the spin transmission, red lines in Fig. 10.2, follows this universal behavior.

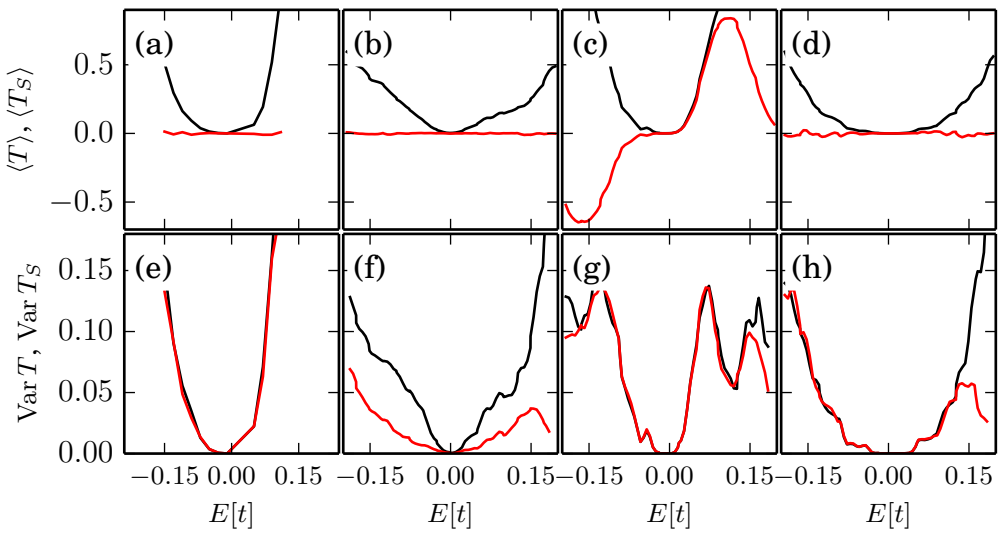

Figure 10.1.: (a) - (d): Average value of T (black) and T_S (red), different panels correspond to the different models as shown in Figs. 9.7 (a) - (d), respectively. (e) - (h): Sample to sample fluctuations of transmission T (black) and spin transmission T_S (red). For their calculation the same models as for Figs. 9.7 (a) - (d) were chosen, respectively.

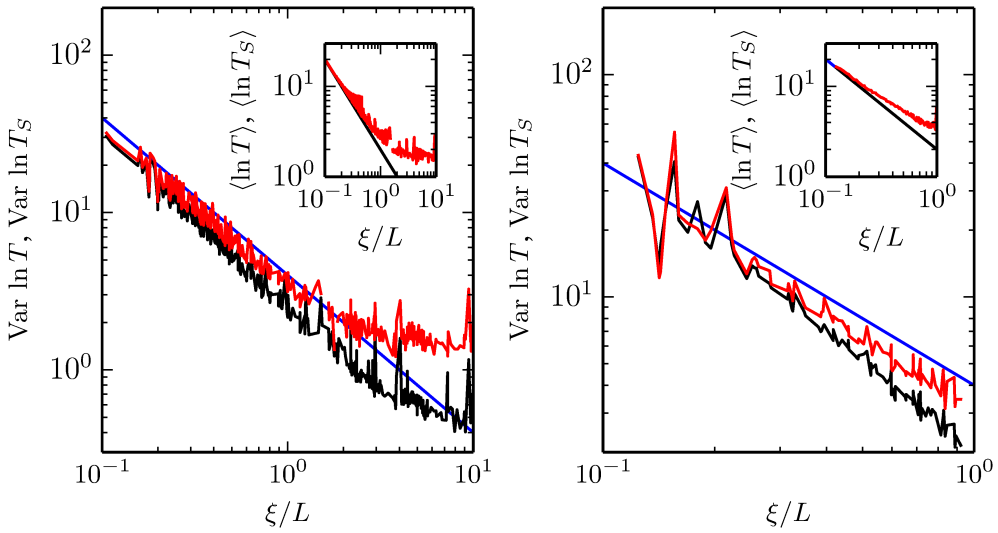

Figure 10.2.: Universal scaling of $\mathrm{Var}\ln T$, $\mathrm{Var}\ln T_S$ with respect to ξ/L, for (a) model (a), collinear magnetic moments along the edges, and (b) model (b), completely randomized magnetic moments. The insets show $\langle \ln T_S\rangle$ as a function of ξ/L. Blue lines correspond to predictions from DMPK equations.

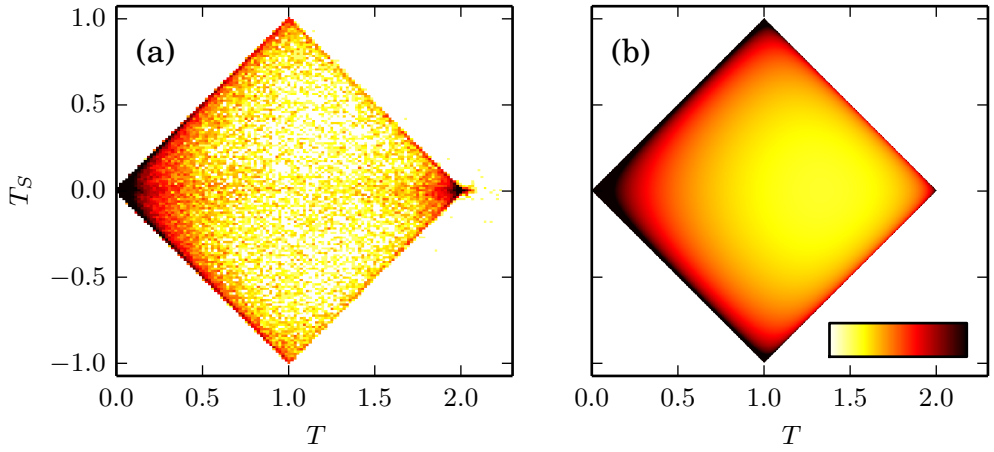

Figure 10.3.: Statistical analysis of the distribution of T-T_S pairs as (a) obtained from numerical calculations for an ensemble of ≈ 150000 ribbons and (b) using a model of uncorrelated transmission function for electrons of spin-up and spin-down electrons.

In the following we want to develop an analytic model depending only on the scaling parameter and use it to explain how spin conductance of graphene nanoribbons might be controllable.

10.2.1. Decomposition

Focusing on systems with local moments only along the z-axis [models (a) and (c)] we decompose the Hamiltonian and the scattering matrix into blocks for electrons with positive or negative spin eigenvalue. The transmission and spin transmission become the sum and the difference, respectively, of the transmission for spin-up and -down electrons,[1]

$$T = T_\uparrow + T_\downarrow, \tag{10.5}$$
$$T_S = T_\uparrow - T_\downarrow. \tag{10.6}$$

The transmission probabilities of the two blocks are described by a distribution function $P_0(T_\uparrow, T_\downarrow)$, which, under the assumption of negligible correlations between the spin-subblocks, can be factorized as $P_0(T_\uparrow, T_\downarrow) = P_\uparrow(T_\uparrow)P_\downarrow(T_\downarrow)$.

[1] For the sake of simplicity we use a shorter notation, replacing $T_{\uparrow\uparrow}$ and $T_{\downarrow\downarrow}$ by $T_\uparrow$ and $T_\downarrow$, respectively. The spin-flip probabilities $T_{\uparrow\downarrow}$ and $T_{\downarrow\uparrow}$ are suppressed as the Hamiltonian contains only terms diagonal in spin space.

It has been shown by Brouwer and Frahm [146] that the thick wire limit of the DMPK equations[2] is equivalent to the 1D σ model and that, hence, the transmission $\tilde{T}$ of such a system follows a binodal distribution

$$P(\tilde{T}) \propto \frac{1}{\tilde{T}\sqrt{1-\tilde{T}}}. \tag{10.7}$$

We can make use of Equation (10.7) at least for a qualitative understanding as it agrees with the numerical data found for the individual spin subblocks (not shown here) and, moreover, allows for a calculation of the expectation values of the total transmission T and the spin transmission T_S. In Fig. 10.3 we compare the probability distribution in the T-T_S plane obtained from the binodal distribution, Equation (10.7), under the assumption of uncorrelated spin-subblocks with the one obtained from numerical calculation. Characteristic features are present in both diagrams such as the points of increased density at $T = T_S = 0$ and at $T = 2.0$, $T_S = 0$ as well as the lines of slope ± 1 representing the case of one spin channel being transmitted while the other one is fully localized.

After the demonstration that the individual subsystems can be treated as being uncorrelated, we, additionally, consider them as localized electronic systems governed by two individual scaling parameters $K_{\uparrow/\downarrow} = L/\xi_{\uparrow/\downarrow}$ given by the inverse normalized localization lengths. The average transmissions, hence, are given by

$$\langle T_{\uparrow/\downarrow} \rangle = \mathrm{e}^{-L/\xi_{\uparrow/\downarrow}}, \tag{10.8}$$

resulting in and average total and spin transmission, given by,

$$\langle T \rangle = \langle T_\uparrow \rangle + \langle T_\downarrow \rangle = \mathrm{e}^{-L/\xi_\uparrow} + \mathrm{e}^{-L/\xi_\downarrow}, \tag{10.9}$$

$$\langle T_S \rangle = \langle T_\uparrow \rangle - \langle T_\downarrow \rangle = \mathrm{e}^{-L/\xi_\uparrow} - \mathrm{e}^{-L/\xi_\downarrow}. \tag{10.10}$$

10.2.2. Average values

For further use we define

$$\Delta_M = \left\langle \frac{M_\uparrow - M_\downarrow}{M_\uparrow + M_\downarrow} \right\rangle, \tag{10.11}$$

the average difference of edge atoms with positive and negative magnetization divided by the total number of magnetized edge atoms, ranging from -1 to $+1$.

Moreover we assume that the scaling parameters $K_{\uparrow/\downarrow}$ are given by a spin-independent component L/ξ_0 and a contribution linear in Δ_M,

$$K_{\uparrow/\downarrow} = \frac{L}{\xi_0} \pm c\Delta_M. \tag{10.12}$$

[2] By thick-wire limit we refer to the limit of many open channels, $N \to \infty$, at short mean free path, $L/l_{tr} \to \infty$.

We find this assumption justified by our numerical results. Higher orders of Δ_M are not needed. Inserting these scaling factors in equations (10.9) and (10.10) we find

$$\langle T \rangle = \mathrm{e}^{-L/\xi_0} \cosh(c\Delta_M), \tag{10.13}$$

$$\langle T_S \rangle = \mathrm{e}^{-L/\xi_0} \sinh(c\Delta_M). \tag{10.14}$$

Expanding for small values of $c\Delta_M$ shows that, to leading order in $c\Delta_M$, average total transmission is independent of the magnetization,

$$\langle T \rangle = \mathrm{e}^{-L/\xi_0} + \mathcal{O}(c^2\Delta_M^2), \tag{10.15}$$

while average spin transmission linearly depends on Δ_M,

$$\langle T_S \rangle = \mathrm{e}^{-L/\xi_0} c\Delta_M + \mathcal{O}(c^3\Delta_M^3). \tag{10.16}$$

Finite spin transmission is achieved by an average net-magnetization and can be controlled by creating an excess of positive (negative) magnetic clusters.

10.3. Controllable finite spin conductance

The local Fermi level $E(\boldsymbol{x}) = E_F - V(\boldsymbol{x})$ varies along the edges due to the random disorder potential. For the Gaussian disorder with parameters we chose for the simulations, $E(\boldsymbol{x})$ exhibits a Gaussian distribution centered around E_F with a width σ_E determined by the disorder peak strength V_{dis}. Only atoms with a local doping within a given energy range are valid centers of magnetic clusters. The number of $M_{L(R)}$ magnetized out of $N_{L(R)}$ atoms along the left (right) edge is given by

$$M_{L(R)} = N_{L(R)} \int_{E_{\mathrm{min}}}^{E_{\mathrm{max}}} P_{\mathrm{doping}}(E)\mathrm{d}E. \tag{10.17}$$

For model (c), ferromagnetically aligned edges, an upper and a lower energy range can be given. Edge atoms in the upper (lower) energy range constitute the centers of positively (negatively) oriented magnetic clusters. The positions of the energy ranges are fixed by the interaction strength in the Hubbard model. For this case, Δ_M is determined by the Fermi level and is controllable by changing the overall doping. Peaks of the spin transmission should be given at energies corresponding to the spin-polarized edge states. This is confirmed by numerical simulations as shown in Fig. 10.1 (c).

Model (a) deviates characteristically from this picture. For clean edges the magnetization of clusters at the left (right) edge are pointing upwards (downwards),

$$M_{\uparrow/\downarrow} = M_{L/R}. \tag{10.18}$$

An imbalance of the magnetic clusters can be created by an imbalance of the cluster distribution along the edges. This can be accomplished by applying a transverse in-plane electric field, which in turn can be approximated by a linear potential drop V_{tilt}

between the two edges. That is why the doping distributions for left and right edge, $P_{L/R}(E)$, have different expectation values,

$$P_{L/R}(E) = \frac{1}{\sqrt{2\pi}} \mathrm{e}^{-[E-(E_F \pm V_{\mathrm{tilt}}/2)]^2/(2\sigma_E^2)}. \tag{10.19}$$

We, hence, can calculate Δ_M as a function of potential drop V_{tilt} and broadening σ_E.

With the correct energy dependence of L/ξ_0 it is possible to calculate average total and spin transmission of graphene zigzag nanoribbons as a function of V_{tilt}, σ_E and E_F. The numerical values imply that σ_E is approximately given by the disorder strength V_{dis} divided by 2. The energy range of the magnetic clusters, $[E_{\mathrm{low}}, E_{\mathrm{high}}]$, depends on next-nearest neighbor hopping and the strength of the magnetization in the clusters. We chose the interval as $[-0.1t, 0]$. The relation between E_F and L/ξ_0 can be taken as an exponential,

$$|E_F| = 0.4\mathrm{e}^{-0.6L/\xi_0}. \tag{10.20}$$

With all these ingredients an expectation for $\langle T \rangle$ and $\langle T_S \rangle$ can be calculated as shown in Fig. 10.4 (black solid line). For comparison, also numerical results are plotted. The model presented here predicts the positions of the peaks in the spin transmission very well, the size of the spin transmission agrees approximately as well. The asymmetry is given by the different extensions of the magnetic clusters for the electron and hole bands within the numerics. This is not included in the simple analytic model. Notably, the spin conductance rises to $0.15e^2/h$ for clean edges. Edge disorder, however, randomizes magnetic moments along the edges (see inset of Fig. 10.4) and restores the balance of magnetic moments, leading to a suppressed spin transmission for sufficiently large amount of edge disorder ($\approx 10\%$).

10.4. Summary

We used the phenomenological model of edge magnetization developed in chapter 9 which has to be put in contrast to the full treatment of interaction [123, 134]. A careful justification has been done in chapter 9. Notably, a similar approach has been chosen in Refs. [129, 124]. In comparison to a more complex treatment, multi-particle treatment or mean-field approximation, the model enables us to efficiently calculate charge an spin transmission in graphene nanoribbons for a wide range of parameters.

In the calculated spin transmission, we clearly see signatures of edge magnetization despite the presence of potential fluctuations. In particular, we found that spin conductance fluctuations follow universal predictions for localized transport from the DMPK equations. Edge roughness, however, should not exceed 10% in order to preserve these features. Using the DMPK equations we showed that *zz* edge magnetization can be used to control spin conductance and, in turn, to polarize an originally unpolarized current.

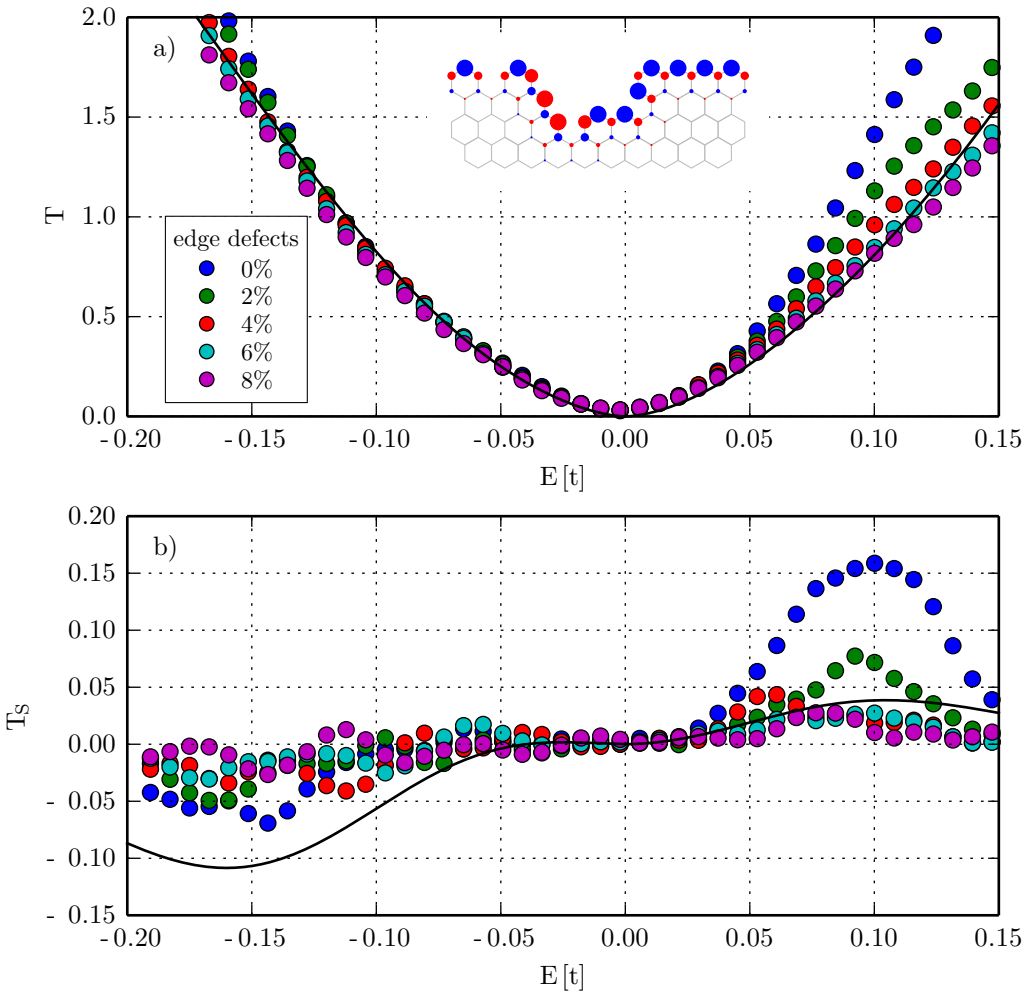

Figure 10.4.: Transport through graphene nanoribbons subject to a transverse in-plane electric field. a) Charge transmission as a function of Fermi energy for different amounts of edge roughness. The inset shows a sketch of the local magnetization close to an edge defect. Blue (red) circle indicate positive (negative) magnetization, the circle diameter is proportional to the size of the local magnetic moment. b) Spin transmission as a function of energy at the same amounts of edge defects as in figure a). The solid black lines are the average transmission $\langle T \rangle$ and spin transmission $\langle T_S \rangle$ calculated from Eqs. (10.15) and (10.16) with the number of magnetic clusters determined as sketched in the text.

11. Conclusions and perspectives

Due to its special bandstructure it is possible to approximate the electronic Hamiltonian of graphene within an effective description where the relevant degrees of freedom are the electron's momentum, its spin and the so-called pseudospin which is a remnant of the honeycomb lattice used to describe graphene. If the real spin is decoupled from the other degrees of freedom, the effective description resembles the Dirac equation of massless fermions with the pseudospin assuming the role of the real spin. Consequently, the real spin is conserved.

The decoupling has been justified by the vanishing nuclear spin in carbon atoms and a negligible atomic spin-orbit interaction [65, 41, 67]. Since spin transport experiments yielded high spin relaxation rates [76, 147] and the existence of magnetism in graphene has been confirmed [34, 130, 141, 142], it turned out that spin cannot be neglected in the electronic Hamiltonian of graphene.

In this thesis we investigated two different examples of how quantum transport is influenced when considering the inclusion of spin-dependent terms in the Hamiltonian. The first example is the investigation of spin relaxation in graphene. We highlighted different sources and mechanisms of spin relaxation and, eventually, showed the dominant role of resonant scatterers. The second example is the appearance of magnetically polarized states at the Fermi level close to zigzag edges. We showed that it manifests in universal spin conductance fluctuations and under which circumstances it leads to a finite spin conductance.

11.1. Spin relaxation in graphene

The first part of this thesis is dedicated to spin relaxation in graphene. We performed numerical simulations of spin transport in various scenarios. This was done with the aim of understanding the nature of spin relaxation which showed a surprisingly high rate in experiments in graphene [76, 147]

In chapter 5 we studied the Dyakonov-Perel (DP) and the Elliot-Yafet (EY) mechanism. In accordance with existing literature [85, 86] we found that both mechanisms can be excluded from considerations about the dominant spin relaxation mechanism. The resulting spin relaxation time, τ_S, we calculated, is several orders larger than in all experiments.

Besides the pure number τ_S we found anisotropic spin relaxation which differs between DP and EY spin relaxation. The obtained ratio between out-of-plane and in-plane spin relaxation is exactly 2 for the DP mechanism in a wide parameter range and it is nearly unaffected from the size of the intrinsic SOC, Δ_{SO}. This is different in the EY scenario where in-plane spin relaxation is strongly affected from the intrinsic SOC while out-of-plane spin relaxation is insensitive to Δ_{SO}. Hence, besides the linear

relation between momentum scattering time τ_p and the spin relaxation time τ_S, we have a second tool at hand to classify spin relaxation, and we used this *controllable anisotropy* in the later discussion of spin relaxation.

In chapter 6 we switched to a position dependent spin-orbit coupling which is supposed to be created by covalently bound adatoms [40, 96, 95]. Such a spin-orbit disorder acts as an additional source of spin relaxation because the amount of spin rotation explicitly depends on the propagation path of the electron. This so-called Sherman mechanism was, for graphene, first investigated with respect to surface ripples as the cause of the position dependence of the spin-orbit interactions [87]. Later studies, which assumed adatoms to be responsible for the position dependence of the spin-orbit coupling, stated that this is the dominant spin relaxation mechanism in graphene [39].

We performed a careful analysis both analytically and numerically and confirmed that the adatom-induced Sherman mechanism can lead to very fast spin relaxation in graphene. We also pointed out that there exists a strong resemblance to the EY mechanism rather than to the DP mechanism and an experimental distinction would be difficult. The obtained large spin relaxation rate requires, however, one out of thousand carbon atoms to be involved in a covalent bond with an adatom. Without artificial adatom deposition, a significantly lower adatom coverage is expected. We, hence, rejected this model as an explanation for the spin transport experiments in graphene.

In chapter 7 we replaced the simplified model of adsorbed adatoms used in chapter 6 by a more realistic extended tight-binding model following ideas laid out in Refs. [33, 95, 42, 43]. Using this model, we calculated the (local) density of states, charge and spin transport in hydrogenated and fluorinated graphene.

In both cases the adatoms lead to a characteristic energy dependence of the calculated quantities which is a notable difference to the simple model of spin-orbit disorder used in chapter 6. Nevertheless, a strongly increased spin-orbit coupling is induced by hydrogen as well as fluorine adatoms. We found, however, that, for spin relaxation, spin-orbit coupling is of minor importance. The spin relaxation rates obtained from the extended tight-binding model (ignoring the formation of magnetic moments) are comparable to the ones from the simplified model and, thus, much lower than in the experimental samples.

Eventually, in chapter 7, we also included the formation of magnetic moments around hydrogen adatoms and thoroughly examined their effect on spin transport. The density of states of hydrogenated graphene shows a narrow peak close to charge neutrality which originates from the impurity state forming around the adatoms. Our calculations show that close to this energy spin is relaxing very fast. The magnetic moments are large enough to significantly rotate the spin while an electron stays in an impurity state. Modifying the tight-binding parameters allowed us to confirm the importance of the elongated lifetime of the resonant state. Moreover, we identified a critical magnetization induced from the adatoms where a crossover to resonant spin scattering happens. Below that value spin relaxation can be obtained from Fermi's Golden rule and follow a simple power law, above the threshold value the spin relaxation rate saturates.

In conclusion, we substantiated that scattering from resonant magnetic impurities is the strongest source of spin relaxation found until now and the most promising candidate to explain why in experiments the spin signal is decaying so fast.

11.2. Zigzag edge magnetism

In the second part of the thesis we focused on the intrinsic magnetization of zigzag (zz) edges. Close to the Fermi level zz edges are expected to be magnetically polarized due to electron-electron interactions [35]. This phenomenon has been studied only theoretically until now, an experimental evidence is still missing. An obstacle for the experimental investigation can be the purity of the graphene samples both with respect to edge defects and potential fluctuations, which has previously been required from theoretical proposals [123, 134, 129]. In our investigations of transport in graphene nanoribbons we found universal signatures of the spin conductance originating from edge magnetization which is also present in disordered systems.

To this end, we dedicated chapter 9 to a thorough investigation of graphene in the presence of electron-electron interactions in Hartree-Fock approximation. We, additionally, included potential changes: p-n and p-n-p junctions as well as completely randomized disorder potentials. In all cases magnetic moments are forming near zz edges when the local doping is close to charge neutrality.

For the calculation of transport properties in chapter 10 we used a phenomenological model based on the results of chapter 9 in which we assumed the formation of clusters of magnetic moments wherever charge neutrality lines and zz edges coincide. The use of the phenomenological model reduces computational costs and allowed us to investigate transport for many parameters. To account for the shortcomings of our model different relative orientations of the magnetic clusters were considered.

In the localized transport regime, all considered models exhibit spin conductance fluctuations that obey universal predictions from the Dhorokov-Mello-Pereyra-Kumar (DMPK) equations [135, 136]. We made use of the DMPK equations to predict a finite spin conductance which results from the application of either a small magnetic field or a transverse in-plane electric field, and we confirmed this prediction by numerical calculations. Notably, edge defect rate may not exceed 10% while potential fluctuations are actually required in our analysis.

This controllable spin conductance can be used to either switch nanoribbons from "off" to "on" states (transistor action) or might be the basis for the all-electronic creation of a spin-polarized current which would open the route to all-graphene-based spintronics.

11.3. Perspectives

In this thesis we examined two conceptually different aspects of spin transport physics in graphene and graphene nanostructures. A common conclusion is that graphene possesses a high potential for spintronics research and applications. But the eventual realization is accompanied by certain demands on the quality of the used graphene samples.

A crucial point is the purity of the graphene lattice itself. Vacancies, which induce magnetic moments, should not be present. Similarly the edges should be sharp on an atomic level. Moreover, a lattice of purely sp^2 hybridized carbon atoms is desired which implies the avoidance of covalently bound impurities. These are the aspects, spin transport is most sensitive to, and we showed in this thesis that they significantly lower spin relaxation time and, potentially, mask the effects of the *zz* edge magnetism.

In the last years the fabrication of graphene nanostructures with well-defined edges made large progress [148, 149, 150, 151, 152, 153]. Hence, an experimental investigation of zigzag edges in the near future seems feasible. It remains an open issue how to control the presence of adatoms. An interesting route to isolate graphene from surface impurities is the use of turbostratic multilayer graphene [154]. However, a combination with an investigation of zigzag edge magnetism is not possible since nanostructuring of turbostratic graphene would naturally result in different terminations of the single layers.

Apart from the experimental implications from our findings, there are several closely related issues to be examined theoretically. Concerning the influence of adatoms, it is not yet fully understood how the size of the magnetic moments enters the spin relaxation length when both scattering from the adatoms and the slowly varying background disorder is involved. Moreover, the spin relaxation rate is linear in the number of adatoms up to a concentration of 10^{-3}. Above this value, we observed deviations from the linear relation whose origin is not yet revealed. Eventually, adatoms in confined systems can be investigated an, with the tools developed in this thesis, their interplay with edges, in particular zigzag edges, is worth being studied.

Part III.

Appendix

A. Recursive Green's function formalism

This chapter summarizes the recursive Green's function (RGF) method utilized in this thesis. In this form it has been implemented by Wimmer [56, 52] relying on previous works by MacKinnon [55].

Constructing the Green's function. Instead of a direct calculation of the Green's function it is constructed slice by slice. MacKinnon used a system discretized by square grid with parallel leads [55] and Wimmer eventually extended the algorithm to arbitrary grids with leads not necessarily parallel by using graph theory for an optimal partitioning of the grid [56].

The RGF method is based on a block-tridiagonalization of the Hamiltonian,

$$\mathcal{H} = \begin{pmatrix} \ddots & & & & \\ & \mathcal{H}_{i-1,i-1} & \mathcal{H}_{i-1,i} & 0 & \\ & \mathcal{H}_{i,i-1} & \mathcal{H}_{i,i} & \mathcal{H}_{i,i+1} & \\ & 0 & \mathcal{H}_{i+1,i} & \mathcal{H}_{i+1,i+1} & \\ & & & & \ddots \end{pmatrix}. \tag{A.1}$$

The Hamiltonian consists of blocks $\mathcal{H}_{j,j}$ representing isolated slices. Blocks i and j are connected by the hopping matrices $\mathcal{H}_{i,j}$ and $\mathcal{H}_{j,i}$. The construction of the Green's function makes use of the Dyson equation

$$G = G_0 + G_0 V G, \tag{A.2}$$

where the role of the perturbation V is taken by the hopping matrices.

Assume that the Green's function has been constructed up to slice i. We know the full *unperturbed* retarded Green's function $G_0^{r,i}$ which contains the Green's function for all blocks $\leq i-1$ and the isolated block i,

$$G_{0,j,k}^{r,i} = \begin{cases} G_{j,k}^{r,i} & \forall j,k < i, \\ (E - \mathcal{H}_{i,i} + \mathrm{i}\eta)^{-1} & j = k = i, \\ 0 & \text{otherwise.} \end{cases} \tag{A.3}$$

The perturbation is given by

$$V = \begin{pmatrix} \ddots & & & \\ & 0 & \mathcal{H}_{i-1,i} & \\ & \mathcal{H}_{i,i-1} & 0 & \\ & & & \ddots \end{pmatrix} \tag{A.4}$$

The Dyson equation tells us

$$G^{i+1}_{i+1,i+1} = (E - \mathcal{H}_{i,i} + \mathrm{i}\eta)^{-1} + (E - \mathcal{H}_{i,i} + \mathrm{i}\eta)^{-1}\mathcal{H}_{i+1,i}G^{i+1}_{i,i+1}, \tag{A.5}$$

$$G^{i+1}_{i,i+1} = G^{i}_{i,i}\mathcal{H}_{i,i+1}G^{i+1}_{i+1,i+1}. \tag{A.6}$$

From there we arrive at

$$G^{i+1}_{i+1,i+1} = [E - \mathcal{H}_{i,i} - \mathcal{H}_{i+1,i}G^{i}_{i,i}\mathcal{H}_{i,i+1}]^{-1}. \tag{A.7}$$

Similarly we can calculate $G^{i+1}_{0,i+1}$ and $G^{i+1}_{i+1,0}$.

With this algorithm it is possible to calculate the Green's function of an open system starting from the surface Green's function of one lead, $G^0_{0,0} = g^r_1$. The iteration continues to the last slice N. The connection to the second lead again makes use of the Dyson equation with the coupling between scattering region and lead as the perturbation term V and the surface Green's function of the second lead, g^r_2, replacing the isolated slice. The obtained matrices can, then, be used to calculate the transmission matrix via the Fisher-Lee relation.

The Green's function for $\mathbf{T}(\mathbf{L})$. In the context of this manuscript we are particularly interested in calculating the transmission as a function of system length. The RGF method allows for an easy access to this quantity when calculating the transmission for nanoribbons. The partitioning of nanoribbons produces slices parallel to the surface of the leads which are formed by rectangles with a well-defined distance from the lead.

We follow the procedure outlined in the previous curse of this chapter to calculate the Green's function. Let the total system length be L, then we want know the transmission at fractions $\{L_\alpha\}$ of this length. Whenever the distance L_{i_0} between slice i_0 and the lead opening coincides with one of the desired lengths L_α we interrupt the RGF iteration. Instead of continuing the iteration with the subsequent slice $i_0 + 1$ we attach the second lead by it surface Green's function and calculate the resulting total Green's function to obtain transmission, $T(L_{i_0})$. The value is stored and, afterwards, iteration is resumed from G^{r,i_0}. We repeat this procedure until all values $\{L_\alpha\}$ are covered.

The advantage of this procedure is its increase of calculation speed. Inverting a $N \times N$ matrix involves $\mathcal{O}(N)$ floating point operations. Consider systems with M slices consisting of N lattice sites. The direct calculation of the Green's function would involve $\mathcal{O}[(N \times M)^3]$ operations. The RGF algorithm reduces this number already to $M \times \mathcal{O}[N^3]$ operations. Calculating transmissions for individual systems of different lengths and, hence, different numbers of slices approximately scales as $\mathcal{O}[N^3]\sum_\alpha M_\alpha$, where M_α is the number of slices necessary to calculate the transmission at $L = L_\alpha$. So, calculating the transmission for many values L_α approximately would scale as $M^2 \times \mathcal{O}[N^3]$. With this optimized procedure calculation time is only slightly increased with respect to the single RGF scaling, $M \times \mathcal{O}[N^3]$.

B. Interactions

This chapter is intended for presenting the self-consistent algorithm for the calculation of electron and spin density used in chapter 9. Although covered in standard textbooks on solid state physics (e. g. [155]) we shortly repeat the derivation of the Hartree-Fock Hubbard Hamiltonian used within the calculation scheme to fix the used notation. In sections B.1 – B.3 we present the Hamiltonian starting from the general formulation in Fock space, mapping it onto a localized Wannier basis and, eventually deriving the mean-field approximation of the Hamiltonian. The calculation scheme used is presented in section B.4.

B.1. Interacting Hamiltonian in second quantization for uncorrelated electrons

We assume a Hamiltonian $\mathcal{H}$, describing N identical fermions. The Hamiltonian consists of a single-particle term $\mathcal{H}_1$ and a term describing two-particle interactions $\mathcal{H}_2$. We write

$$\mathcal{H} = \mathcal{H}_1 + \mathcal{H}_2 \tag{B.1}$$

$$\mathcal{H}_1 = \sum_{i=1}^{N} h(x_i, p_i) \tag{B.2}$$

$$\mathcal{H}_2 = \frac{1}{2} \sum_{\substack{i,j=1 \\ i \neq j}}^{N} V(x_i, x_j, p_i, p_j) \tag{B.3}$$

Particles, obeying the single-particle hamiltonian h, may be described by a set of quantum numbers α, e. g. $\alpha = \{k, \sigma\}$ momentum and spin. We use this general form in the following when not addressing a particular problem. So for the identity in the subspace of the i-th particle we get $I_i = \sum_\alpha |\alpha\rangle^{ii}\langle\alpha|$.

As a first approximation we neglect correlations between particles and express our multi-particle wavefunction as a product of single-particle wavefunctions. The Slater-determinant is a good candidate for such a wavefunction as it already incorporates the correct particle exchange properties for fermions. With this approximation we can express $\mathcal{H}_1$ and $\mathcal{H}_2$ with the help of the single-particle wavefunctions,

$$\begin{aligned} \mathcal{H}_1 &= \sum_{i=1}^{N} \sum_{\alpha,\beta} |\alpha\rangle^{ii}\langle\alpha|h_i|\beta\rangle^{ii}\langle\beta| \\ &= \sum_{i=1}^{N} \sum_{\alpha,\beta} h_{\alpha,\beta}|\alpha\rangle^{ii}\langle\beta| = \sum_{\alpha,\beta} h_{\alpha,\beta} c_\alpha^\dagger c_\beta. \end{aligned} \tag{B.4}$$

Due to orthogonality $\sum_{i=1}^{N} |\alpha\rangle^{ii}\langle\beta|$ removes a state $|\beta\rangle$ and replaces it with a state $|\alpha\rangle$ which is the same what also the creation and annihilation operators $c_\alpha^\dagger c_\beta$ do. Similarly, we obtain for the two-particle Hamiltonian:

$$\begin{aligned}\mathcal{H}_2 &= \frac{1}{2}\sum_{\substack{i,j=1\\ i\neq j}}^{N}\sum_{\alpha,\beta,\gamma,\delta} |\alpha\rangle^i|\beta\rangle^{jj}\langle\beta|^i\langle\alpha|V(x_i,x_j,p_i,p_j)|\gamma\rangle^j|\delta\rangle^{ii}\langle\delta|^j\langle\gamma| \\ &= \frac{1}{2}\sum_{\alpha,\beta,\gamma,\delta} V_{\alpha,\beta,\gamma,\delta} c_\alpha^\dagger c_\beta^\dagger c_\gamma c_\delta .\end{aligned} \tag{B.5}$$

B.2. Interacting Hamiltonian on a Discrete lattice

On a discrete lattice we use Wannier states for the description of the electrons. Wannier states belong to an electronic band n and are localized around the position $\boldsymbol{R}$ of a lattice point usually defined by the atoms' positions. Together with the spin σ these numbers form the set of quantum numbers α in the Wannier basis. Often, instead of the atomic position $\boldsymbol{R}$ the index of the lattice site i is chosen. In the single-band approximation the quantum number n is omitted and no excited states are taken into account.

Write the "default" solid state electronic hamiltonian with Coulomb interaction in Wannier basis:

$$\begin{aligned}\mathcal{H} =& \sum_{\sigma,\sigma'}\sum_{\boldsymbol{R},\boldsymbol{R}'} t_{\boldsymbol{R},\boldsymbol{R}'}^{\sigma,\sigma'} c_{\sigma,\boldsymbol{R}}^\dagger c_{\sigma',\boldsymbol{R}'} + \\ &+ \frac{1}{2}\sum_{\sigma_1\sigma_2\sigma_3\sigma_4}\sum_{\boldsymbol{R}_1\boldsymbol{R}_2\boldsymbol{R}_3\boldsymbol{R}_4} V_{\boldsymbol{R}_1\boldsymbol{R}_2,\boldsymbol{R}_2\boldsymbol{R}_4}^{\sigma_1\sigma_2,\sigma_3\sigma_4} c_{\sigma_1,\boldsymbol{R}_1}^\dagger c_{\sigma_2,\boldsymbol{R}_2}^\dagger c_{\sigma_3,\boldsymbol{R}_3} c_{\sigma_4,\boldsymbol{R}_4}\end{aligned} \tag{B.6}$$

Spin conservation is assumed for the interaction, which can formally be expressed by $V_{\boldsymbol{R}_1\boldsymbol{R}_2,\boldsymbol{R}_2\boldsymbol{R}_4}^{\sigma_1\sigma_2,\sigma_3\sigma_4} = V_{\boldsymbol{R}_1\boldsymbol{R}_2,\boldsymbol{R}_2\boldsymbol{R}_4}^{\sigma_1\sigma_2}\delta_{\sigma_1\sigma_4}\delta_{\sigma_2\sigma_3}$. This helps to carry out the σ_3 and σ_4 summation. After renaming σ_1 and σ_2 to σ and σ' the Hamiltonian reads:

$$\begin{aligned}\mathcal{H} =& \sum_{\sigma,\sigma'}\sum_{\boldsymbol{R},\boldsymbol{R}'} t_{\boldsymbol{R},\boldsymbol{R}'}^{\sigma,\sigma'} c_{\sigma,\boldsymbol{R}}^\dagger c_{\sigma',\boldsymbol{R}'} + \\ &+ \frac{1}{2}\sum_{\sigma,\sigma'}\sum_{\boldsymbol{R}_1\boldsymbol{R}_2\boldsymbol{R}_3\boldsymbol{R}_4} V_{\boldsymbol{R}_1\boldsymbol{R}_2,\boldsymbol{R}_2\boldsymbol{R}_4}^{\sigma,\sigma'} c_{\sigma,\boldsymbol{R}_1}^\dagger c_{\sigma',\boldsymbol{R}_2}^\dagger c_{\sigma',\boldsymbol{R}_3} c_{\sigma,\boldsymbol{R}_4} .\end{aligned} \tag{B.7}$$

Under the assumption that only diagonal elements of $V_{\boldsymbol{R}_1\boldsymbol{R}_2,\boldsymbol{R}_2\boldsymbol{R}_4}^{\sigma,\sigma'}$ contribute to the Hamiltonian[1] the Hamiltonian can be written as

$$\begin{aligned}\mathcal{H} =& \sum_{\sigma,\sigma'}\sum_{\boldsymbol{R},\boldsymbol{R}'} t_{\boldsymbol{R},\boldsymbol{R}'}^{\sigma,\sigma'} c_{\sigma,\boldsymbol{R}}^\dagger c_{\sigma',\boldsymbol{R}'} + \\ &+ \frac{1}{2}\sum_{\sigma,\sigma'}\sum_{\boldsymbol{R}} V_{\boldsymbol{R}}^{\sigma,\sigma'} c_{\sigma,\boldsymbol{R}_1}^\dagger c_{\sigma',\boldsymbol{R}_2}^\dagger c_{\sigma',\boldsymbol{R}_3} c_{\sigma,\boldsymbol{R}_4} .\end{aligned} \tag{B.8}$$

[1] diagonal in position space, i. e. only *local* interactions but still, possibly, between opposite spins

Due to Pauli exclusion only electrons of opposite spin can occupy a state located at the same lattice site within the single-band approximation. The interaction potential further simplifies to

$$V_{\boldsymbol{R}}^{\sigma,\sigma'} = \begin{cases} 0 & \sigma = \sigma' \\ V_{\boldsymbol{R}} & \sigma = -\sigma' \end{cases}. \tag{B.9}$$

Since the Coulomb interaction in a constant dielectric does not depend on the position a further simplification of the Hamiltonian is the removal of the position dependence of the interaction strength $V_{\boldsymbol{R}} \to U$. With this and fermion anti-commutation[2] relations the very compact version of the interacting Hamiltonian, the Hubbard hamiltonian, reads:

$$\mathcal{H} = \sum_{\sigma,\sigma'} \sum_{\boldsymbol{R},\boldsymbol{R}'} t_{\boldsymbol{R},\boldsymbol{R}'}^{\sigma,\sigma'} c_{\sigma,\boldsymbol{R}}^{\dagger} c_{\sigma',\boldsymbol{R}'} + U \sum_{\boldsymbol{R}} c_{\uparrow,\boldsymbol{R}}^{\dagger} c_{\uparrow,\boldsymbol{R}} c_{\downarrow,\boldsymbol{R}}^{\dagger} c_{\downarrow,\boldsymbol{R}} \tag{B.10}$$

Sometimes also the extended Hubbard model is mentioned which is an extension of the Hubbard model taking into account also nearest neighbor interactions. The investigation of the magnetic edge of graphene zigzag nanoribbons was performed both with the simple as well as with the extended Hubbard model. The original work on the magnetic zigzag edge state in graphene, Ref. [35], uses the simple Hubbard model. In 2003 the calculation was repeated within the extended Hubbard model [122]. There it is found that the nearest neighbor interaction can turn the spin-polarized state into a charge-polarized state when the next-nearest neighbor interaction exceeds the local interaction strength. We stick to the simple Hubbard model for the investigation of the spin-polarized nanoribbons which are not qualitatively changed by the extension of the Hubbard Hamiltonian.

B.3. Hubbard model in Hartree-Fock approximation

To facilitate a numerical treatment we approximate the interacting Hamiltonian by a single particle Hamiltonian. This can be achieved by the Hartee-Fock approximation. We want to obtain a Hamiltonian of the form

$$\tilde{\mathcal{H}} = \sum_{\alpha,\beta} x_{\alpha,\beta} c_{\alpha}^{\dagger} c_{\beta}, \tag{B.11}$$

or, written explicitly with quantum numbers used in the preceding section

$$\tilde{\mathcal{H}} = \sum_{\sigma,\sigma'} \sum_{\boldsymbol{R},\boldsymbol{R}'} x_{\boldsymbol{R},\boldsymbol{R}'}^{\sigma,\sigma'} c_{\sigma,\boldsymbol{R}}^{\dagger} c_{\sigma',\boldsymbol{R}'}. \tag{B.12}$$

There is no exact mapping, we only can approximate the effective Hamiltonian and do this with help af minimalizing the corresponding grand-canonical potentials. The grand-canonical potential is defined by the grand-canonical partition function as

$$\Phi_{GK} = -k_B T \ln Z_{GK} = -k_B T \ln \mathrm{Tr}[\mathrm{e}^{-\beta(\mathcal{H}-\mu N)}] \tag{B.13}$$

[2] $\{c_\alpha, c_\beta\} = 0 = \{c_\alpha^\dagger, c_\beta^\dagger\}$, $\{c_\alpha^\dagger, c_\beta\} = \delta_{\alpha,\beta}$

with the grand-canonical partition function

$$Z = \mathrm{Tr}[\mathrm{e}^{-\beta(\mathcal{H}-\mu N)}] \tag{B.14}$$

and the grand-canonical density operator is

$$\rho_{GK} = \frac{1}{Z_{GK}}\mathrm{e}^{-\beta(\mathcal{H}-\mu N)}. \tag{B.15}$$

Defining a functional $\mathcal{F}[\rho] := \mathrm{Tr}[\rho(\mathcal{H} - \mu N + k_B T \ln \rho)]$ it appears that

$$\mathcal{F}[\rho_{GK}] = \Phi_{GK} \tag{B.16}$$

For an arbitrary density operator $\mathcal{F}[\rho] > \mathcal{F}[\rho_{GK}]$.Hence, we calculate the density operator $\tilde{\rho}$ of our effective Hamiltonian $\tilde{\mathcal{H}}$.

$$\tilde{Z} = \mathrm{Tr}[\mathrm{e}^{-\beta(\tilde{\mathcal{H}}-\mu N)}], \tag{B.17}$$

$$\tilde{\rho} = \frac{1}{\tilde{Z}}\mathrm{e}^{-\beta(\tilde{H}-\mu N)}, \tag{B.18}$$

$$\tilde{\Phi} = -k_B T \ln \tilde{Z}, \tag{B.19}$$

and minimize $\mathcal{F}[\tilde{\rho}]$ by variation of the $x^{\sigma,\sigma'}_{\boldsymbol{R},\boldsymbol{R}'}$ in order to obtain an approximation to the original potential.

$$\begin{aligned}
\mathcal{F}[\tilde{\rho}] =& \mathrm{Tr}[\tilde{\rho}(\mathcal{H} - \mu N + k_B T \ln \tilde{\rho})] = \\
=& \mathrm{Tr}[\tilde{\rho}(\mathcal{H} - \mu N - (\tilde{\mathcal{H}} - \mu N) - k_B T \ln \tilde{Z})] = \\
=& \mathrm{Tr}[\tilde{\rho}(\mathcal{H} - \tilde{\mathcal{H}})] - k_B T \ln \tilde{Z} = \\
=& \langle \mathcal{H} - \tilde{\mathcal{H}} \rangle_{\mathrm{eff}} + \tilde{\Phi}
\end{aligned} \tag{B.20}$$

Here $\langle A \rangle_{\mathrm{eff}} = \frac{1}{\tilde{Z}} \mathrm{Tr}[\mathrm{e}^{-\beta(\tilde{\mathcal{H}}-\mu N)} A]$ as the average with respect to the single-particle Hamiltonian $\tilde{\mathcal{H}}$. With the explicit forms of $\mathcal{H}$ and $\tilde{\mathcal{H}}$ we obtain

$$\begin{aligned}
\mathcal{F}[\tilde{\rho}] =& \langle \textstyle\sum_{\sigma,\sigma'} \sum_{\boldsymbol{R},\boldsymbol{R}'} (x^{\sigma,\sigma'}_{\boldsymbol{R},\boldsymbol{R}'} - t^{\sigma,\sigma'}_{\boldsymbol{R},\boldsymbol{R}'}) c^\dagger_{\sigma,\boldsymbol{R}} c_{\sigma',\boldsymbol{R}'} + U \sum_{\boldsymbol{R}} c^\dagger_{\uparrow,\boldsymbol{R}} c_{\uparrow,\boldsymbol{R}} c^\dagger_{\downarrow,\boldsymbol{R}} c_{\downarrow,\boldsymbol{R}} \rangle_{\mathrm{eff}} + \tilde{\Phi} = \\
=& \sum_{\sigma,\sigma'} \sum_{\boldsymbol{R},\boldsymbol{R}'} (t^{\sigma,\sigma'}_{\boldsymbol{R},\boldsymbol{R}'} - x^{\sigma,\sigma'}_{\boldsymbol{R},\boldsymbol{R}'}) \langle c^\dagger_{\sigma,\boldsymbol{R}} c_{\sigma',\boldsymbol{R}'} \rangle_{\mathrm{eff}} + U \sum_{\boldsymbol{R}} \langle c^\dagger_{\uparrow,\boldsymbol{R}} c_{\uparrow,\boldsymbol{R}} c^\dagger_{\downarrow,\boldsymbol{R}} c_{\downarrow,\boldsymbol{R}} \rangle_{\mathrm{eff}} + \tilde{\Phi}
\end{aligned} \tag{B.21}$$

The two-particle correlator $\langle c^\dagger_{\uparrow,\boldsymbol{R}} c_{\uparrow,\boldsymbol{R}} c^\dagger_{\downarrow,\boldsymbol{R}} c_{\downarrow,\boldsymbol{R}}\rangle_{\text{eff}}$ needs to be simplified which is possible as the average is calculated with respect to a non-interacting Hamiltonian.[3] We obtain

$$\begin{aligned}\mathcal{F}[\tilde{\rho}] =& \sum_{\sigma,\sigma'}\sum_{\boldsymbol{R},\boldsymbol{R}'}(t^{\sigma,\sigma'}_{\boldsymbol{R},\boldsymbol{R}'} - x^{\sigma,\sigma'}_{\boldsymbol{R},\boldsymbol{R}'})\langle c^\dagger_{\sigma,\boldsymbol{R}} c_{\sigma',\boldsymbol{R}'}\rangle_{\text{eff}} \\ &+ U\sum_{\boldsymbol{R}}\langle c^\dagger_{\uparrow,R} c_{\uparrow,R}\rangle_{\text{eff}}\langle c^\dagger_{\downarrow,R} c_{\downarrow,R}\rangle_{\text{eff}} + \tilde{\Phi}.\end{aligned} \tag{B.24}$$

The functional $\mathcal{F}[\tilde{\rho}]$ is to be minimized with respect to $x^{\sigma,\sigma'}_{R,R'}$. The minima fulfill

$$\begin{aligned}0 =& \sum_{\sigma,\sigma'}\sum_{\boldsymbol{R},\boldsymbol{R}'}\frac{\partial}{\partial x^{\sigma,\sigma'}_{R,R'}}\langle c^\dagger_{\sigma,\boldsymbol{R}} c_{\sigma',\boldsymbol{R}'}\rangle_{\text{eff}}\times \\ &\times\left[(t^{\sigma,\sigma'}_{\boldsymbol{R},\boldsymbol{R}'} - x^{\sigma,\sigma'}_{\boldsymbol{R},\boldsymbol{R}'}) + U\langle c^\dagger_{\downarrow,R} c_{\downarrow,R}\rangle_{\text{eff}}\delta_{\boldsymbol{R}\boldsymbol{R}'}\delta_{\sigma\uparrow} + U\langle c^\dagger_{\uparrow,R} c_{\uparrow,R}\rangle_{\text{eff}}\delta_{\boldsymbol{R}\boldsymbol{R}'}\delta_{\sigma\downarrow}\right],\end{aligned} \tag{B.25}$$

where we made use of

$$\frac{\partial}{\partial x^{\sigma,\sigma'}_{R,R'}}\tilde{\Phi} = -k_B T\frac{1}{\tilde{Z}}\frac{\partial}{\partial x^{\sigma,\sigma'}_{R,R'}}Z = \frac{1}{\tilde{Z}}\,\text{Tr}\left[\mathrm{e}^{-\beta(\tilde{\mathcal{H}}-\mu N)} c^\dagger_{\sigma,\boldsymbol{R}} c_{\sigma',\boldsymbol{R}'}\right] = \langle c^\dagger_{\sigma,\boldsymbol{R}} c_{\sigma',\boldsymbol{R}'}\rangle_{\text{eff}}. \tag{B.26}$$

Equation (B.25) is fulfilled when

$$x^{\sigma,\sigma'}_{\boldsymbol{R},\boldsymbol{R}'} = t^{\sigma,\sigma'}_{\boldsymbol{R},\boldsymbol{R}'} + U\langle c^\dagger_{\downarrow,R} c_{\downarrow,R}\rangle_{\text{eff}}\delta_{\boldsymbol{R}\boldsymbol{R}'}\delta_{\sigma\uparrow} + U\langle c^\dagger_{\uparrow,R} c_{\uparrow,R}\rangle_{\text{eff}}\delta_{\boldsymbol{R}\boldsymbol{R}'}\delta_{\sigma\downarrow}. \tag{B.27}$$

So, the Hartee-Fock approximation of the Hubbard Hamiltonian is the sum of the non-interacting single-particle Hamiltonian and an effective interaction potential proportional to the spin-up and spin-down densities, $\langle n_{\uparrow(\downarrow)}\rangle = \langle c^\dagger_{\uparrow(\downarrow),R} c_{\uparrow(\downarrow),R}\rangle_{\text{eff}}$,

$$\begin{aligned}\mathcal{H} =& \sum_{\sigma,\sigma'}\sum_{\boldsymbol{R},\boldsymbol{R}'} t^{\sigma,\sigma'}_{\boldsymbol{R},\boldsymbol{R}'} c^\dagger_{\sigma,\boldsymbol{R}} c_{\sigma',\boldsymbol{R}'} + \\ &+ U\sum_{\boldsymbol{R}}\left(\langle n_\uparrow(\boldsymbol{R})\rangle c^\dagger_{\downarrow,R} c_{\downarrow,R} + \langle n_\downarrow(\boldsymbol{R})\rangle c^\dagger_{\uparrow,R} c_{\uparrow,R}\right)\end{aligned} \tag{B.28}$$

We calculate the densities in a self-consistent way presented in the next section.

[3] For non-interacting systems the Hamiltonian is a sum of single-particle operators acting on orthogonal subspaces and thus $\tilde{\rho}$ can be factorized into single-particle parts. The corresponding average becomes

$$\langle c^\dagger_\alpha c^\dagger_\beta c_\gamma c_\delta\rangle_{\text{eff}} = \langle c^\dagger_\alpha c_\delta\rangle_{\text{eff}}\delta_{\alpha\delta}\langle c^\dagger_\beta c_\gamma\rangle_{\text{eff}}\delta_{\beta\gamma} - \langle c^\dagger_\alpha c_\gamma\rangle_{\text{eff}}\delta_{\alpha\gamma}\langle c^\dagger_\beta c_\delta\rangle_{\text{eff}}\delta_{\beta\delta} \tag{B.22}$$

$$\langle c^\dagger_{\uparrow,R} c_{\uparrow,R} c^\dagger_{\downarrow,R} c_{\downarrow,R}\rangle_{\text{eff}} = \langle c^\dagger_{\uparrow,R} c_{\uparrow,R}\rangle_{\text{eff}}\langle c^\dagger_{\downarrow,R} c_{\downarrow,R}\rangle_{\text{eff}} \tag{B.23}$$

B.4. Calculation scheme

Electron density in equilibrium can be calculated by integrating the density of states over all energies and weighting with the Fermi distribution,

$$\langle n_\uparrow(\boldsymbol{r})\rangle = \int_{-\infty}^{\infty} f(E, E_F, k_B T) d_\uparrow(\boldsymbol{r}, E)\mathrm{d}E, \tag{B.29}$$

$$\langle n_\downarrow(\boldsymbol{r})\rangle = \int_{-\infty}^{\infty} f(E, E_F, k_B T) d_\downarrow(\boldsymbol{r}, E)\mathrm{d}E. \tag{B.30}$$

At $T = 0\mathrm{K}$ we replace the Fermi function by the Heaviside step function and get

$$\langle n_\uparrow(\boldsymbol{r})\rangle = \int_{-\infty}^{E_F} d_\uparrow(\boldsymbol{r}, E)\mathrm{d}E, \tag{B.31}$$

$$\langle n_\downarrow(\boldsymbol{r})\rangle = \int_{-\infty}^{E_F} d_\downarrow(\boldsymbol{r}, E)\mathrm{d}E. \tag{B.32}$$

With these preliminaries laid out, we can explain how the iteration scheme works. We define an initial electron distribution $\langle n^0_{\uparrow/\downarrow}\rangle$. To calculate $\langle n^i_{\uparrow/\downarrow}\rangle$ for $i > 0$ we follow these steps:

1. Using the Hamiltonian (B.28) with the interaction part obtained from $\langle n^{i-1}_{\uparrow/\downarrow}\rangle$ we calculate an intermediate density $\langle \tilde{n}^i_{\uparrow/\downarrow}\rangle$ from Eqs. (B.31) and (B.32). To deal with van-Hove singularities within the energy range $[-\infty, E_F]$ we shifted the energy by a small imaginary number.

2. To achieve a better convergence we included damping in the iteration process by taking a fraction Ω of the result of the last iteration step,

$$\langle n^i_{\uparrow/\downarrow}(\boldsymbol{r})\rangle = (1-\Omega)\langle \tilde{n}^i_{\uparrow/\downarrow}(\boldsymbol{r})\rangle + \Omega\langle n^{i-1}_{\uparrow/\downarrow}(\boldsymbol{r})\rangle. \tag{B.33}$$

3. The obtained densities are checked for self-consistency by comparing to the previous iteration step. Convergence is reached when the change of both spin-up and down density $\delta^{\mathrm{step}}_{\uparrow/\downarrow} = |\langle n^i_{\uparrow/\downarrow}\rangle - \langle n^{i-1}_{\uparrow/\downarrow}\rangle|^2$ is smaller than 10^{-5}. If this is the case, iteration ends. Otherwise we continue with the calculation of $\langle n^{i+1}_{\uparrow/\downarrow}\rangle$.

C. Sherman spin relaxation

C.1. Correlation function of Rashba disorder

From Ref. [40] an SO-parameter of the form,

$$\lambda(\boldsymbol{r}) = \sum_{i=0}^{N_{\text{imp}}} \lambda_i(\boldsymbol{r} - \boldsymbol{R}_i) = \sum_{i=0}^{N_{\text{imp}}} \lambda_{\text{SO}}^{at} A_0 \mathrm{e}^{-\frac{|\boldsymbol{r}-\boldsymbol{R}_i|}{\xi}} \sqrt{3\left(1 - A_0^2 \mathrm{e}^{-2\frac{|\boldsymbol{r}-\boldsymbol{R}_i|}{\xi}}\right)}, \tag{C.1}$$

is expected. This is similar to the Edwards model for static disorder [48, section 2.2.2]:

$$V(\boldsymbol{r}) = \sum_{i=1}^{N_{\text{imp}}} v(\boldsymbol{r} - \boldsymbol{r}_i).$$

The corresponding two-point correlator is

$$B(\boldsymbol{r} - \boldsymbol{r}') = n_i \int \mathrm{d}r'' \lambda_i(\boldsymbol{r}'' - \boldsymbol{r}) \lambda_i(\boldsymbol{r}'' - \boldsymbol{r}'), \tag{C.2}$$

where n_i is the adatom density. The Fourier transform $B(\boldsymbol{q})$ is the square of the Fourier transform of the potential induced by a single impurity sitting at the origin multiplied by the adatom density [48],

$$\begin{aligned} B(\boldsymbol{q}) &= n_i \lambda(\boldsymbol{q})^2, \\ \lambda(\boldsymbol{q}) &= \int \mathrm{d}\boldsymbol{r} \mathrm{e}^{-\mathrm{i}\boldsymbol{q}\cdot\boldsymbol{r}} \lambda(\boldsymbol{r}). \end{aligned}$$

We calculate:

$$\lambda(\boldsymbol{q}) = \int \mathrm{d}\boldsymbol{r} \mathrm{e}^{-\mathrm{i}\boldsymbol{q}\cdot\boldsymbol{r}} \lambda_{\text{SO}}^{at} A_0 \mathrm{e}^{-\frac{r}{\xi}} \sqrt{3(1 - A_0^2 \mathrm{e}^{-2\frac{r}{\xi}})}$$

In polar coordinates this can be written as

$$\lambda(\boldsymbol{q}) = \lambda_{S0}^{at} A_0 \int_0^{2\pi} \mathrm{d}\varphi \int_0^{\infty} \mathrm{d}r \left(r \mathrm{e}^{-\mathrm{i}qr\cos\varphi} \mathrm{e}^{-\frac{r}{\xi}} \sqrt{3(1 - A_0^2 \mathrm{e}^{-2\frac{r}{\xi}})} \right).$$

The only part depending on φ is

$$I = \int_0^{2\pi} \mathrm{e}^{-\mathrm{i}qr\cos\varphi} \mathrm{d}\varphi. \tag{C.3}$$

We can find a solution for this integral [156, section 3.195],

$$\int_0^\pi \mathrm{e}^{\mathrm{i}\beta\cos x}\cos nx\mathrm{d}x = \mathrm{i}^n\pi J_n(\beta) \tag{C.4}$$

where $J_n(\beta)$ is the Bessel function:

$$J_n(\beta) = \frac{\beta^n}{2^n}\sum_{k=0}^{\infty}(-1)^k\frac{\beta^{2k}}{2^{2k}k!\Gamma(n+k+1)} \tag{C.5}$$

We split the integration limits at $\varphi=\pi$ and substitute the integrand φ in the second summand by $\varphi-\pi$,

$$\begin{aligned}\int_0^{2\pi}\mathrm{e}^{-\mathrm{i}qr\cos\varphi}\mathrm{d}\varphi &= \int_0^{\pi}\mathrm{e}^{-\mathrm{i}qr\cos\varphi}\mathrm{d}\varphi + \int_\pi^{2\pi}\mathrm{e}^{-\mathrm{i}qr\cos\varphi}\mathrm{d}\varphi\\ = \pi J_0(-qr) + \int_0^{\pi}\mathrm{e}^{\mathrm{i}qr\cos\varphi}\mathrm{d}\varphi &= \pi J_0(-qr) + \pi J_0(qr) = 2\pi J_0(qr).\end{aligned}$$

For the integration we made use of equation (C.4). $J_0(x)$ is an even function of x allowing the summation in the last step. We end up with

$$I = \int_0^{2\pi}\mathrm{e}^{-\mathrm{i}qr\cos\varphi}\mathrm{d}\varphi = 2\pi J_0(qr), \tag{C.6}$$

and insert the solution of this integration in the original problem:

$$\lambda(\boldsymbol{q}) = \lambda_{S0}^{at}A_0\int_0^\infty \mathrm{d}r\left(r2\pi J_0(qr)\mathrm{e}^{-\frac{r}{\xi}}\sqrt{3(1-A_0^2\mathrm{e}^{-2\frac{r}{\xi}})}\right). \tag{C.7}$$

With the expression under the square root expanded as

$$\begin{aligned}\sqrt{1+x} &= \sum_{n=0}^{\infty}C_nx^n,\\ C_n &= \frac{(-1)^n(2n!)}{(1-2n)(n!)^2(4^n)},\end{aligned}$$

the integral simplifies to

$$\begin{aligned}\lambda(\boldsymbol{q}) &= \sum_{n=0}^{\infty}C_n\lambda_{S0}^{at}A_0\sqrt{3}\int_0^\infty \mathrm{d}r\left(r2\pi J_0(qr)\mathrm{e}^{-\frac{r}{\xi}}(-A_0^2)^n\mathrm{e}^{-2n\frac{r}{\xi}}\right)\\ &= \sum_{n=0}^{\infty}C_n(-A_0^2)^n2\pi\lambda_{S0}^{at}A_0\sqrt{3}\int_0^\infty \mathrm{d}r\left(J_0(qr)r\mathrm{e}^{-\frac{2n+1}{\xi}r}\right).\end{aligned}$$

We can again find a solution for the integral [156, section 6.621],

$$\begin{aligned}&\int_0^\infty \mathrm{e}^{-\alpha x}J_\nu(\beta x)x^{\mu-1}\mathrm{d}x\\ &= \frac{\left(\frac{\beta}{2\alpha}\right)^\nu\Gamma(\nu+\mu)}{\alpha^\mu\Gamma(\nu+1)}\left(1+\frac{\beta^2}{\alpha^2}\right)^{\frac{1}{2}-\mu}F\left(\frac{\nu-\mu+1}{2},\frac{\nu-\mu}{2}+1;\nu+1;-\frac{\beta^2}{\alpha^2}\right),\end{aligned} \tag{C.8}$$

where $F(\delta, \epsilon; \gamma; z)$ is the hypergeometric functions; in our case, we consider

$$\begin{aligned} \alpha =& \frac{2n+1}{\xi}, & \beta =& q, \\ \nu =& 0, & \mu =& 2, \end{aligned}$$

such that

$$\begin{aligned} \delta =& -\frac{1}{2}, & \epsilon =& 0, \\ \gamma =& 1, & z =& -\left(\frac{q\xi}{2n+1}\right)^2. \end{aligned}$$

As $\epsilon = 0$, the hypergeometric functions is 1. The prefactor further simplifies when plugging the parameters,

$$\frac{\left(\frac{\beta}{2\alpha}\right)^{\nu}\Gamma(\nu+\mu)}{\alpha^{\mu}\Gamma(\nu+1)}\left(1+\frac{\beta^2}{\alpha^2}\right)^{\frac{1}{2}-\mu} = \frac{\xi^2}{(1+2n)^2}\left[1+\left(\frac{q\xi}{1+2n}\right)^2\right]^{-\frac{3}{2}}.$$

The Fourier transform of the SOC now has the form

$$\begin{aligned} \lambda(\boldsymbol{q}) &= \sum_{n=0}^{\infty} C_n(-A_0^2)^n 2\pi\lambda_{S0}^{at}A_0\sqrt{3}\frac{\xi^2}{(1+2n)^2}\left[1+\left(\frac{q\xi}{1+2n}\right)^2\right]^{-\frac{3}{2}} \\ &= 2\pi\lambda_{\mathrm{SO}}^{at}A_0\sqrt{3}\xi^2\sum_{n=0}^{\infty}\frac{D_n(A_0)}{\left[1+(\frac{\xi}{1+2n})^2q^2\right]^{\frac{3}{2}}}, \\ \text{with } D_n(A_0) &= C_n\cdot\frac{(-1)^n(A_0^2)^n}{(1+2n)^2} = \frac{(2n)!(A_0^2)^n}{(1-2n)(1+2n)^2(n!)^2(4^n)}. \end{aligned}$$

Let us have a look at the coefficient $D_n(A_0)$:

$$\begin{aligned} D_0(A_0) &= 1 \\ D_1(A_0) &= -\frac{A_0^2}{36} \qquad \Rightarrow |D_1(A_0)| \leq D_0 \quad \forall\, |A_0| \leq 6 \\ \frac{D_n(A_0)}{D_{n-1}(A_o)} &= \frac{A_0^2}{4}\cdot\left(1-\frac{1}{n}\right)\cdot\left(1+\frac{2}{1-2n}\right)\cdot\left(1-\frac{2}{1+2n}\right)^2;\ \forall\, n \geq 2 \\ &\quad |\frac{A_0^2}{4}| < 1\ \forall\, |A_0| < 2 \\ &\quad \frac{1}{2} \leq \left(1-\frac{1}{n}\right) < 1 \\ &\quad \frac{1}{3} \leq \left(1+\frac{2}{1-2n}\right) < 1 \\ &\quad \frac{3}{5} \leq \left(1-\frac{2}{1+2n}\right) < 1 \end{aligned}$$

Thus, the coefficients $D_n(A_0)$ for $A_0 = \frac{1}{2}$ decay as n increases. We truncate $\lambda(\boldsymbol{q})$ at $n = 1$, obtaining

$$\lambda(\boldsymbol{q}) = 2\pi\lambda_{\mathrm{SO}}^{at} A_0\sqrt{3}\xi^2 \frac{1}{[1+(\xi q)^2]^{\frac{3}{2}}}. \tag{C.9}$$

And the two-point correlator in k-space is

$$B(q) = n_i \left(2\pi\lambda_{\mathrm{SO}}^{at} A_0\sqrt{3}\xi^2\right)^2 \frac{1}{[1+(\xi q)^2]^3} \tag{C.10}$$

From $\int B(\boldsymbol{q})\mathrm{d}\boldsymbol{q}/(2\pi)^2 = \langle\lambda^2\rangle$ we get

$$\langle\lambda^2\rangle = \frac{3\pi}{2} n_i(\lambda_{\mathrm{SO}}^{at} A_0\xi)^2. \tag{C.11}$$

C.2. Sherman spin relaxation rate

With $B(q)$ we can calculate the spin relaxation rate given by equation (13) in [87]:

$$\begin{aligned}
\frac{1}{\tau_S(k)} &= \frac{4k}{\pi v_F\hbar^2}\int_0^{2k} \frac{B(q)}{\sqrt{(2k)^2-q^2}}\mathrm{d}q \\
&= \frac{32k\xi^2\langle\lambda^2\rangle}{v_f\hbar^2}\int_0^{2k} \frac{1}{(1+(\xi q)^2)^3\sqrt{(2k)^2-q^2}}\mathrm{d}q \\
&= \frac{32k\xi^2\langle\lambda^2\rangle}{v_f\hbar^2}\int_0^{2\xi k} \frac{1}{(1+(\xi q)^2)^3\sqrt{(2\xi k)^2-(\xi q)^2}}\mathrm{d}(\xi q) \\
&= \frac{2\pi k\xi^2\langle\lambda^2\rangle}{v_f\hbar^2}\frac{8+8(2\xi k)^2+3(2\xi k)^4}{((2\xi k)^2+1)^{5/2}} \\
&= \frac{2\pi\langle\lambda^2\rangle}{v_f\hbar^2}\xi\begin{cases} 8\xi k & \xi k \ll 1 \\ \frac{3}{2} & \xi k \gg 1 \end{cases}
\end{aligned} \tag{C.12}$$

Bibliography

[1] M. N. Baibich, J. M. Broto, A. Fert, F. N. Van Dau, and F. Petroff, *Giant Magnetoresistance of (001)Fe/(001)Cr Magnetic Superlattices*, Phys. Rev. Lett. **61** (1988), 24722475.

[2] G. Binasch, P. Grünberg, F. Saurenbach, and W. Zinn, *Enhanced magnetoresistance in layered magnetic structures with antiferromagnetic interlayer exchange*, Phys. Rev. B **39** (1989), 48284830.

[3] P. Grünberg, *Magnetfeldsensor mit ferromagnetischer, dünner Schicht*, German Patent DE **3820475** (1988), C1.

[4] S. A. Wolf, *Spintronics: A Spin-Based Electronics Vision for the Future*, Science **294** (2001), 14881495.

[5] M. Julliere, *Tunneling between ferromagnetic films*, Phys. Lett. A **54** (1975), 225226.

[6] J. S. Moodera, L. R. Kinder, T. M. Wong, and R. Meservey, *Large Magnetoresistance at Room Temperature in Ferromagnetic Thin Film Tunnel Junctions*, Phys. Rev. Lett. **74** (1995), 32733276.

[7] T. Miyazaki and N. Tezuka, *Giant magnetic tunneling effect in Fe/Al2O3/Fe junction*, J. Magn. Mater. **139** (1995), 231234.

[8] D. D. Awschalom and J. M. Kikkawa, *Lateral drag of spin coherence in gallium arsenide*, Nature **397** (1999), 139.

[9] R. Fiederling, M. Keim, G. Reuscher, W. Ossau, G. Schmidt, A. Waag, and L. W. Molenkamp, *Injection and detection of a spin-polarized current in a light-emitting diode*, Nature **402** (1999), 787.

[10] H. Ohno, D. Chiba, F. Matsukura, T. Omiya, E. Abe, T. Dietl, Y. Ohno, and K. Ohtani, *Electric-field control of ferromagnetism*, Nature **408** (2000), 944.

[11] I. Malajovich, J. Kikkawa, D. Awschalom, J. Berry, and N. Samarth, *Coherent Transfer of Spin through a Semiconductor Heterointerface*, Phys. Rev. Lett. **84** (2000), 1015.

[12] M. Johnson and R. H. Silsbee, *Interfacial charge-spin coupling: Injection and detection of spin magnetization in metals*, Phys. Rev. Lett. **55** (1985), 1790.

[13] M. Johnson and R. H. Silsbee, *Coupling of electronic charge and spin at a ferromagnetic-paramagnetic metal interface*, Phys. Rev. B **37** (1988), 5312.

[14] A. Fert and H. Jaffrès, *Conditions for efficient spin injection from a ferromagnetic metal into a semiconductor*, Phys. Rev. B **64** (2001), 184420.

[15] F. J. Jedema, A. T. Filip, and B. J. van Wees, *Electrical spin injection and accumulation at room temperature in an all-metal mesoscopic spin valve*, Nature **410** (2001), 345.

[16] E. Rashba, *Properties of semiconductors with an extremum loop. 1. Cyclotron and combinational resonance in a magnetic field perpendicular to the plane of the loop*, Sov. Phys. – Solid State **2** (1960), 1109.

[17] S. Datta and B. Das, *Electronic analog of the electro-optic modulator*, Appl. Phys. Lett. **56** (1990), 665.

[18] H. C. Koo, J. H. Kwon, J. Eom, J. Chang, S. H. Han, and M. Johnson, *Control of Spin Precession in a Spin-Injected Field Effect Transistor*, Science **325** (2009), 15151518.

[19] F. J. Jedema, M. V. Costache, H. B. Heersche, J. J. A. Baselmans, and B. J. van Wees, *Electrical detection of spin accumulation and spin precession at room temperature in metallic spin valves*, Appl. Phys. Lett. **81** (2002), 5162.

[20] J. Schliemann, J. Egues, and D. Loss, *Nonballistic Spin-Field-Effect Transistor*, Phys. Rev. Lett. **90** (2003), 146801.

[21] B. A. Bernevig, J. Orenstein, and S.-C. Zhang, *Exact SU(2) Symmetry and Persistent Spin Helix in a Spin-Orbit Coupled System*, Phys. Rev. Lett. **97** (2006), 236601.

[22] M.-H. Liu, K.-W. Chen, S.-H. Chen, and C.-R. Chang, *Persistent spin helix in Rashba-Dresselhaus two-dimensional electron systems*, Phys. Rev. B **74** (2006), 235322.

[23] C. Betthausen, T. Dollinger, H. Saarikoski, V. Kolkovsky, G. Karczewski, T. Wojtowicz, K. Richter, and D. Weiss, *Spin-Transistor Action via Tunable Landau-Zener Transitions*, Science **337** (2012), 324.

[24] I. Adagideli, V. Lutsker, M. Scheid, P. Jacquod, and K. Richter, *Spin Transistor Action from Hidden Onsager Reciprocity*, Phys. Rev. Lett. **108** (2012), 236601.

[25] L. Onsager, *Reciprocal Relations in Irreversible Processes. II.*, Phys. Rev. **38** (1931), 2265.

[26] M. Büttiker, *Four-Terminal Phase-Coherent Conductance*, Phys. Rev. Lett. **57** (1986), 1761.

[27] P. R. Wallace, *The Band Theory of Graphite*, Phys. Rev. **71** (1947), 622.

[28] G. W. Semenoff, *Condensed-Matter Simulation of a Three-Dimensional Anomaly*, Phys. Rev. Lett. **53** (1984), 2449.

[29] K. S. Novoselov, A. K. Geim, S. V. Morozov, D. Jiang, Y. Zhang, S. V. Dubonos, I. V. Grigorieva, and A. A. Firsov, *Electric Field Effect in Atomically Thin Carbon Films*, Science **306** (2004), 666.

[30] Y. Zhang, Y.-W. Tan, H. L. Stormer, and P. Kim, *Experimental observation of the quantum Hall effect and Berry`s phase in graphene*, Nature **438** (2005), 201204.

[31] A. F. Young and P. Kim, *Quantum interference and Klein tunnelling in graphene heterojunctions*, Nature Physics **5** (2009), 222.

[32] S. Chen, Q. Wu, C. Mishra, J. Kang, H. Zhang, K. Cho, W. Cai, A. A. Balandin, and R. S. Ruoff, *Thermal conductivity of isotopically modifiedgraphene*, Nature Materials **11** (2012), 203207.

[33] D. Kochan, M. Gmitra, and J. Fabian, *Spin Relaxation Mechanism in Graphene: Resonant Scattering by Magnetic Impurities*, Phys. Rev. Lett. **112** (2014), 116602.

[34] O. V. Yazyev, *Emergence of magnetism in graphene materials and nanostructures*, Rep. Prog. Phys. **73** (2010), 056501.

[35] M. Fujita, K. Wakabayashi, K. Nakada, and K. Kusakabe, *Peculiar Localized State at Zigzag Graphite Edge*, J. Phys. Soc. Jpn. **65** (1996), 1920.

[36] M.-H. Liu, J. Bundesmann, and K. Richter, *Spin-dependent Klein tunneling in graphene: Role of Rashba spin-orbit coupling*, Phys. Rev. B **85** (2012), 085406.

[37] E. Y. Sherman, *Random spin–orbit coupling and spin relaxation in symmetric quantum wells*, Appl. Phys. Lett. **82** (2003), 209.

[38] V. K. Dugaev, E. Y. Sherman, V. I. Ivanov, and J. Barnaś, *Spin relaxation and combined resonance in two-dimensional electron systems with spin-orbit disorder*, Phys. Rev. B **80** (2009), 081301.

[39] P. Zhang and M. W. Wu, *Electron spin relaxation in graphene with random Rashba field: Comparison of D'yakonov-Perel' and Elliott-Yafet–like mechanisms*, New Journal of Physics **14** (2012), 033015.

[40] A. H. Castro Neto and F. Guinea, *Impurity-Induced Spin-Orbit Coupling in Graphene*, Phys. Rev. Lett. **103** (2009), 026804.

[41] M. Gmitra, S. Konschuh, C. Ertler, C. Ambrosch-Draxl, and J. Fabian, *Band-structure topologies of graphene: Spin-orbit coupling effects from first principles*, Phys. Rev. B **80** (2009), 235431.

[42] T. Frank, *Ab initio studies of fluorinated graphene*, Master's thesis, Universität Regensburg, 2014.

[43] S. Irmer, *Spin-orbit coupling in functionalized graphene structures*, Master's thesis, Universität Regensburg, 2014.

[44] G. Bergmann, *Weak localization in thin films: a time-of-flight experiment with conduction electrons*, Phys. Rep. **107** (1984), 1.

[45] S. Chakravarty and A. Schmid, *Weak localization: The quasiclassical theory of electrons in a random potential*, Phys. Rep. **140** (1986), 193.

[46] C. Beenakker and H. van Houten, *Quantum Transport in Semiconductor Nanostructures*, Semiconductor Heterostructures and Nanostructures (H. Ehrenreich and D. Turnbull, eds.), Solid State Physics, vol. 44, Academic Press, 1991, pp. 1 – 228.

[47] S. Konschuh, M. Gmitra, and J. Fabian, *Tight-binding theory of the spin-orbit coupling in graphene*, Phys. Rev. B **82** (2010), 245412.

[48] E. Akkermans and G. Montambaux, *Mesoscopic Physics of Electrons and Photons*, Cambridge University Press, 2007.

[49] S. Datta, *Electronic Transport in Mesoscopic Systems*, Cambridge University Press, May 1997.

[50] P. A. Mello and N. Kumar, *Quantum Transport in Mesoscopic Systems*, Oxford University Press, May 2004.

[51] M. P. L. Sancho, J. M. Lopez Sancho, J. M. L. Sancho, and J. Rubio, *Highly convergent schemes for the calculation of bulk and surface Green functions*, J. Phys. F: Met. Phys. **15** (1985), 851.

[52] M. Wimmer, *Quantum transport in nanostructures: From computational concepts to spintronics in graphene and magnetic tunnel junctions*, Ph.D. thesis, Universität Regensburg, Dezember 2009.

[53] D. J. Thouless and S. Kirkpatrick, *Conductivity of the disordered linear chain*, J. Phys. C: Solid State Phys. **14** (1981), 235.

[54] P. A. Lee and D. S. Fisher, *Anderson Localization in Two Dimensions*, Phys. Rev. Lett. **47** (1981), 882.

[55] A. MacKinnon, *The calculation of transport properties and density of states of disordered solids*, Z. Phys. B: Condens. Matter **59** (1985), 385.

[56] M. Wimmer and K. Richter, *Optimal block-tridiagonalization of matrices for coherent charge transport*, J. Comput. Phys. **228** (2009), 8548.

[57] D. Fisher and P. Lee, *Relation between conductivity and transmission matrix*, Phys. Rev. B **23** (1981), 6851.

[58] A. H. Castro Neto, F. Guinea, N. M. R. Peres, K. S. Novoselov, and A. K. Geim, *The electronic properties of graphene*, Rev. Mod. Phys. **81** (2009), 109.

[59] V. N. Kotov, B. Uchoa, V. M. Pereira, F. Guinea, and A. H. Castro Neto, *Electron-Electron Interactions in Graphene: Current Status and Perspectives*, Rev. Mod. Phys. **84** (2012), 1067.

[60] R. Saito, G. Dresselhaus, M. S. Dresselhaus, et al., *Physical properties of carbon nanotubes*, vol. 4, World Scientific, 1998.

[61] H. W. Kroto, J. R. Heath, S. C. O'Brien, R. F. Curl, and R. E. Smalley, *C60: Buckminsterfullerene*, Nature **318** (1985), 162.

[62] S. Iijima, *Helical microtubules of graphitic carbon*, Nature **354** (1991), 56.

[63] S. Iijima and T. Ichihashi, *Single-shell carbon nanotubes of 1-nm diameter*, Nature **363** (1993), 603.

[64] D. S. Bethune, C. H. Klang, M. S. de Vries, G. Gorman, R. Savoy, J. Vazquez, and R. Beyers, *Cobalt-catalysed growth of carbon nanotubes with single-atomic-layer walls*, Nature **363** (1993), 605.

[65] C. L. Kane and E. J. Mele, *Quantum Spin Hall Effect in Graphene*, Phys. Rev. Lett. **95** (2005), 226801.

[66] H. Min, J. E. Hill, N. A. Sinitsyn, B. R. Sahu, L. Kleinman, and A. H. MacDonald, *Intrinsic and Rashba spin-orbit interactions in graphene sheets*, Phys. Rev. B **74** (2006), 165310.

[67] D. Huertas-Hernando, F. Guinea, and A. Brataas, *Spin-orbit coupling in curved graphene, fullerenes, nanotubes, and nanotube caps*, Phys. Rev. B **74** (2006), 155426.

[68] M.-H. Liu and C.-R. Chang, *Upstanding Rashba spin in honeycomb lattices: Electrically reversible surface spin polarization*, Phys. Rev. B **80** (2009), 241304.

[69] O. Klein, *Die Reflexion von Elektronen an einem Potentialsprung nach der relativistischen Dynamik von Dirac*, Z. Phys. **53** (1929), 157 (German).

[70] F. Sauter, *Über das Verhalten eines Elektrons im homogenen elektrischen Feld nach der relativistischen Theorie Diracs*, Z. Phys. **69** (1931), 742 (German).

[71] M. I. Katsnelson, K. S. Novoselov, and A. K. Geim, *Chiral tunnelling and the Klein paradox in graphene*, Nature Physics **2** (2006), 620.

[72] T. Ando, T. Nakanishi, and R. Saito, *Berry's Phase and Absence of Back Scattering in Carbon Nanotubes*, J. Phys. Soc. Jpn. **67** (1998), 2857.

[73] V. V. Cheianov and V. I. Fal'ko, *Selective transmission of Dirac electrons and ballistic magnetoresistance of n-p junctions in graphene*, Phys. Rev. B **74** (2006), 041403.

[74] N. Stander, B. Huard, and D. Goldhaber-Gordon, *Evidence for Klein Tunneling in Graphene p-n Junctions*, Phys. Rev. Lett. **102** (2009), 026807.

[75] A. Yamakage, K.-I. Imura, J. Cayssol, and Y. Kuramoto, *Spin-orbit effects in a graphene bipolar pn junction*, EPL **87** (2009), 47005.

[76] N. Tombros, C. Jozsa, M. Popinciuc, H. T. Jonkman, and B. J. van Wees, *Electronic spin transport and spin precession in single graphene layers at room temperature*, Nature **448** (2007), 571.

[77] C. Józsa, M. Popinciuc, N. Tombros, H. T. Jonkman, and B. J. van Wees, *Electronic Spin Drift in Graphene Field-Effect Transistors*, Phys. Rev. Lett. **100** (2008), 236603.

[78] N. Tombros, S. Tanabe, A. Veligura, C. Jozsa, M. Popinciuc, H. T. Jonkman, and B. J. van Wees, *Anisotropic Spin Relaxation in Graphene*, Phys. Rev. Lett. **101** (2008), 046601.

[79] C. Józsa, T. Maassen, M. Popinciuc, P. J. Zomer, A. Veligura, H. T. Jonkman, and B. J. van Wees, *Linear scaling between momentum and spin scattering in graphene*, Phys. Rev. B **80** (2009), 241403.

[80] C. Józsa, M. Popinciuc, N. Tombros, H. T. Jonkman, and B. J. van Wees, *Controlling the efficiency of spin injection into graphene by carrier drift*, Phys. Rev. B **79** (2009), 081402.

[81] M. Popinciuc, C. Józsa, P. J. Zomer, N. Tombros, A. Veligura, H. T. Jonkman, and B. J. van Wees, *Electronic spin transport in graphene field-effect transistors*, Phys. Rev. B **80** (2009), 214427.

[82] M. Orlita, C. Faugeras, G. Martinez, D. Maude, J. Schneider, M. Sprinkle, C. Berger, W. de Heer, and M. Potemski, *Magneto-transmission of multi-layer epitaxial graphene and bulk graphite: A comparison*, Solid State Commun. **149** (2009), 1128.

[83] W. Han, W. H. Wang, K. Pi, K. M. McCreary, W. Bao, Y. Li, F. Miao, C. N. Lau, and R. K. Kawakami, *Electron-Hole Asymmetry of Spin Injection and Transport in Single-Layer Graphene*, Phys. Rev. Lett. **102** (2009), 137205.

[84] K. Pi, K. M. McCreary, W. Bao, W. Han, Y. F. Chiang, Y. Li, S.-W. Tsai, C. N. Lau, and R. K. Kawakami, *Electronic doping and scattering by transition metals on graphene*, Phys. Rev. B **80** (2009), 075406.

[85] D. Huertas-Hernando, F. Guinea, and A. Brataas, *Spin-Orbit-Mediated Spin Relaxation in Graphene*, Phys. Rev. Lett. **103** (2009), 146801.

[86] C. Ertler, S. Konschuh, M. Gmitra, and J. Fabian, *Electron spin relaxation in graphene: The role of the substrate*, Phys. Rev. B **80** (2009), 041405.

[87] V. K. Dugaev, E. Y. Sherman, and J. Barnaś, *Spin dephasing and pumping in graphene due to random spin-orbit interaction*, Phys. Rev. B **83** (2011), 085306.

[88] Y. Zhou and M. W. Wu, *Electron spin relaxation in graphene from a microscopic approach: Role of electron-electron interaction*, Phys. Rev. B **82** (2010), 085304.

[89] P. Zhang and M. W. Wu, *Electron spin diffusion and transport in graphene*, Phys. Rev. B **84** (2011), 045304.

[90] P. Zhang, Y. Zhou, and M. W. Wu, *Electron spin relaxation in rippled graphene with low mobilities*, J. Appl. Phys. **112** (2012), 073709.

[91] Y. Zhou and M. W. Wu, *Single-parameter quantum charge and spin pumping in armchair graphene nanoribbons*, Phys. Rev. B **86** (2012), 085406.

[92] H. Ochoa, A. H. Castro Neto, and F. Guinea, *Elliot-Yafet Mechanism in Graphene*, Phys. Rev. Lett. **108** (2012), 206808.

[93] M. Droth and G. Burkard, *Electron spin relaxation in graphene nanoribbon quantum dots*, Phys. Rev. B **87** (2013), 205432.

[94] S. Fratini, D. Gosálbez-Martínez, P. Merodio Cámara, and J. Fernández-Rossier, *Anisotropic intrinsic spin relaxation in graphene due to flexural distortions*, Phys. Rev. B **88** (2013), 115426.

[95] M. Gmitra, D. Kochan, and J. Fabian, *Spin-Orbit Coupling in Hydrogenated Graphene*, Phys. Rev. Lett. **110** (2013), 246602.

[96] C. Weeks, J. Hu, J. Alicea, M. Franz, and R. Wu, *Engineering a Robust Quantum Spin Hall State in Graphene via Adatom Deposition*, Phys. Rev. X **1** (2011), 021001.

[97] R. J. Elliott, *Theory of the Effect of Spin-Orbit Coupling on Magnetic Resonance in Some Semiconductors*, Phys. Rev. **96** (1954), 266.

[98] Y. Yafet, *g Factors and Spin-Lattice Relaxation of Conduction Electrons*, Solid State Physics (F. Seitz and D. Turnbull, eds.), Solid State Physics, vol. 14, Academic Press, 1963, pp. 1 – 98.

[99] M. Dyakonov and V. Y. Kachorovskii, *Spin relaxation of two-dimensional electrons in noncentrosymmetric semiconductors*, Sov. Phys. Semicond **20** (1986), 110.

[100] I. Zutic, J. Fabian, and S. Das Sarma, *Spintronics: Fundamentals and applications*, Rev. Mod. Phys. **76** (2004), 323.

[101] J. Fabian, A. Matos-Abiague, C. Ertler, P. Stano, and I. Žutić, *Semiconductor spintronics*, Acta Physica Slovaca **57** (2007), 565.

[102] M. D'yakonov and V. Perel', *Spin Orientation of Electrons Associated with the Interband Absorption of Light in Semiconductors*, J. Exp. Theor. Phys. **60** (1971), 1053.

[103] C. W. J. Beenakker, *Random-matrix theory of quantum transport*, Rev. Mod. Phys. **69** (1997), 731.

[104] K. Pi, W. Han, K. M. McCreary, A. G. Swartz, Y. Li, and R. K. Kawakami, *Manipulation of Spin Transport in Graphene by Surface Chemical Doping*, Phys. Rev. Lett. **104** (2010), 187201.

[105] W. Han and R. K. Kawakami, *Spin Relaxation in Single-Layer and Bilayer Graphene*, Phys. Rev. Lett. **107** (2011), 047207.

[106] G. Dresselhaus, *Spin-Orbit Coupling Effects in Zinc Blende Structures*, Phys. Rev. **100** (1955), 580.

[107] S. Tarasenko, *Scattering induced spin orientation and spin currents in gyrotropic structures*, JETP Lett. **84** (2006), 199.

[108] S.-Z. Liang and J. O. Sofo, *Impurity State and Variable Range Hopping Conduction in Graphene*, Phys. Rev. Lett. **109** (2012), 256601.

[109] C.-C. Liu, H. Jiang, and Y. Yao, *Low-energy effective Hamiltonian involving spin-orbit coupling in silicene and two-dimensional germanium and tin*, Phys. Rev. B **84** (2011), 195430.

[110] X. Hong, K. Zou, B. Wang, S.-H. Cheng, and J. Zhu, *Evidence for Spin-Flip Scattering and Local Moments in Dilute Fluorinated Graphene*, Phys. Rev. Lett. **108** (2012), 226602.

[111] X. Hong, S.-H. Cheng, C. Herding, and J. Zhu, *Colossal negative magnetoresistance in dilute fluorinated graphene*, Phys. Rev. B **83** (2011), 085410.

[112] R. R. Nair, M. Sepioni, I.-L. Tsai, O. Lehtinen, J. Keinonen, A. V. Krasheninnikov, T. Thomson, A. K. Geim, and I. V. Grigorieva, *Spin-half paramagnetism in graphene induced by point defects*, Nature Physics **8** (2012), 199202.

[113] H.-J. Kim and J.-H. Cho, *Fluorine-induced local magnetic moment in graphene: A hybrid DFT study*, Phys. Rev. B **87** (2013), 174435.

[114] H. Y. Liu, Z. F. Hou, C. H. Hu, Y. Yang, and Z. Z. Zhu, *Electronic and Magnetic Properties of Fluorinated Graphene with Different Coverage of Fluorine*, J. Phys. Chem. C **116** (2012), 1819318201.

[115] E. J. G. Santos, A. Ayuela, and D. Snchez-Portal, *Universal magnetic properties of sp 3 -type defects in covalently functionalized graphene*, New Journal of Physics **14** (2012), 043022.

[116] J. O. Sofo, A. M. Suarez, G. Usaj, P. S. Cornaglia, A. D. Hernández-Nieves, and C. A. Balseiro, *Electrical control of the chemical bonding of fluorine on graphene*, Phys. Rev. B **83** (2011), 081411.

[117] D. A. Ryndyk, J. Bundesmann, M.-H. Liu, and K. Richter, *Edge state effects in junctions with graphene electrodes*, Phys. Rev. B **86** (2012), 195425.

[118] J. Bundesmann, M.-H. Liu, d. Adagideli, and K. Richter, *Spin conductance of diffusive graphene nanoribbons: A probe of zigzag edge magnetization*, Phys. Rev. B **88** (2013), 195406.

[119] K. Nakada, M. Fujita, G. Dresselhaus, and M. S. Dresselhaus, *Edge state in graphene ribbons: Nanometer size effect and edge shape dependence*, Phys. Rev. B **54** (1996), 17954.

[120] J. Cai, P. Ruffieux, R. Jaafar, M. Bieri, T. Braun, S. Blankenburg, M. Muoth, A. P. Seitsonen, M. Saleh, X. Feng, and et al., *Atomically precise bottom-up fabrication of graphene nanoribbons*, Nature **466** (2010), 470.

[121] L. Jiao, L. Zhang, X. Wang, G. Diankov, and H. Dai, *Narrow graphene nanoribbons from carbon nanotubes*, Nature **458** (2009), 877.

[122] A. Yamashiro, Y. Shimoi, K. Harigaya, and K. Wakabayashi, *Spin- and charge-polarized states in nanographene ribbons with zigzag edges*, Phys. Rev. B **68** (2003), 193410.

[123] Y.-W. Son, M. L. Cohen, and S. G. Louie, *Half-metallic graphene nanoribbons*, Nature **444** (2006), 347.

[124] M. Wimmer, I. Adagideli, S. Berber, D. Tománek, and K. Richter, *Spin Currents in Rough Graphene Nanoribbons: Universal Fluctuations and Spin Injection*, Phys. Rev. Lett. **100** (2008), 177207.

[125] W. L. Wang, O. V. Yazyev, S. Meng, and E. Kaxiras, *Topological Frustration in Graphene Nanoflakes: Magnetic Order and Spin Logic Devices*, Phys. Rev. Lett. **102** (2009), 157201.

[126] T. O. Wehling, E. Şaşıoğlu, C. Friedrich, A. I. Lichtenstein, M. I. Katsnelson, and S. Blügel, *Strength of Effective Coulomb Interactions in Graphene and Graphite*, Phys. Rev. Lett. **106** (2011), 236805.

[127] H. Feldner, Z. Y. Meng, A. Honecker, D. Cabra, S. Wessel, and F. F. Assaad, *Magnetism of finite graphene samples: Mean-field theory compared with exact diagonalization and quantum Monte Carlo simulations*, Phys. Rev. B **81** (2010), 115416.

[128] H. Karimi and I. Affleck, *Towards a rigorous proof of magnetism on the edges of graphene nanoribbons*, Phys. Rev. B **86** (2012), 115446.

[129] E. Grichuk and E. Manykin, *Spin polarized quantum pump effect in zigzag graphene nanoribbons*, JETP Lett. **93** (2011), 372 (English).

[130] V. L. J. Joly, M. Kiguchi, S.-J. Hao, K. Takai, T. Enoki, R. Sumii, K. Amemiya, H. Muramatsu, T. Hayashi, Y. A. Kim, M. Endo, J. Campos-Delgado, F. López-Urías, A. Botello-Méndez, H. Terrones, M. Terrones, and M. S. Dresselhaus, *Observation of magnetic edge state in graphene nanoribbons*, Phys. Rev. B **81** (2010), 245428.

[131] Y. Kobayashi, K. Fukui, T. Enoki, and K. Kusakabe, *Edge state on hydrogen-terminated graphite edges investigated by scanning tunneling microscopy*, Phys. Rev. B **73** (2006), 125415.

[132] K. A. Ritter and J. W. Lyding, *The influence of edge structure on the electronic properties of graphene quantum dots and nanoribbons*, Nature Materials **8** (2009), 235.

[133] X. Zhang, O. V. Yazyev, J. Feng, L. Xie, C. Tao, Y.-C. Chen, L. Jiao, Z. Pedramrazi, A. Zettl, S. G. Louie, H. Dai, and M. F. Crommie, *Experimentally Engineering the Edge Termination of Graphene Nanoribbons*, ACS Nano **7** (2013), 198.

[134] R. Farghadan and E. Saievar-Iranizad, *Spin-polarized transport in zigzag-edge graphene nanoribbon junctions*, J. Appl. Phys. **111** (2012), 014304.

[135] O. Dorokhov, *Transmission coefficient and the localization length of an electron in N bound disordered chains*, JETP Lett. **36** (1982), 318.

[136] P. Mello, P. Pereyra, and N. Kumar, *Macroscopic approach to multichannel disordered conductors*, Ann. Phys. **181** (1988), 290 .

[137] J. Hubbard, *Electron Correlations in Narrow Energy Bands*, Proc. R. Soc. London, Ser. A **276** (1963), 238.

[138] J. Fernández-Rossier and J. J. Palacios, *Magnetism in Graphene Nanoislands*, Phys. Rev. Lett. **99** (2007), 177204.

[139] T. Wassmann, A. P. Seitsonen, A. M. Saitta, M. Lazzeri, and F. Mauri, *Structure, Stability, Edge States, and Aromaticity of Graphene Ribbons*, Phys. Rev. Lett. **101** (2008), 096402.

[140] J. Kunstmann, C. Özdoğan, A. Quandt, and H. Fehske, *Stability of edge states and edge magnetism in graphene nanoribbons*, Phys. Rev. B **83** (2011), 045414.

[141] R. R. Nair, M. Sepioni, I.-L. Tsai, O. Lehtinen, J. Keinonen, A. V. Krasheninnikov, T. Thomson, A. K. Geim, and I. V. Grigorieva, *Spin-half paramagnetism in graphene induced by point defects*, Nature Phys. **8** (2012), 199.

[142] H. S. S. Ramakrishna Matte, K. S. Subrahmanyam, and C. N. R. Rao, *Novel Magnetic Properties of Graphene: Presence of Both Ferromagnetic and Antiferromagnetic Features and Other Aspects*, J. Phys. Chem. C **113** (2009), 9982.

[143] J. Fernández-Rossier, *Prediction of hidden multiferroic order in graphene zigzag ribbons*, Phys. Rev. B **77** (2008), 075430.

[144] J. Jung and A. H. MacDonald, *Carrier density and magnetism in graphene zigzag nanoribbons*, Phys. Rev. B **79** (2009), 235433.

[145] J.-L. Pichard, *Random Transfer Matrix Theory and Conductance Fluctuations*, Quantum Coherence in Mesoscopic Systems (B. Kramer, ed.), NATO ASI Series B, vol. 254, 1991, p. 369, p. p. 369.

[146] P. W. Brouwer and K. Frahm, *Quantum transport in disordered wires: Equivalence of the one-dimensional σ model and the Dorokhov-Mello-Pereyra-Kumar equation*, Phys. Rev. B **53** (1996), 1490.

[147] W. Han, K. McCreary, K. Pi, W. Wang, Y. Li, H. Wen, J. Chen, and R. Kawakami, *Spin transport and relaxation in graphene*, J. Magn. Mater. **324** (2012), 369 .

[148] J. Cai, P. Ruffieux, R. Jaafar, M. Bieri, T. Braun, S. Blankenburg, M. Muoth, A. P. Seitsonen, M. Saleh, X. Feng, et al., *Atomically precise bottom-up fabrication of graphene nanoribbons*, Nature **466** (2010), 470.

[149] X. Jia, J. Campos-Delgado, M. Terrones, V. Meunier, and M. S. Dresselhaus, *Graphene edges: a review of their fabrication and characterization*, Nanoscale **3** (2011), 86.

[150] H. Mizuta, N. Kalhor, S. Hang, S. Boden, Z. Moktadir, H. Rutt, and D. Bagnall, *Ultrafine graphene nanodevice fabrication*, SPIE Newsroom (2013).

[151] Q. Xu, M.-Y. Wu, G. F. Schneider, L. Houben, S. K. Malladi, C. Dekker, E. Yucelen, R. E. Dunin-Borkowski, and H. W. Zandbergen, *Controllable Atomic Scale Patterning of Freestanding Monolayer Graphene at Elevated Temperature*, ACS Nano **7** (2013), 15661572.

[152] F. Oberhuber, S. Blien, S. Heydrich, F. Yaghobian, T. Korn, C. Schuller, C. Strunk, D. Weiss, and J. Eroms, *Weak localization and Raman study of anisotropically etched graphene antidots*, Appl. Phys. Lett. **103** (2013), 143111.

[153] J. Baringhaus, M. Ruan, F. Edler, A. Tejeda, M. Sicot, A. Taleb-Ibrahimi, A.-P. Li, Z. Jiang, E. H. Conrad, C. Berger, and et al., *Exceptional ballistic transport in epitaxial graphene nanoribbons*, Nature **506** (2014), 349354.

[154] M. Orlita, C. Faugeras, P. Plochocka, P. Neugebauer, G. Martinez, D. K. Maude, A.-L. Barra, M. Sprinkle, C. Berger, W. A. de Heer, and et al., *Approaching the Dirac Point in High-Mobility Multilayer Epitaxial Graphene*, Physical Review Letters **101** (2008), 267601.

[155] G. Czycholl, *Theoretische Festkrperphysik*, Springer-Lehrbuch, Springer Berlin Heidelberg, 2008.

[156] I. S. Gradshteyn and I. M. Ryzhik, *Table of Integrals, Series, and Products, Seventh Edition*, 7th ed., Academic Press, January 2007.

Publication list

- Ming-Hao Liu, Jan Bundesmann and Klaus Richter
  Spin-dependent Klein tunneling in graphene: Role of Rashba spin-orbit coupling
  Phys. Rev. B **85**, 085406 (2012)

- Silvia Minke, Jan Bundesmann, Dieter Weiss and Jonathan Eroms
  Phase coherent transport in graphene nanoribbons and graphene nanoribbon arrays
  Phys. Rev. B **86**, 155403 (2012)

- Dmitry A. Ryndyk, Jan Bundesmann, Ming-Hao Liu and Klaus Richter
  Edge state effects in junctions with graphene electrodes
  Phys. Rev. B **86**, 195425 (2012)

- Jan Bundesmann, Ming-Hao Liu, Inanç Adagideli and Klaus Richter
  Spin conductance of diffusive graphene nanoribbons: A probe of zigzag edge magnetization
  Phys. Rev. B **88**, 195406 (2013)

Danksagung

Mein größter Dank gilt meinem Doktorvater *Prof. Dr. Klaus Richter*, der diese Arbeit erst möglich gemacht hat. Er hat meine Arbeit immer unterstützt und war da, wenn Rat und sein immenses Wissen über mesoskopische Physik nötig waren.

Im Laufe meiner Promotion habe ich mit vielen Menschen zusammengearbeitet, die alle wichtige Beiträge zur vorliegenden Arbeit gebracht haben. Von diesen möchte ich einigen meinen besonderen Dank aussprechen.

Prof. Dr. Jaroslav Fabian, der mich an sein Erfahrung mit Spintransport und Graphen teilhaben ließ. Ich bedanke mich auch bei den Mitgliedern seiner Arbeitsgruppe *Dr. Martin Gmitra*, *Dr. Denis Kochan*, *Susanne Irmer* und *Tobias Frank*, die mit ihren Daten die Grundlagen für die verschiedenen Modellierungen adsorbierter Atome auf Graphen legten. Außerdem danke ich *Prof. Dr. Inanç Adagideli*, der viel Wissen und Enthusiasmus beisteuerte, besonders im Bezug auf die magnetischen Randkanäle in Graphen-Zickzack-Nanostreifen. Des Weiteren danke ich *Dr. Dima Ryndyk*, durch den ich einen Einblick in Molekül-Elektronik erhalten habe und ganz besonders *Dr. Ming-Hao Liu* und *Fedor Tkatschenko*, mit denen ich permanent im Austausch stand, so daß eine klare Benennung ihres Einflusses gar nicht mehr möglich ist.

Ebenso bedanke ich mich bei unserer "topical group" zu topologischen Isolatoren und Graphen, die aus *Sven Essert*, *Lisa Hesse*, *Dr. Viktor Krückl*, *Dr. Ming-Hao Liu*, *Fedor Tkatschenko* und *Dr. Jürgen Wurm* bestand, bei *Dr. Tobias Dollinger* und *Quirin Humml*, die mich immer wieder über den Graphen'schen Tellerrand hinausblicken ließen und bei *Dr. Mike Wimmer*, der mit seiner Implementierung des rekursiven Greensfunktionsalgorithmus eine wichtige Grundlage für diese Arbeit gelegt hat.

Für das Korrekturlesen meiner Dissertation danke ich *Dr. Tobias Dollinger*, *Dr. Viktor Krückl*, *Dr. Ming-Hao Liu*, *Josef Michl* und *Dr. Juan-Diego Urbina* und ganz besonders *Fedor Tkatschenko*, der beinahe die ganze Arbeit gelesen hat.

Für die Finanzierung im Rahmen von Graduiertenkollen 1570 und Sonderforschungsbereich 689 danke ich der DFG. Für ideelle Förderung danke ich der Hans-Böckler-Stiftung.